REPORT DOCUMENTATION PAGE

AFRL-SR-AR-TR-09-0232

1. REPORT DATE *(DD-MM-YYYY)*	2. REPORT TYPE	3. DATES COVERED *(From - To)*
06/30/2009	Final Technical Report	11/30/2006-02/28/2009

4. TITLE AND SUBTITLE

Supercritical Combustion of Liquid Oxygen and Hydrocarbon for Staged-Combustion Cycle Engine Technology Development

5a. CONTRACT NUMBER

5b. GRANT NUMBER
FA9550-07-1-0111

5c. PROGRAM ELEMENT NUMBER

6. AUTHOR(S)

Vigor Yang

5d. PROJECT NUMBER

5e. TASK NUMBER

5f. WORK UNIT NUMBER

7. PERFORMING ORGANIZATION NAME(S) AND ADDRESS(ES)

The Pennsylvania State University
104 Research Building East
University Park, PA 16802

8. PERFORMING ORGANIZATION REPORT NUMBER

9. SPONSORING / MONITORING AGENCY NAME(S) AND ADDRESS(ES)

Dr. Mitat A. Birkan
Air Force Office of Scientific Research
875 N. Randolph Street, Ste. 325
Arlington, VA 22203-1768

10. SPONSOR/MONITOR'S ACRONYM(S)
AFOSR

11. SPONSOR/MONITOR'S REPORT NUMBER(S)

12. DISTRIBUTION / AVAILABILITY STATEMENT

Approved for public release; distribution unlimited.

13. SUPPLEMENTARY NOTES

14. ABSTRACT

An integrated modeling and numerical program has been conducted to substantially improve the fundamental knowledge of supercritical fluid dynamics and combustion of oxygen and hydrocarbon fuels under conditions representative of contemporary liquid-propellant rocket engines. Emphasis was placed on the swirler injector flow dynamics and flame stabilization and spreading. The fundamental characteristics of counter-flow diffusion flames of oxygen and hydrogen, as well as hydrocarbons, were also explored. The analysis was based on the complete conservation equations for a multi-component chemically reacting mixture, and accommodated general-fluid thermodynamics and transport phenomena valid for the entire range of fluid states of concern. Turbulence closure was treated using the large-eddy-simulation (LES) technique. Start-of-the-art closure schemes for subgrid-scale dynamics and turbulence/chemistry interactions were implemented. The effects of design attributes (e.g., injection port size and location, center post recess distance, etc.) and operating conditions (e.g., chamber pressure, velocity, and temperature, swirl strength, etc) on injector characteristics were assessed. Results not only enhance the basic understanding of the subject problems, but also provide a quantitative basis to identify and prioritize the key design parameters and flow variables that exert dominant influence on the injector behavior in different environments.

15. SUBJECT TERMS

supercritical fluid injection, mixing, and combustion; liquid rocket engines, injectors

16. SECURITY CLASSIFICATION OF:			17. LIMITATION OF ABSTRACT	18. NUMBER OF PAGES	19a. NAME OF RESPONSIBLE PERSON
a. REPORT	b. ABSTRACT	c. THIS PAGE			19b. TELEPHONE NUMBER *(include area code)*
unclassified	unclassified	unclassified	UU	76	(814) 863-1052

Final Report
on

Supercritical Combustion of Liquid Oxygen and Hydrocarbon for Staged-Combustion Cycle Engine Technology Development

For

AFOSR Contract/Grant FA9550-07-1-0111

Prepared by

Vigor Yang
Department of Mechanical Engineering
The Pennsylvania State University
104 Research Building East
University Park, PA16802

Submitted to:

Dr. Mitat A. Birkan
Air Force Office of Scientific Research
875 N. Randolph Street, Ste. 325
Arlington, VA 22203-1768

June 30, 2009

TABLE OF CONTENTS

Supercritical Combustion of Liquid Oxygen and Hydrocarbon for Staged-Combustion Cycle Engine Technology Development

SUMMARY

An integrated modeling and numerical program has been conducted to substantially improve the fundamental knowledge of supercritical fluid dynamics and combustion of oxygen and hydrocarbon fuels under conditions representative of contemporary liquid-propellant rocket engines. Emphasis was placed on the swirler injector flow dynamics and flame stabilization of LOX and methane. The fundamental characteristics of counter-flow diffusion flames of oxygen and hydrogen (or methane) were also explored. The analysis was based on the complete conservation equations for a multi-component chemically reacting mixture, and accommodated general-fluid thermodynamics and transport phenomena valid for the entire range of fluid states of concern. Turbulence closure was treated using the large-eddy-simulation (LES) technique. Start-of-the-art closure schemes for subgrid-scale dynamics and turbulence/chemistry interactions were implemented.

The work addressed the following issues:

1. cryogenic fluid dynamics of pressure swirl injectors at supercritical conditions,
2. counterflow diffusion flames of general fluids, including oxygen/hydrogen and oxygen/methane mixtures, and
3. flame stabilization and spreading of liquid oxygen (LOX) and methane at supercritical conditions.

Various underlying physiochemical mechanisms associated with swirl co-axial injectors have been studied in detail. These include flow evolution, flame stabilization and spreading, heat transfer, and acoustic response. The effects of design attributes (e.g., injection port size and location, center post recess distance, etc.) and operating conditions (e.g., chamber pressure, velocity, and temperature, swirl strength, etc) on injector characteristics were assessed. Results not only enhance the basic understanding of the subject problems, but also provide a quantitative basis to identify and prioritize the key design parameters and flow variables that exert dominant influence on the injector behavior in different environments.

Results from this research project have led to the following publications.

1. "Cryogenic Fluid Dynamics of Pressure Swirl Injectors at Supercritical Conditions," by N. Zong and V. Yang, *Physics of Fluids*, Vol. 20, 2008, 056103 (1-14).

2. "Counterflow Diffusion Flames of General Fluids: Oxygen/Hydrogen Mixtures," by G. Ribert, N. Zong, V. Yang, L. Pons, N. Darabiha, and S. Candel, *Combustion and Flame*, Vol. 154, 2008, pp. 319-330.

3. "Mass Transfer and Combustion in Transcritical Non-Premixed Counterflows," by L. Pons, N. Darabiha, S. Candel, G. Ribert, and V. Yang, *Combustion Theory and Modeling*, Vol. 13, No. 1, 2009, pp. 57-81.

4. "Supercritical Combustion of LOX/Methane Stabilized by a Splitter Plate," by N. Zong, G. Ribert, and V. Yang, AIAA Paper 2007-0575, presented at the 45th AIAA Aerospace Sciences Meeting and Exhibit, January 2007.

5. "Large Eddy Simulation of Combustion of Liquid Oxygen and Methane in a Supercritical Environment," by G. Ribert, N. Zong, and V. Yang, presented at European Community Conference on Large Eddy Simulation for Advanced Design of Combustion Systems, Rouen, France, May 2007.

6. "A Flamelet Approach for Modeling of Liquid Oxygen (LOX)/Methane Flames at Supercritical Pressures," by N. Zong, G. Ribert, and V. Yang, AIAA Paper 2008-946, presented at 46th AIAA Aerospace Sciences Meeting and Exhibit, January 2008.

7. "Cryogenic Fluid Dynamic Response of Swirl Injector to External Forcing at Supercritical Conditions," by H. Huo, N. Zong, and V. Yang, AIAA Paper 2009-0233, presented at 47th Aerospace Sciences Meeting, January 2009.

Task 1

Cryogenic Fluid Dynamics of Pressure Swirl Injectors at Supercritical Conditions

Summary

A comprehensive numerical analysis has been conducted to explore the development of liquid oxygen flow in pressure swirl injectors operating at supercritical pressures. The model is based on full-conservation laws and accommodates real-fluid thermodynamics and transport phenomena over the entire range of fluid states of concern. Three different flow regimes with distinct characteristics, the developing, stationary, and accelerating regimes, are identified within the injector. Results are compared with predictions from classical hydrodynamic theories to acquire direct insight into the flow physics involved. In addition, various flow dynamics are investigated by means of the spectral and proper-orthogonal-decomposition techniques. The interactions between the hydrodynamic instabilities in the LOX film and acoustic oscillations in the gaseous core are clearly observed and studied. The influences of flow conditions (mass flowrate, swirl strength of the injected fluid, and ambient pressure) and injector geometry (injector length and tangential entry location) on the injector flow behavior are characterized systematically in terms of the LOX film thickness and spreading angle. The axial and azimuthal momentum exchange and loss mechanisms are also examined.

1.1 Introduction

This paper deals with the cryogenic fluid dynamics of a pressure swirl injector, as shown schematically by the center element of a co-axial injector in Fig. 1. The configuration is representative of contemporary liquid-propellant rocket injectors for liquid/liquid and gas/liquid mixtures.[1] Liquid propellant is introduced tangentially into the center post, and then forms a swirling film attached to the wall due to centrifugal force. A hollow gas core exists in the center region in accordance with the conservation of angular momentum. The film exits the injector as a thin sheet and impinges onto the surrounding

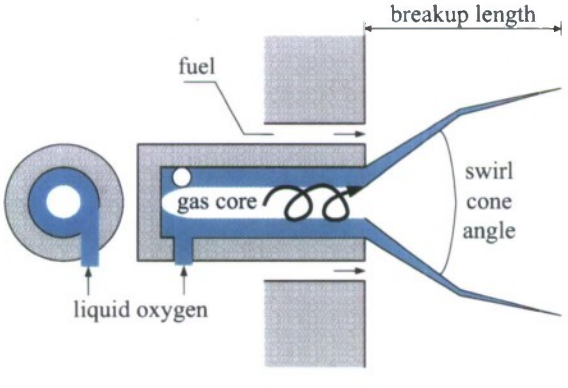

Fig. 1 Schematic of swirl co-axial injector.

fuel stream. The swirl injection/atomization process basically involves two mechanisms: disintegration of the liquid sheet as it swirls and stretches; and sheet break-up due to the interaction with the surrounding co-axial flow. In spite of the broad applications of swirl co-axial injectors, fundamental studies on the mixing and combustion processes appear to be limited, especially at scales sufficient to identify the underlying mechanisms dictating the flow evolution and flame dynamics, and at high-pressures.

Compared with jet injectors, swirl injectors in liquid-propellant rocket engines (LREs) distinguish themselves in several aspects.[1] First, the non-uniform mixing of propellants in the jet core region is avoided and the intra-element mixing is significantly improved because of the outward spreading of the liquid spray.[2] High mixing efficiency is thus possible even for a large injector flowrate. Second, the large flow passage in a swirl injector renders the atomization characteristics less sensitive to manufacturing errors. The injector is also less susceptible to choking and cavitation. Third, the injected fluid is discharged into the chamber as a hollow spray cone. The thickness of the liquid film becomes thinner as it swirls and spreads outward. The resultant mean diameter of droplets is 2.2 to 2.5-times smaller than that produced by a jet injector with the same pressure drop and mass flowrate. The droplet size distribution is also more uniform. Finally, rocket swirl injectors feature large aspect ratios of up to 20, due to the manifolding considerations of propellant supply. The viscous loss along the injector wall exerts significant influence on the flow evolution and subsequently alters liquid atomization characteristics.

Hulka et al. [2-4] conducted a series of cold-flow studies to optimize the design of swirl co-axial injectors for liquid rockets. Three different types of experiments were performed in a quiescent, atmospheric environment. Still photographs were first taken to measure the spreading angle of a water spray without a surrounding co-flow. The circumferential spray uniformity and droplet size distribution were then measured under conditions with and without co-flow nitrogen gas by means of a grid patternator and a Malvern droplet size analyzer, respectively. The co-flow reduces the mean droplet size, but widens the droplet size distribution. Measurements were also made of the Rupe mixing efficiency using water and a sucrose solution to simulate liquid oxygen and gaseous hydrogen, respectively. A broad range of fuel-to-oxidizer mixture (0.94-17.8) and velocity (1.15-4.28) ratios at one atmosphere was considered. The mixing efficiency could be greatly enhanced by increasing the initial swirl strength of the oxidizer, which is a function of the injector geometric characteristic parameter. The oxidizer mass flowrate has little influence on the mixing efficiency. Thus, an oxidizer swirl element with a mass flowrate greater than that of a shear co-axial injector can still achieve better mixing efficiency.

A similar cold-flow experiment with water and nitrogen as injectants was performed by Sasaki et al.[5] at room conditions. Special attention was given to the effect of the center post recess, which tends to narrow the spreading angle and cause a deformation of the spray cone. The influence of the annular co-flow on spray characteristics was also investigated. The swirling liquid sheet that blocked the outer gas-flow passage in a recessed injector was blown off in a mushroom shape accompanied with a high-intensity screaming sound. This phenomenon, known as self-pulsation, may

result in reduced combustion efficiency and high-amplitude pressure oscillations in the chamber.[1,6]

The recess effects of the center element on the mixing characteristics of a swirl co-axial injector were also examined by Han et al.[7] and Kim et al.[8] using kerosene as the fuel and water as the oxidizer simulant. Backlit stroboscopic photographs were taken to determine the liquid spreading angle and breakup length. The median droplet size, propellant mass distribution, and mixing efficiency were measured using a phase Doppler particle analyzer (PDPA) and a mechanical patternator. The influence of the inner-stream spreading angle was taken into account by considering four different recess numbers in the range of 0.71-1.37, defined as the ratio of the recess length to the distance from the center post to the position where the swirling liquid sheet impinges onto the outer wall of the annular passage. The mixing efficiency and propellant mass distribution were found to be very sensitive to the recess length. The Sauter mean diameter of droplets decreased slightly with increasing recess length, and could be correlated with the empirical equations suggested by Lefebvre[9] and Jones.[10]

Marchione et al.[11] recently used a PDPA system to measure the mean droplet size and velocity profiles of a kerosene spray produced by a swirl injector. The experiment was conducted in a quiescent environment at one atmosphere. Instantaneous images were taken with a high-speed CCD camera to analyze both the static and oscillatory behaviors of the spray. The spray angle estimated based on the measured mean droplet size and velocity agreed well with the results derived from the images. Two oscillation modes of the spray at a low frequency of 100 Hz and a high frequency of 1800 Hz were identified by analyzing the Mie scattering intensity in different regions. Those modes of oscillation could induce a variation of the local air/fuel ratio.

All the aforementioned studies[2-5,7,8,11] were conducted at one atmosphere without considering the effects of the elevated pressures typically encountered in operational liquid-propellant rocket engines. Strakey et al.[12] investigated the spray characteristics of swirl co-axial injectors over a broad range of liquid-to-gas momentum ratios (0.1-100) at a chamber pressure of 2.97 MPa using water and helium/nitrogen as propellant simulants. The spreading angle of the liquid spray decreases with the increase of the co-axial gas momentum, and appears almost identical to that produced by a shear co-axial injector at the lowest liquid-to-gas momentum ratio (0.1). The mean droplet size, however, becomes smaller compared with that of a shear co-axial injector at the same flowrate. Recently, Yoon and coworkers studied the effects of ambient gas density on the liquid-sheet spreading angle and breakup length of single swirl[13] and swirl co-axial[14] injectors. Water was employed as the oxidizer simulant. The measured spray angle prior to the sheet breakup remains almost fixed in the pressure range of 1-40 atm. The sheet breakup length, however, decreases with increasing pressure due to the enhanced aerodynamic force as the ambient gas density increases. Ela[15] conducted hot-fire experiments for multi-element swirl injectors with liquid oxygen and gaseous hydrogen at mixture ratios of 5.2-6.9 and a chamber pressure of 10.3 MPa. Results indicated that the C* efficiency increases with increasing mixture ratio. Hot-fire studies of liquid oxygen and gaseous hydrogen were also performed by Tamura and colleagues[16,17] for both single- and multi-element swirl injectors at moderate chamber pressures (2.6-3.5 MPa) and mixture ratios

of 4.0-8.0. It was reported that an enhanced C* efficiency could be obtained at a greater mixture ratio.

In addition to experimental studies, numerical simulations were recently performed to explore the flow evolution of swirl co-axial injectors. Kim and Heister[18] investigated hydrodynamic instabilities of the swirling liquid jet within the recessed region of a swirl co-axial injector. A locally homogeneous flow model, previously developed for treating flow instabilities in shear co-axial injectors,[19] was adopted, by assuming the thermodynamic and momentum equilibria between the gas and liquid phases throughout the entire flowfield. The approach also employed an incompressible-flow assumption with pre-specified gas and liquid densities. Real-fluid thermodynamics and property variations inherent in operational injector flows were not taken into account, to simplify the analysis. Initial results indicated that the swirling motion and fluctuation of the injected liquid became more pronounced with an increase in the gas-to-liquid density ratio. Park and Heister[20] simulated the free surface and spray shape of injected liquid in a swirl injector. The analysis was based on a boundary element method along with the assumption of an aixsymmetrical, inviscid, and incompressible flow. Calculated film thickness and spray cone angle agreed well with those predicted by the classical theory. Canino et al.[21] studied the flow development behind the center post in a swirl co-axial injector. Emphasis was placed on the vortex-shedding characteristics due to the bluff-body dynamics within the injector passage.

Although much useful information has been obtained about the liquid atomization and mixing characteristics of swirl co-axial injectors, most existing studies were conducted either at room temperatures using water as the oxidizer simultant,[2-5,7,8,11-14] or at hot-fire conditions[15-17] where the available diagnostics are limited by the difficulties in probing the flowfield in such a high-pressure, high-temperature environment. Very limited effort has been applied to investigate detailed injector flow dynamics under conditions representative of operational rocket engines, where the chamber pressure often exceeds the thermodynamic critical pressure of the injected fluid. Furthermore, the flow evolution within the injector has not been carefully explored, except for the analytic studies based on classical hydrodynamics theories discussed in Refs. 1 and [22] and numerical studies based on an incompressible-flow assumption.[18]

The purpose of the present work is to remedy these deficiencies by conducting high-fidelity simulations of cryogenic fluid dynamics of swirl injectors at supercritical pressures, mimicking the configurations and flow conditions of contemporary rocket engines using liquid oxygen (LOX) as the oxidizer.[23] The formulation accommodates full conservation laws, and takes into account real-fluid thermodynamics and transport phenomena. The specific objectives of the study are: 1) to characterize the detailed flow physics in the injector flow path; 2) to explore various underlying mechanisms dictating the fluid atomization and energy-transfer behaviors; and 3) to identify and prioritize key injector design attributes and operating conditions critical to the injector performance.

1.2 Theoretical Formulation

The basis of the present study is the general theoretical framework for treating supercritical fluid injection and mixing, as detailed by Meng et al.[24] and Zong et al.[25]

The approach has been used to investigate the transport and dynamics of droplets,[24] jet mixing,[25] and chemically reacting shear flows[26] over a broad range of thermodynamic states and flow conditions. In brief, the formulation accommodates complete conservation equations of mass, momentum, energy, and species transport. Full account is taken of general-fluid thermodynamics and transport phenomena over the entire temperature and pressure regimes of concern. Turbulence closure is achieved by means of a large-eddy-simulation (LES) technique, in which large-scale motions are calculated explicitly, and the effects of unresolved small-scale turbulence are modeled either analytically or empirically. The governing Favre-filtered conservation equations are derived by filtering small-scale dynamics from resolved scales over a well-defined set of spatial and temporal intervals.[27,28] The effects of subgrid-scale (*sgs*) motions are treated using the approach proposed by Erlebacher et al,[29] which employs a Favre-averaged generalization of the Smagorinsky eddy viscosity model. The Smagorinsky coefficient C_R (≈ 0.01) and C_I (≈ 0.007) are determined empirically.[30] It should be noted that accurate modeling of *sgs* dynamics under supercritical conditions remains a challenging task, due to complications arising from rapid property variations and real-fluid thermodynamics and transport. Very limited effort has been applied so far to quantify the effects of real-fluid thermodynamics on small-scale turbulent structures and a well-calibrated *sgs* model for supercritical fluid flows is currently not available. This issue will be addressed in our subsequent work.

The fluid volumetric behavior is evaluated using a modified Soave-Redlich-Kwong equation of state[31] because of its validity over a broad range of fluid states and simplicity of numerical implementation. Thermodynamic properties, such as enthalpy, Gibbs energy, and constant-pressure specific heat, are derived directly from fundamental thermodynamic theories. They are expressed as the sum of an ideal-gas property at the same temperature and a thermodynamic departure function accounting for dense-fluid correction.[32] Transport properties, such as viscosity and thermal conductivity, are estimated using an extended corresponding-state theory[33,34] along with a 32-term Benedict-Webb-Robin equation of state. Mass diffusivity is obtained by the Takahashi method calibrated for high pressure conditions.[35] The implementation and validation of the property evaluation schemes are detailed in Refs. 24 and 32.

1.3 Numerical Framework

The theoretical formulation outlined above is numerically solved by means of a preconditioning scheme incorporating a unified treatment of general fluid thermodynamics.[36] All the numerical properties, including the preconditioning matrix, Jacobian matrices, and eigenvalues, are derived directly from fundamental thermodynamics theories, rendering a self-consistent and robust algorithm. The numerical formulation can accommodate any equation of state, and is valid for fluid flows at all speeds and at all fluid thermodynamic states. Further efficiency is achieved by employing temperature instead of enthalpy as the primary dependent variable in the preconditioned energy equation.[37] This procedure eliminates laborious iterations in solving the equation of state for temperature, and consequently facilitates the load balance among computational blocks in a distributed computing environment. The resultant scheme is highly efficient and suitable for parallel processing.

The numerical framework employs a density-based, finite-volume methodology along with a dual-time-step integration technique.[38] Temporal discretization is obtained using a second-order backward differencing scheme, and the inner-loop pseudo-time term is integrated with a four-step Runge-Kutta scheme. Spatial discretization is achieved with a fourth-order, central-difference scheme in generalized coordinates.[39] A nine-point stencil is employed to evaluate the convective flux in each spatial direction to improve the spectral resolution of small-scale turbulence structures. Fourth-order scalar dissipation with the coefficient $\varepsilon_4 = 0.001$ is applied to ensure numerical stability with minimum contamination of the solution.

The overall accuracy of the present scheme within the context of LES was carefully assessed based on the decay of the kinetic energy of isotropic turbulence. Calculations were performed for an isotropic turbulent flow in a cubic box of a non-dimensional width of 2π. The experimental results of Comet-Bellot and Corrsin (CBC)[40] were selected as the benchmark with an initial Taylor Reynolds number of 80 on a $32 \times 32 \times 32$ grid. The predicted temporal evolution of turbulent kinetic energy agrees well with experimental data. The effects of numerical and *sgs* dissipation on the evolution of turbulent kinetic energy were further assessed by either turning those terms on or off or reducing the corresponding coefficients by one half. Results indicated that the dissipation associated with the *sgs* model overshadows that of the numerical scheme, and the numerical dissipation only serves to maintain numerical stability.

The present flowfield involves exceedingly large property gradients between the injected LOX and ambient gaseous oxygen. The density ratio may reach a level of 10 for a chamber pressure 100 atm. A second-order scalar dissipation with a total-variation-diminishing switch developed by Swanson and Turkel[41] was thus applied to suppress numerical oscillations in regions with steep property variations. Care was also exercised to ensure sufficient grid resolution for properly capturing the hydrodynamic instability waves inherent in the LOX film.

Finally, a multiblock domain decomposition technique, along with static load balance, is employed to facilitate the implementation of parallel computation with message passing interfaces (MPI) at the domain boundaries. The parallelization methodology is robust and the speedup is almost linear.

1.4 Injector Configuration and Boundary Conditions

The dynamics of liquid oxygen (LOX) injected through a pressure swirl injector into a free volume preconditioned with gaseous oxygen at a supercritical pressure is investigated. Figure 2 shows the physical model considered herein. It consists of three major parts: tangential inlets, a vortex chamber, and a discharge nozzle.[1,6] The baseline geometry and mass flowrate are summarized in Table 1, where R_s, R_n, and R_p denote the radii of the vortex chamber, discharge nozzle, and tangential inlet, respectively, and L the injector length. The parameters are chosen to be identical to those of the center element of the swirl co-axial injector in the RD-0110 liquid rocket engine, the third-stage engine for the Soyuz space launch vehicle.[42] The geometric characteristic constant, K, which determines the initial swirl strength of the injected fluid,[1] is defined as

$K \equiv A_n R_{in} / A_{in} R_n$, with A_n being the discharge nozzle area, A_{in} the total area of the tangential inlets, and R_{in} the radial location of the tangential entry.

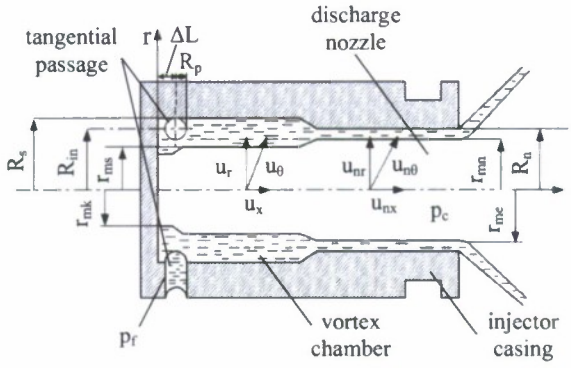

Fig. 2 Schematic of pressure swirl injector.

Table 1 Baseline geometry and mass flowrate

R_s (mm)	R_n (mm)	R_p (mm)	L (mm)	K	$\dot{m}$ (kg/s)
2.5	2.5	0.85	25	3.2	0.15

The computational domain includes the interior of the swirl injector and a downstream region measuring $8R_s$ and $40R_s$ in the radial and axial directions, respectively. Because of the enormous computational effort required for calculating the flow evolution in the entire regime, only a cylindrical sector with periodic boundary conditions specified in the azimuthal direction is treated. Such an axisymmetric simulation introduces several limitations: 1) the tangential inlets, which consist of six small circular ports on the injector wall, are simplified to a 1 mm wide slit on the radial boundary of the injector; 2) the flow variations in the azimuthal direction are neglected; 3) the vortex stretching mechanism, which is responsible for the energy transfer from large- to small-scale structures in the flowfield, is not considered. In spite of those limitations, previous studies[25,43] have indicated that the present numerical analysis is able to capture many unique mechanisms dictating supercritical fluid injection and mixing dynamics, including thermodynamic non-idealities, density stratification, interfacial instability, and baroclinic vorticity production. In addition, various important unsteady flow features, such as the interactions of hydrodynamic instabilities and acoustic oscillations within the swirl injector, are well explored in the present work. The results provide a quantitative basis for identifying the key processes and injector parameters that determine the liquid sheet breakup and atomization characteristics under supercritical pressures.

At the inlet, the bulk radial and azimuthal velocities are selected to match the mass flowrate, $\dot{m}$, and the swirl strength of the injected fluid, which is estimated based on the injector geometric constant, K. The fluid temperature is fixed and pressure is obtained through a one-dimensional approximation to the radial momentum equation

(i.e., $\partial p/\partial r = -\rho(\partial u_r/\partial t) - u_r(\partial u_r/\partial r) + u_\theta^2/r$). Turbulence is provided by superimposing broadband noise onto the mean velocity profiles. The disturbances are produced by a Gaussian random-number generator with an intensity of 8% of the mean quantities, sufficient to trigger the instabilities inherent in the flowfield. A white noise with a higher turbulence intensity (10%) is also considered for the baseline case (Case 1 in Table 2). No obvious changes in the injector flow dynamics are observed in terms of the spectral characteristics of flow-oscillations at different locations. At the downstream boundary, extrapolation of primitive variables from the interior may cause undesired reflection of numerical waves propagating into the computation domain. Thus, the characteristic boundary conditions proposed by Poinsot and Lele[44] for ideal gases and extended to real-fluid flows[37] are incorporated into the present preconditioning scheme, and a time-invariant back pressure is specified. At the radial boundary, the temperature and velocity components are extrapolated from the interior with a fixed ambient pressure. Because the computational domain is sufficiently large, the truncation effects of the radial and downstream boundaries on the injector near-field flow dynamics are negligible. Finally, the non-slip adiabatic conditions are enforced along the solid wall.

1.5 Results and Discussion

The liquid film thickness, h, and spreading angle, 2α, at the injector exit are often employed to characterize the performance of a swirl injector.[1] The former dictates the size of the fluid parcel after the film breaks up, and the latter affects the intra-element mixing efficiency. The spreading angle is defined as twice the apex angle of the asymptotic cone to the hyperboloid of revolution corresponding to the profile of the spray, and can be calculated by the ratio of the circumferential to the axial velocities at the injector exit, i.e., $\alpha \equiv \tan^{-1}(u_{e\theta}/u_{ex})$.[1] The key variables influencing the injector flow dynamics include the geometric constant, K, injector length, L, injector exit diameter, D_n, and thermophysical properties of the injected fluid, such as the density, ρ, and viscosity, μ. According to the Buckingham Pi theorem,[45] two dimensionless equations for the film thickness and spreading angle at the injector exit can be obtained in terms of those variables,

$$h/D_n = f(\rho_{inj}/\rho_\infty, \mu_{inj}/\mu_\infty, Re_L, K) \tag{1}$$

$$\alpha = \tan^{-1} u_{e\theta}/u_{ex} = f(\rho_{inj}/\rho_\infty, \mu_{inj}/\mu_\infty, Re_L, K) \tag{2}$$

where the subscripts *inj* and ∞ denote the injected-fluid and ambient conditions, respectively. The Reynolds number of the liquid film is defined as $Re_L = \rho_{inj} u_n L/\mu_{inj}$. Among those parameters, the density and viscosity ratios are fixed for a given flow condition. The geometric constant and injector length are determined by the injector configuration.

A parametric study is conducted to investigate the effects of injector geometry and operating condition on the liquid spray behavior over a pressure range of 100-200 atm. The LOX injection and ambient temperatures are fixed at 120 and 300 K, respectively. For reference, the critical pressure and temperature of oxygen are 50.4 atm

and 154.6 K, respcctively. Table 2 summarizes the injector configurations and flow parameters obtained from the present analysis. Also included for comparison are those predicted by classical swirl-injector theories for inviscid, incompressible flows (denoted by the subscript *inv*),[1] written in the following form,

$$h_{inv} = R_n(1-\sqrt{1-\varphi}) \tag{3}$$

$$\alpha_{inv} = u_{e\theta}/u_{ex} = \tan^{-1}\sqrt{2(1-\varphi)^2/[2-\varphi-2(1-\varphi)^2]} \tag{4}$$

Table 2 Effects of injector geometry and flow conditions on LOX film thickness and spreading anglc at injector exit (T_∞ = 300 K, and T_{inj} = 120 K).

Cases	p_∞ (atm)	L (mm)	ΔL* (mm)	K	$\dot{m}$ (kg/s)	Re_L (10^6)	h (mm)	2α (deg)	h_{inv} (mm)	$2\alpha_{inv}$ (deg)
1	100	25	2.0	3.2	0.15	5.4	0.686	73.8	0.56	92.2
2	100	25	2.0	3.2	0.10	3.8	0.660	73.6	0.56	92.2
3	100	25	2.0	3.2	0.20	7.6	0.632	73.2	0.56	92.2
4	100	25	2.0	3.2	0.25	9.5	0.611	73.0	0.56	92.2
5	100	25	0.5	3.2	0.15	5.7	0.660	76.0	0.56	92.2
6	100	25	4.5	3.2	0.15	4.9	0.672	74.4	0.56	92.2
7	100	50	2.0	3.2	0.15	11.0	0.709	73.4	0.56	92.2
8	100	75	2.0	3.2	0.15	16.0	0.738	72.0	0.56	92.2
9	100	100	2.0	3.2	0.15	22.0	0.796	69.8	0.56	92.2
10	100	25	2.0	4.2	0.15	5.8	0.595	87.0	0.50	103.6
11	150	25	2.0	3.2	0.15	5.0	0.612	72.4	0.56	92.2
12	200	25	2.0	3.2	0.15	4.8	0.586	71.8	0.56	92.2

* distance from the center of the tangential entry to the injector headend.

where the coefficient of passage fullness, φ, is defined as the fractional area filled by the injected fluid in the discharge nozzle,

$$\varphi = \frac{\pi(R_n^2 - r_{mn}^2)}{\pi R_n^2} = 1 - \frac{r_{mn}^2}{R_n^2} \tag{5}$$

As will be further elaborated, both the liquid-film thickness and sprcading angle are sole functions of the injector geometric constant, K, and independent of such operating parameters as mass flowrate, in accordance with classical hydrodynamics theories. The situation becomes substantially different in reality due to the existence of viscous loss and property variations. Since no distinct interface exists between thc injected fluid and gaseous core in a supercritical flow environment, to facilitate analysis, the numerically calculated LOX film boundary is defined as thc radial position above which the mass flowrate equals the specified value at the inlet. This dcfinition takes into account rapid fluid property variations and provides a quantitative basis for evaluating thc liquid-sheet formation and breakup processes. Because the detailed velocity information can be easily retrieved from the present analysis, the film spreading angle, α, is evaluated bascd on its definition, as the invcrse tangent of the ratio of the averaged azimuthal to axial velocity at the injector exit.

A typical simulation employs a 50×100 grid for the injector interior, and a 150×200 grid for the downstream exterior region. The grids are clustered near the wall and the injector exit to resolve steep gradients in these regions. The smallest grid size in the radial direction is 20 μm, which falls in the inertial sub-range of the turbulent kinetic energy spectrum estimated using the Kolmogorov-Obukhow theory. The computational domain is divided into 15 blocks, with each calculated on a single processor of a distributed-memory parallel computer. The physical time step is 1×10^{-2} ms and the maximum CFL number for the inner-loop pseudo-time integration is 0.7. Each simulation is conducted for 10 flow-through times for the entire domain (i.e., 0.1 s) to obtain statistically meaningful data.

A grid-independence study was performed for Case 1 as part of the validation procedure. The same numerical code, injector configuration, and flow conditions are considered using a fine mesh with a 75×160 grid for the injector interior and a 225×320 grid for the downstream exterior region. The mean grid resolution inside the injector is enhanced by 50% in each spatial direction. Figure 3 shows the radial distributions of the time-mean temperature, density, and axial and radial velocity components at different axial locations. Results for the two different grid systems are in close agreement. The maximum derivation in the entire domain is less than 5%. The effect of grid resolution on the dynamical behavior of the injector flow was also examined. The maximum relative error is 3% for both the length and speed of the hydrodynamic instability wave within the liquid film. The differences of the frequency and magnitude of the dominant pressure oscillations induced by flow instabilities are less than 5%. The results indicate that the injector dynamics have been well captured and the grid system employed is appropriate in the present work.

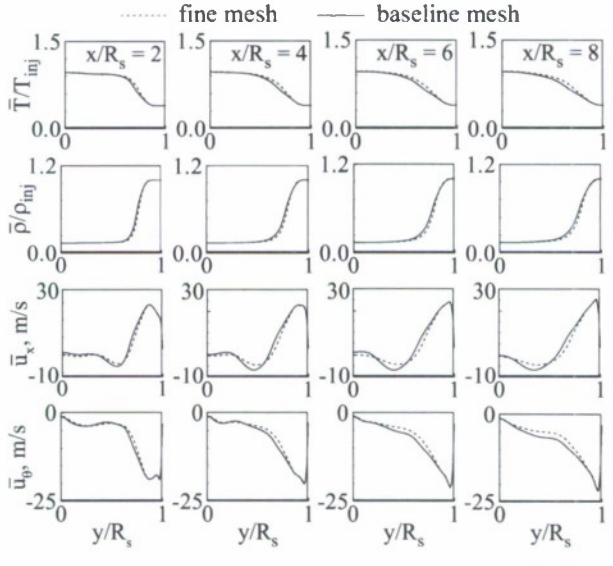

Fig. 3 Effect of grid resolution on radial distributions of mean temperature, density, and axial and radial velocity components at different axial locations (Case 1: $p_\infty = 10\,MPa$, $T_{inj} = 120\,K$, $T_\infty = 300\,K$, $\dot{m} = 0.15\,kg/s$, $\Delta L = 2.0\,mm$).

1.5.1 Injector Flow Dynamics

Figure 4 shows the temporal evolution of the temperature field for Case 1 (thc baseline case). Liquid oxygen is introduced tangentially into the injector. The swirl-induced centrifugal force prevents the injected fluid from penctrating into the center, and consequently gives rise to the formation of a gaseous core (referred to as cavity). A thin liquid film forms, convects downstream along the wall according to the conservation of mass and momentum, and exits from the injector as a nearly conical sheet. Several different typcs of flow oscillations are observed. The LOX film is intrinsically unstable and features three-dimensional hydrodynamic instability waves in both thc longitudinal and circumferential directions.[46] The circumfercntial mode, however, can not be observed in the present axisymmetric simulation. The longitudinal instability wave

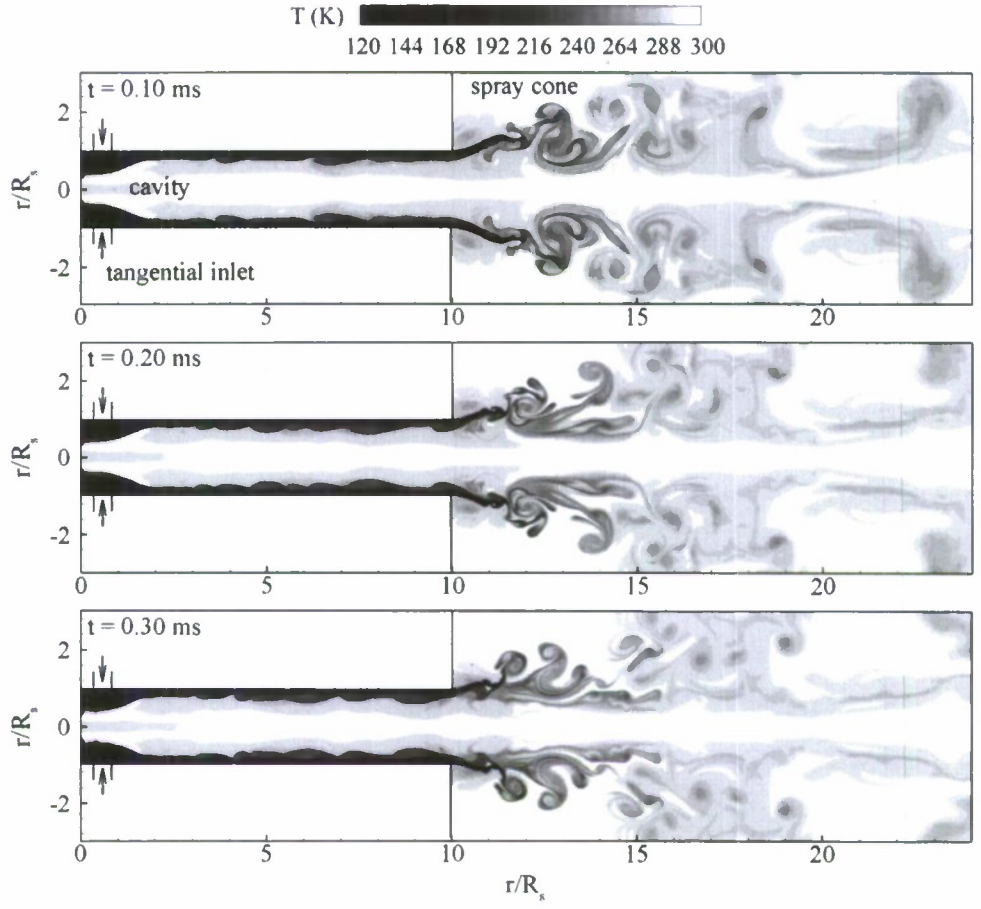

Fig. 4 Temporal evolution of temperature field (Case 1: $p_\infty = 10\,MPa$, $T_{inj} = 120\,K$, $T_\infty = 300\,K$, $\dot{m} = 0.15\,kg/s$, $K = 3.2$, $\Delta L = 2.0\,mm$).

propagates within the film in a form similar to the shallow-watcr wave for an incompressible flow, and induces oscillations of the circumferential velocity in both the axial and radial directions, which are then convected downstream with the mean flow.

As the liquid film is discharged from the injector to the chamber, the Kelvin-Helmholtz type of instability emerges in the LOX sheet, and subsequently leads to sheet breakup and droplet formation. In addition, the injector is acoustically connected with the downstream chamber. Any acoustic oscillation in the chamber may propagate upstream into the injector and affect the LOX film behavior by influencing the mass flowrate of the injected fluid.[1,6] Furthermore, strong acoustic resonance occurs if the natural frequencies of the injector and chamber match each other.[47]

Figure 5 shows a close-up view of the temperature evolution near the LOX film for the baseline case, indicating the presence of the longitudinal mode of the hydrodynamic instability. The wave grows and develops to large-scale billows as it

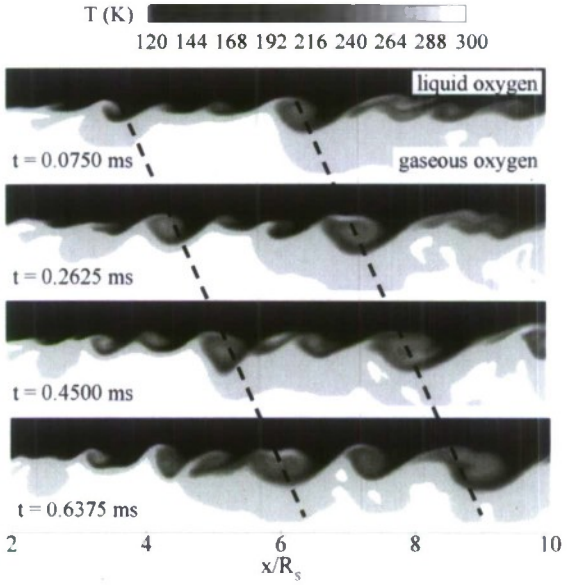

Fig. 5 Close-up view of temporal evolution of temperature field near liquid-oxygen film (Case 1: $p_\infty = 10\ MPa$, $T_{inj} = 120\ K$, $T_\infty = 300\ K$, $\dot{m} = 0.15\ kg/s$, $K = 3.2$, $\Delta L = 2.0\ mm$).

convects downstream. The calculated wave speed is approximately 10 *m/s* in the region of $2 \le x/R_s \le 9$, where the LOX film is well developed and its time-mean thickness varies slowly. A wave equation characterizing the hydrodynamic instability of a swirling liquid film can be established based on linearized conservation laws. For an inviscid, incompressible flow, with the neglect of the radial velocity and the assumption of an infinitesimal film thickness compared to the wave length, the wave equation becomes[6]

$$\frac{\partial^2 \xi}{\partial t^2} = \frac{1}{r_m^4} u_{in}^2 R_{in}^2 \left(\frac{R_s^2 - r_m^2}{2}\right) \frac{\partial^2 \xi}{\partial x^2} \tag{6}$$

where ξ is the instantaneous displacement of the film surface, and r_m the radial distance between the injector centerline and the time-mean film surface, and u_{in} the injection

velocity at the tangential inlet. The form of the wave speed bears a close resemblance to that for shallow-water wave propagation,[6]

$$a = \sqrt{(\frac{u_{in}^2 R_{in}^2}{r_m^3})(\frac{R_s^2 - r_m^2}{2r_m})} \tag{7}$$

The first parenthesized term in the square root represents the centrifugal force and the second term the effective thickness of the liquid film. Equation (7) results in a wave speed of 6.6 *m/s* based on the values of u_{in} and r_m (11 m/s and 1.9 mm, respectively). The classical hydrodynamics theory underpredicts the wave speed due to the neglect of fluid compressibility and viscous effects.

The frequency spectra of pressure fluctuations provide a more quantitative insight into the various types of instability waves involved. Figure 6 presents the results obtained at eight different positions within the injector. A small peak at 14 kHz is

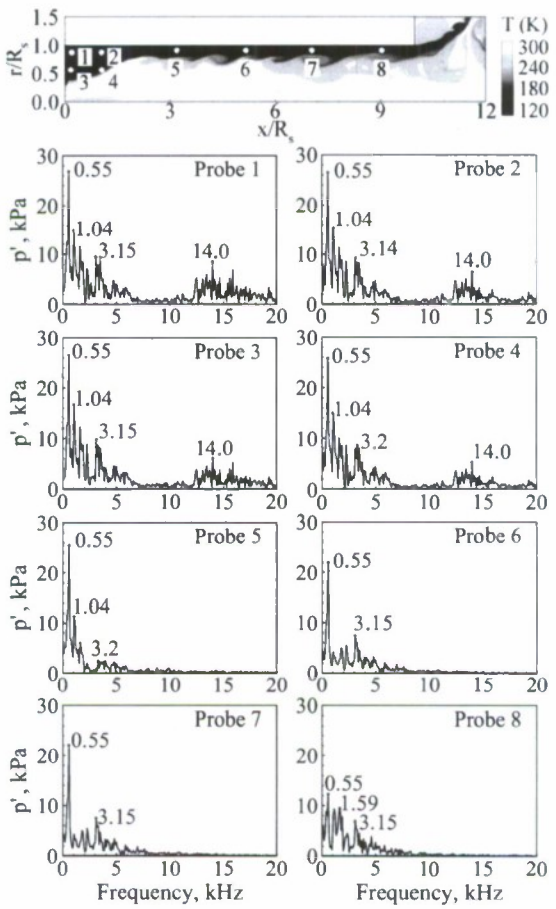

Fig. 6 Power spectral densities of pressure fluctuations at eight different locations inside injector (Case 1: $p_\infty = 10\ MPa$, $T_{inj} = 120\ K$, $T_\infty = 300\ K$, $\dot{m} = 0.15\ kg/s$, $K = 3.2$, $\Delta L = 2.0\ mm$).

observed at probes 1-4, resulting from the recirculating LOX flow between the tangential inlet and the injector head-end. This high-frequency oscillation is confined within the upstream region. It decays rapidly and disappears as the LOX film moves downstream due to viscous dissipation. Two dominant modes at the frequencies of 0.55 and 3.15 kHz are observed at all the probe locations. The former is closely related to the longitudinal wave of hydrodynamic instability within the LOX film. In the present case, the wave propagation speed is about 10 m/s, and the time for a disturbance to travel through the LOX film within the injector (i.e., from the tangential entry to the injector exit) is on the order of 2 *ms*. This leads to a characteristic frequency of 500 Hz for the longitudinal hydrodynamic instability. The result shows good agreement with the calculated frequency of 550 Hz. Figure 7 presents the frequency contents of the pressure and velocity fluctuations at Probe 6. Both the axial and azimuthal velocities correlate closely with the pressure signal. As the wave propagates downstream, the local axial velocity and pressure also fluctuate to satisfy the conservation of the mass and momentum. The ensuing variation of the film thickness then causes the azimuthal velocity to oscillate in accordance with the conservation of mass and angular momentum. The lack of noticeable oscillations of the radial velocity in the low-frequency range may be attributed to the small thickness of the LOX film.

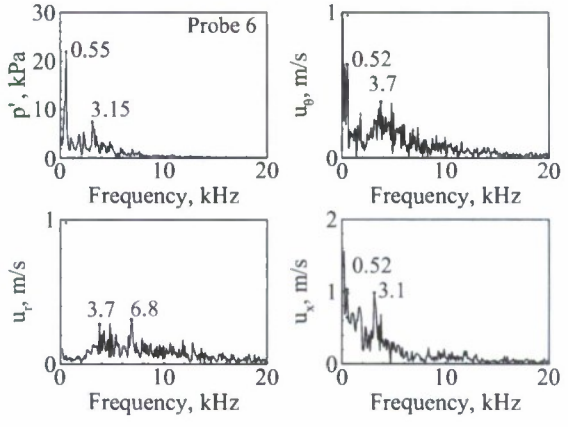

Fig. 7 Power spectral densities of pressure and velocity fluctuations at probe 6 (Case 1: $p_\infty = 10\ MPa$, $T_{inj} = 120\ K$, $T_\infty = 300\ K$, $\dot{m} = 0.15\ kg/s$, $K = 3.2$, $\Delta L = 2.0\ mm$).

The harmonic of 3.15 kHz shown in the frequency spectral of Fig. 6 may arise from the acoustic oscillation in the injector. The injector configuration considered in the present study can be treated acoustically as a quarter-wave resonator having a natural frequency

$$f = c/4(L + \Delta l) \tag{8}$$

where c is the speed of sound in the gaseous oxygen core, L the injector length. A correction factor, Δl, which is usually taken as $0.6R_n$, is employed to account for the effect of gaseous oxygen immediately downstream of the injector exit on the acoustic resonance of the injector. Under the present flow conditions of $c = 340\ m/s$, $L = 25\ mm$, and $\Delta l = 1.5\ mm$, the resonance frequency becomes 3.2 kHz, almost identical to the observed harmonic in Fig. 6. Figure 8 shows the time histories of

pressure oscillations at Probes 5-8. The low-frequency (0.55 kHz) hydrodynamic wave decays considerably in the downstream region, while the acoustic-driven, high-frequency (3.15 kHz) instability retains its magnitude in the entire LOX film.

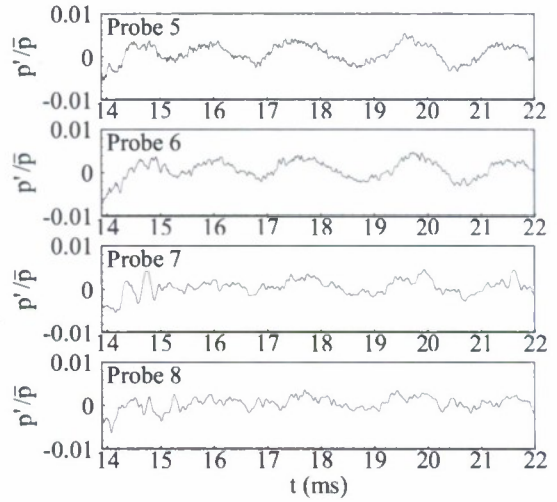

Fig. 8 Time histories of pressure oscillations at four different locations along liquid-oxygen film (Case 1: $p_\infty = 10\,MPa$, $T_{inj} = 120\,K$, $T_\infty = 300\,K$, $\dot{m} = 0.15\,kg/s$, $K = 3.2$, $\Delta L = 2.0\,mm$).

Figure 9 shows the spectra contents of flow oscillations in the near-field of the injector. A dominant frequency of 1.04 kHz is observed at all probes. This phenomenon

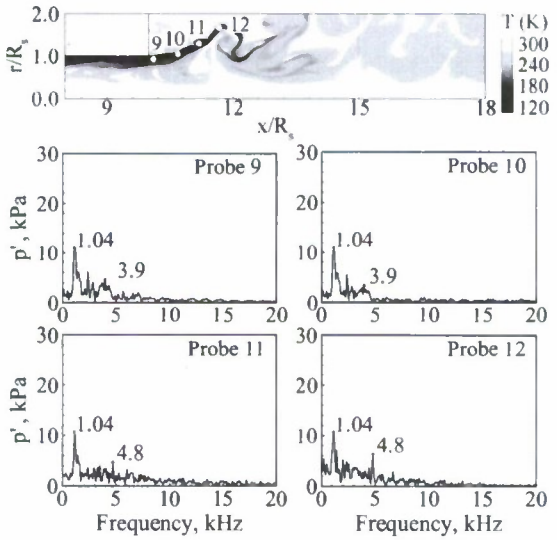

Fig. 9 Power spectral densities of pressure fluctuations at four different locations in ncar-field of injector (Case 1: $p_\infty = 10\,MPa$, $T_{inj} = 120\,K$, $T_\infty = 300\,K$, $\dot{m} = 0.15\,kg/s$, $K = 3.2$, $\Delta L = 2.0\,mm$).

can be attributed to the precession of the vortex core in the central toroidal recirculation zone (CTRZ) immediately downstream of the injector exit.[48] The resultant oscillation then excites flow instabilities inside the injector, as evidenced in the frequency spectral given in Fig. 6. The LOX sheet, once it exits from the injector, is subject to the Kelvin-Helmholtz type of instability. A peak around 3.9 kHz (Probes 9-10) exists along the LOX sheet, which subsequently develops to 4.8 kHz (Probes 11-12) as the liquid travels downstream. The vortex-shedding frequency can be roughly estimated using the following empirical correlation,[49]

$$f_n = St \cdot \bar{U} / \theta \tag{9}$$

where the Strouhal numer, St, ranges from 0.044 to 0.048 for turbulent flows. In the present study, the mean velocity, $\bar{U}$, is around 10 m/s, and the momentum thickness of the conic sheet is around 0.08 mm. The most unstable frequency, f_n, is predicted to be 5.75 kHz, which is comparable with the calculated frequency.

The injector flow dynamics are further explored using the proper-orthogonal-decomposition (POD) technique, which extracts energetic coherent structures from the calculated flowfields. For a given flow property, $f(\boldsymbol{r},t)$, the POD analysis can determine a set of orthogonal functions φ_j, $j = 1, 2, \cdots$, such that the projection of f onto the first n functions

$$\hat{f}(\boldsymbol{r},t) = \bar{f}(\boldsymbol{r}) + \sum_{j=1}^{n} a_j(t)\varphi_j(\boldsymbol{r}) \tag{10}$$

has the smallest error, defined as $E(\|f - \hat{f}\|^2)$. Here, $a_j(t)$ represents the temporal variation of the jth mode, and $E(\cdot)$ and $\|\cdot\|$ denote the time average and norm in the L^2 space, respectively. The function f can be extended to a vector by introducing an appropriate inner product on $\vec{F}$. A more complete discussion of this subject can be found in Refs. [50] and [51].

The method of snapshots is implemented to compute the POD modes. The database for the POD analysis contains a total of 320 snapshots of the flowfield within the injector. The time interval between snapshots is 50 μs, compared with the time step of 5 μs employed in the numerical simulations.

Figure 10 presents the energy distribution of the POD modes for the oscillatory pressure field of the baseline case. Here the energy of the jth mode, E_j, is defined as

$$E_j = E(\|a_j(t)\varphi_j(\boldsymbol{r})\|^2) \tag{11}$$

The first six POD modes capture more than 95% of the total energy of the oscillatory flowfield. The frequency spectra of the time-varying coefficients, $a_j(t)$, of these modes are shown in Fig. 11. A dominant frequency of 0.55 kHz is observed for the first mode, which is close to the characteristic frequency of the longitudinal hydrodynamic instability wave in the LOX film. The second and third modes are associated with the oscillations resulting from the precession of the toroidal recirculating flow downstream of the injector exit. The fourth and fifth modes have the identical frequency of 3.5 kHz, corresponding

to the natural acoustic oscillations within the injector. It should be noted that the frequency contents of the POD modes deviate slightly from those presented in Fig. 6 (i.e., pressure oscillations in the LOX film). The POD analysis is concerned with the entire field, and consequently provides results in a volume-average sense, as opposed to results at selected points (Fig. 6). The discrepancy becomes more noticeable in the present study, in which the flowfield is highly non-homogeneous with a steep density stratification across the LOX film surface. Another factor contributing to the difference between Figs. 6 and 11 is the limited temporal resolution of the POD analysis, especially for the high-frequency modes.

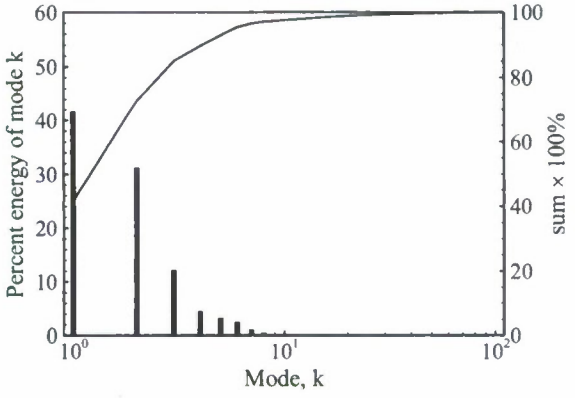

Fig. 10 Energy distribution of POD modes of pressure oscillations within injector (Case 1: $p_\infty = 10\ MPa$, $T_{inj} = 120\ K$, $T_\infty = 300\ K$, $\dot{m} = 0.15\ kg/s$, $K = 3.2$, $\Delta L = 2.0\ mm$).

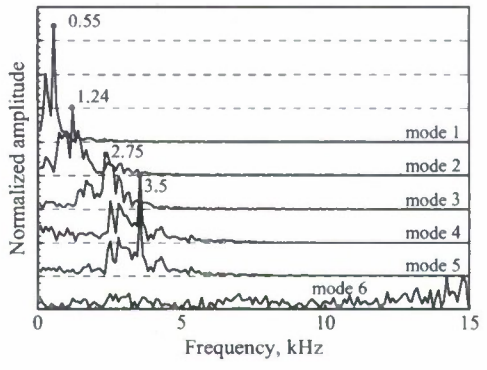

Fig. 11 Frequency spectra of time-varying coefficients of first six POD modes of pressure oscillations (Case 1: $p_\infty = 10\ MPa$, $T_{inj} = 120\ K$, $T_\infty = 300\ K$, $\dot{m} = 0.15\ kg/s$, $K = 3.2$, $\Delta L = 2.0\ mm$).

Figure 12 shows the spatial distributions (i.e., mode shapes) of the first six modes of the oscillatory pressure field in the injector. The first mode shape is nearly one-dimensional and exhibits a decaying distribution with a maximum at the head and a diminished value at the exit. The results corroborate the intimate relationship between the hydrodynamic instability wave in the LOX film and the unsteady field in the gaseous core. Any hydrodynamic disturbance in the liquid film may cause variations of the film

thickness, which in turn produces pressure fluctuations in the free volume of the injector, mainly due to the volume dilation across the film surface induced by the local temperature changes (see Fig. 5). The second and third modes are attributed to the excitation by the precession vortex core in the near-field of the injector exit. The fourth and fifth modes bear quite similar structures, but with a phase difference of $\pi/2$ in both time and space. This suggests the existence of a standing wave in the injector. The sixth mode reveals a dipole-like structure surrounding the tangential entry near the injector headend. The associated high-frequency oscillation is basically confined in the upstream region, and decays rapidly as the fluctuation propagates downstream.

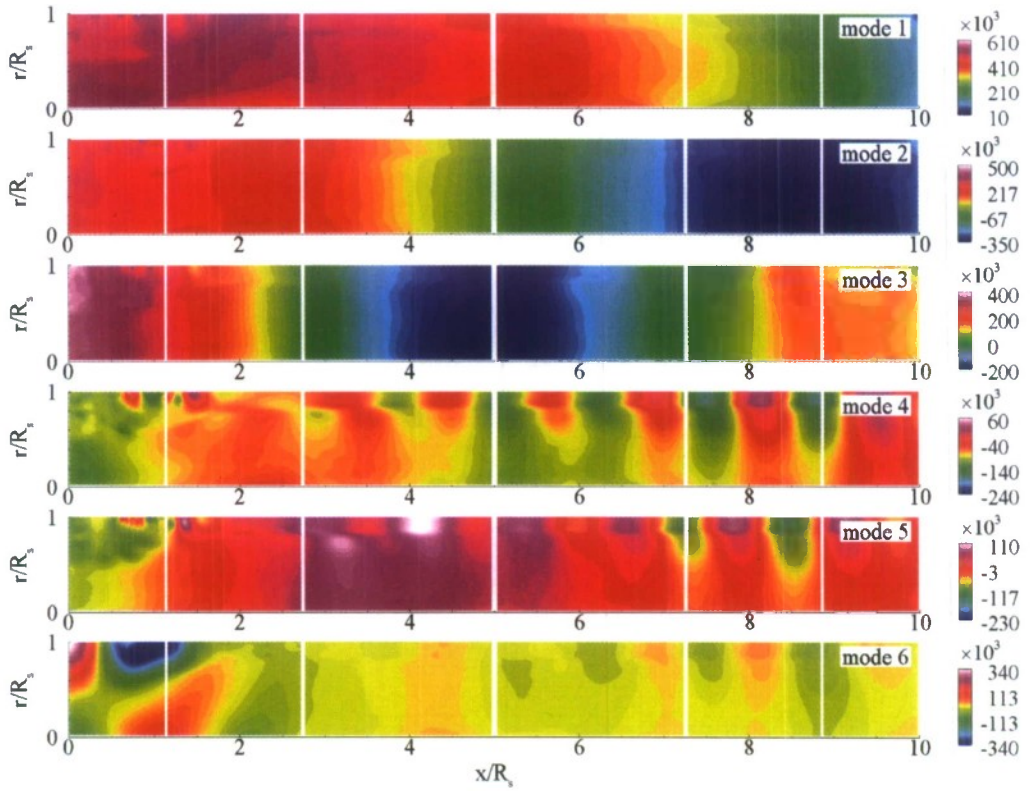

Fig. 12 Spatial distributions of first six POD modes of oscillatory pressure field within injector (Case 1: $p_\infty = 10\,MPa$, $T_{inj} = 120\,K$, $T_\infty = 300\,K$, $\dot{m} = 0.15\,kg/s$, $K = 3.2$, $\Delta L = 2.0\,mm$).

1.5.2 Mean Flow Properties

Figure 13 shows the time-mean fields of the density, temperature, compressibility factor, and velocities for Cases 1 and 10. The corresponding geometric parameters, K, are 3.2 and 4.2, respectively. The critical isothermal surface of oxygen at $T_c = 154\,K$, as denoted by the dashed line, is also presented, to provide a reference for the LOX film boundary. The dense fluid film near the wall and gaseous core in the cavity are clearly observed. The LOX sheet mixes promptly with the warm gas soon after exiting from the

injector, instead of penetrating deeply into the chamber. Rapid volume dilation and property variations take place when the LOX mixes with the surrounding gaseous oxygen and the local temperature transits across the inflection point on the isobaric line in the

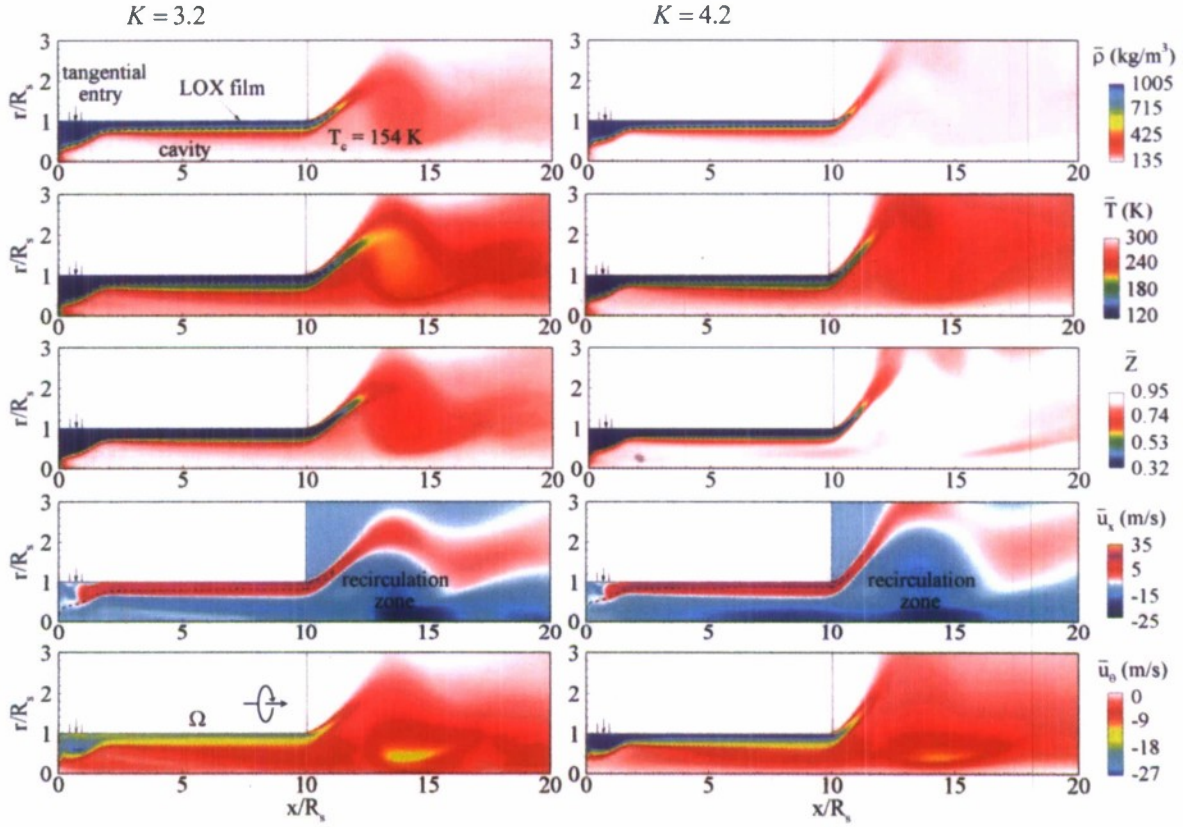

Fig. 13 Time-mean fields of density, temperature, compressibility factor, and velocity components ($p_\infty = 10\ MPa$, $T_{inj} = 120\ K$, $T_\infty = 300\ K$, $\dot{m} = 0.15\ kg/s$, $\Delta L = 2.0\ mm$).

thermodynamic ρ-T diagram. Figure 14 shows the radial distributions of the time-mean flow properties at various axial locations for Case 1. The velocity field indicates the presence of a swirling gaseous flow downstream of the injector exit, where the adverse pressure gradient in the axial direction produces a recirculation zone. Owing to the relatively low pressure in this region, the LOX sheet, which initially expands outward in the radial direction, converges toward the centerline, until the radial pressure gradient is balanced by the centrifugal force. As the swirl strength increases with K varying from 3.2 to 4.2, the film thickness decreases, but the spreading angle becomes wider. The recirculation zone downstream of the exit is enlarged and even extended into the injector. A similar situation was observed by Panda and Mclaughlin[52] in their experimental study on swirling-jet instabilities at a swirl number of 0.5 and a Reynolds number of 57000.

Figure 15 shows the distribution of the LOX film thickness along the injector wall for Case 1, defined based on the injected mass flow rate of 0.15 kg/s and local fluid density and axial velocity. Three different flow regimes exist within the injector. In the

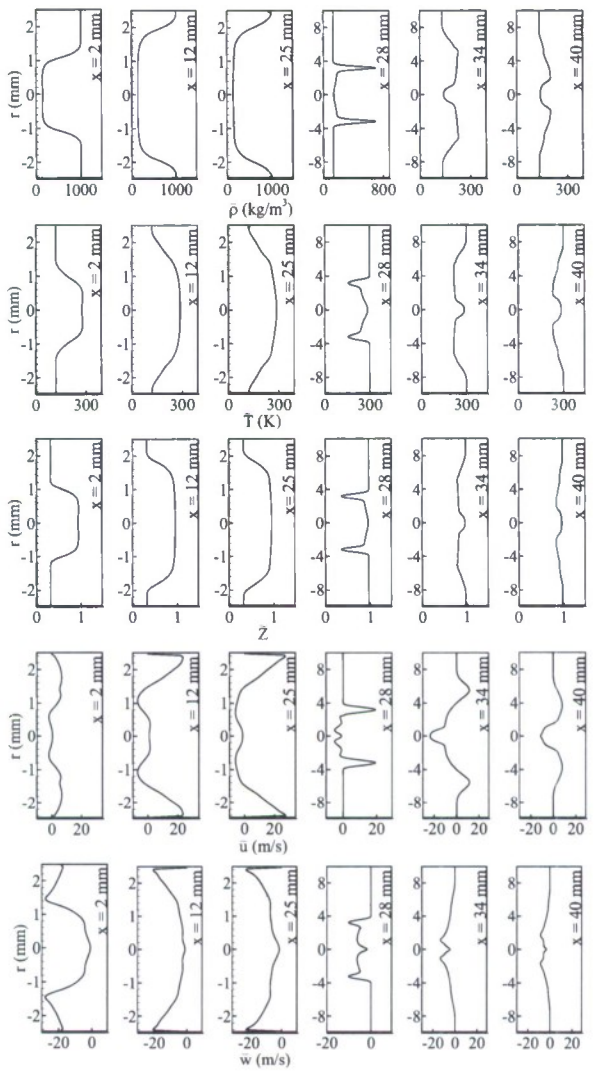

Fig. 14 Radial distributions of mean velocity components, temperature, density and compressibility-factor at various axial locations (Case 1: $p_\infty = 10\,MPa$, $T_{inj} = 120\,K$, $T_\infty = 300\,K$, $\dot{m} = 0.15\,kg/s$, $K = 3.2$, $\Delta L = 2.0\,mm$).

developing region ($0 \le x/R_s \le 2$) close to the injector head end, the injected LOX initially occupies a substantial fraction of the free volume, due to the small axial velocity. The fluid then converges toward the wall and forms a thin film. Downstream of the tangential inlet at $2 \le x/R_s \le 9$, a stationary regime emerges, in which the radial distributions of the flow properties vary slowly along the axial direction. The film thickness increases gradually due to the decreased axial velocity caused by viscous friction and reduced fluid density resulting from local heat transfer. Finally, as the static pressure induced by the swirling motion is converted into axial momentum close to the injector exit, the axial velocity increases and the film thickness decreases in the

acceleration region ($9 \le x/R_s \le 10$). Also included in the figure is the critical isotherm of oxygen. Thc heat transfer from the warm ambient gas to the LOX film causes the critical isothermal surface to regress toward the injector wall.

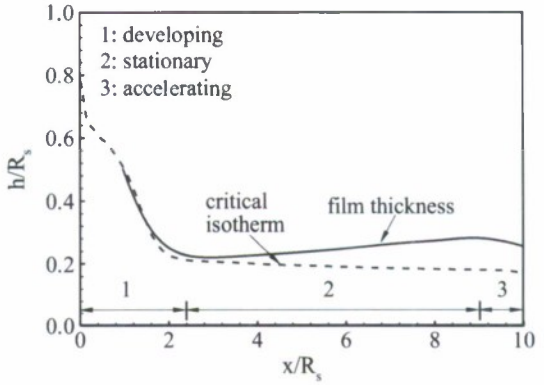

Fig. 15 Liquid-oxygcn film thickness along injector wall (Case 1: $p_\infty = 10\ MPa$, $T_{inj} = 120\ K$, $T_\infty = 300\ K$, $\dot{m} = 0.15\ kg/s$, $K = 3.2$).

Figure 16 shows the axial distributions of the time-averaged axial and angular momenta of the LOX film. The flow motions in both the axial and azimuthal directions are weak close to the headend. The angular momentum then increases rapidly and rcaches its maximum at the trailing edge of the tangential inlet. The injected LOX is driven toward the wall by the centrifugal force and accelerates downstream according to the conservation of mass. As a consequence, the axial momentum of the LOX film

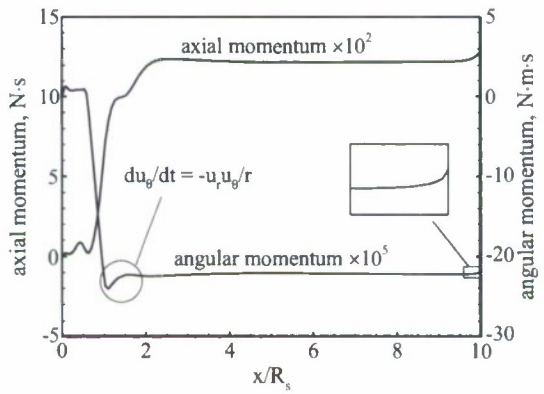

Fig. 16 Axial distributions of time-mean axial and angular momenta (Case 1: $p_\infty = 10\ MPa$, $T_{inj} = 120\ K$, $T_\infty = 300\ K$, $\dot{m} = 0.15\ kg/s$, $K = 3.2$).

increases rapidly. Thc transport of azimuthal momentum is more complicated and can be described by the following equation,

$$\frac{du_\theta}{dt} = -\frac{1}{\rho}\frac{\partial p}{\partial \theta} + \nu(\nabla^2 u_\theta + \frac{2}{r^2}\frac{\partial u_r}{\partial \theta} - \frac{u_\theta}{r^2}) - \frac{u_r u_\theta}{r} \qquad (12)$$

The first term on the right hand side of Eq. (12) represents the pressure gradient in the azimuthal direction, which vanishes in the present axisymmetrical simulation. The second term denotes viscous dissipation. The third term accounts for the transfer between the radial and azimuthal momenta. This quantity vanishes in the stationary region, in which u_r is practically zero in the LOX film. The small variations of the angular momentum downstream of the tangential entry and near the injector exit (the accelerating region) arise from the rapid change of u_r in those regions.

Based on classical hydrodynamics theories, the axial, u_{ex}, and azimuthal, $u_{e\theta}$, velocities at the injector exit for an incompressible inviscid fluid can be written as follows,[1]

$$u_{ex} = \sqrt{1-2(1-\varphi)^2/(2-\varphi)} \tag{13}$$

$$u_{e\theta} = \sqrt{2(1-\varphi)^2/(2-\varphi)} \tag{14}$$

where the coefficient of passage fullness, φ, is a function of the geometrical constant, K.

$$K = (1-\varphi)\sqrt{2}/\varphi\sqrt{\varphi} \tag{15}$$

Combining of Eqs. (13) and (14) gives the spreading angle of the liquid sheet at the injector exit, as defined in Eq. (4). The LOX film thickness and spreading angle are determined solely by the injector geometry and are independent of operating conditions. The situation for a real fluid, as treated in the present study, however, may be quite different, due to the many underlying assumptions in classical theories. Figure 17 presents the radial distributions of the time-averaged density, axial velocity, and azimuthal velocity in the stationary region ($x/R_s = 5$) for Case 1. The discrepancies between the classical theories and the results of the present work are obvious. Nonetheless, classical hydrodynamic analysis provides much useful information about the flow physics and can serve as an effective guideline for treating injector flow dynamics.

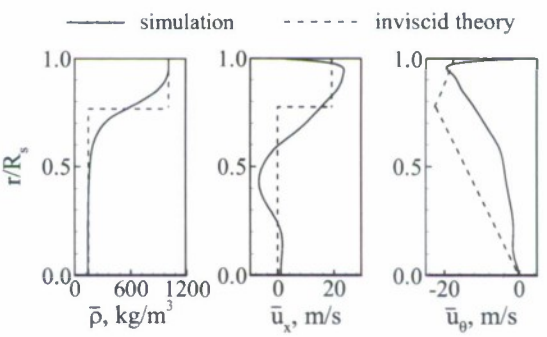

Fig. 17 Radial distributions of mean density and velocity components in the stationary region, $x/R_s = 5$ (Case 1: $p_\infty = 10\,MPa$, $T_{inj} = 120\,K$, $T_\infty = 300\,K$, $\dot{m} = 0.15\,kg/s$, $K = 3.2$, $\Delta L = 2.0\,mm$).

1.5.3 Effects of Flow Conditions and Geometry on Injector Behavior

The effects of LOX mass flowrate on the injector dynamics are studied in Cases 1 through 4 (see Table 2). Consistent with classical hydrodynamic theory, the calculated film thickness decreases slightly with increasing mass flowrate. The spreading angle, however, is almost independent of the variation in mass flowrate. Since both the viscous and compressibility effects are neglected, classical theory under-predicts the film thickness and over-predicts the spreading angle.

The influence of the tangential inlet position on the injector performance is explored through Cases 1, 5, and 6. Figure 18 shows the corresponding axial distributions of the axial- and angular-momenta of the LOX film. A more severe viscous loss, as measured by the relatively smaller increase of the axial momentum, is observed for Case 5 ($\Delta L = 0.5\ mm$) because the tangential inlet is directly attached to the headend. A similar situation occurs if the tangential inlet is placed farther downstream (Case 6, $\Delta L = 4.5\ mm$). Under this condition, a more substantial part of the injected fluid is delivered upstream to fill the volume between the inlet and the headend and forms a recirculation region there. This is manifested by the instantaneous streamlines close to the headend for Cases 5 and 6 in Fig. 19. The information obtained suggests that an optimal position for the tangential inlet exists to minimize the momentum loss. The film thickness and spreading angle at the injector exit are insensitive to the location of the tangential entry.

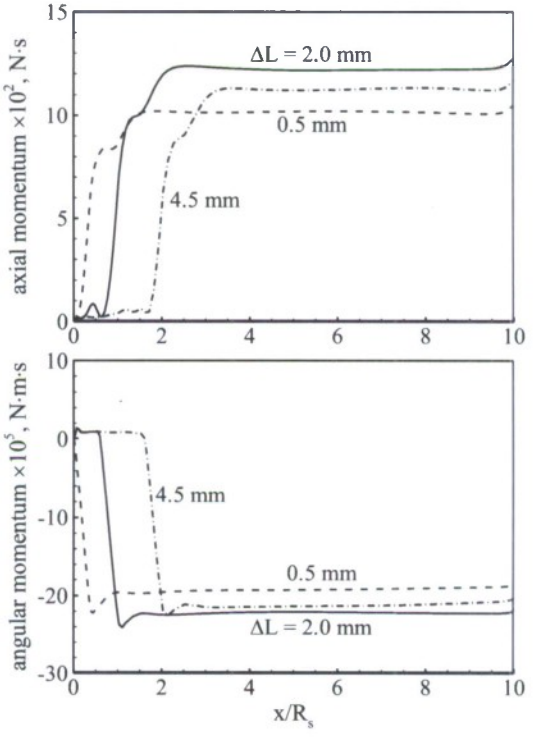

Fig. 18 Effect of tangential inlet location on mean axial and angular momentum distributions ($p_\infty = 10\ MPa$, $T_{inj} = 120\ K$, $T_\infty = 300\ K$, $\dot{m} = 0.15\ kg/s$, $K = 3.2$).

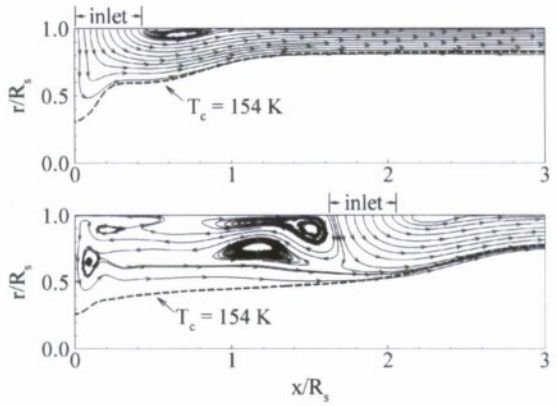

Fig. 19 Effect of tangential entry position on flow evolution near the head end ($p_\infty = 10\,MPa$, $T_{inj} = 120\,K$, $T_\infty = 300\,K$, $\dot{m} = 0.15\,kg/s$, $K = 3.2$).

For injectors with large length-to-diameter (aspeet) ratios, the viscous loss along the wall exerts a substantial impact on the injection process and henee alters the atomization efficiency and spray distribution. Figure 20 shows the relative axial- and angular-momentum losses as a function of the injeetor length (Cases 1, 7, 8, and 9). The losses are defined as the relative drops of the momenta at the injeetor exit in reference to the corresponding values at the beginning of the stationary region (i.e., $x/R_s = 2$). For

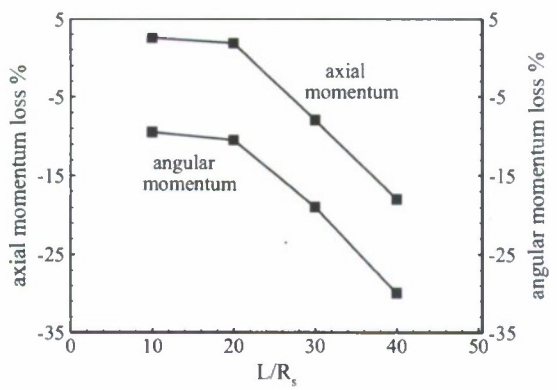

Fig. 20 Mean axial and angular momentum losses as functions of injector length ($p_\infty = 10\,MPa$, $T_{inj} = 120\,K$, $T_\infty = 300\,K$, $\dot{m} = 0.15\,kg/s$, $K = 3.2$).

the two shorter injectors ($L/R_s = 10$ and 20), the axial momentum at the injeetor exit is even greater than that at the beginning of the stationary region. This phenomenon may bc attributed to the transformation of the swirl-indueed static pressure to the axial momentum within the aceeleration regime. Sinee the azimuthal veloeity is influeneed by both the viscous dissipation and defleetion of fluid in the radial direction, the angular momentum experiences a morc severe decay than its axial counterpart. An increase in the injector length narrows the spreading angle. The simulation results for Cases 1 and 7-9 indicate that an elongation of thc injector has three negative impacts: (1) greater

momentum losses; (2) thickened liquid film and enlarged mean droplet size; and (3) reduced sheet spreading angle.

Figure 21 shows the LOX film thickness at the injector exit as a function of the injector length. Classical hydrodynamic theory under-estimates the film thickness by almost 30%, especially for longer injectors. An improved estimation is given by the empirical correlation suggested by Inamura et al.,[22] in which viscous loss is taken into account, but the influence of property variations under supercritical conditions is neglected. The latter accounts for the approximately 10% difference between the present analysis and classical theory.

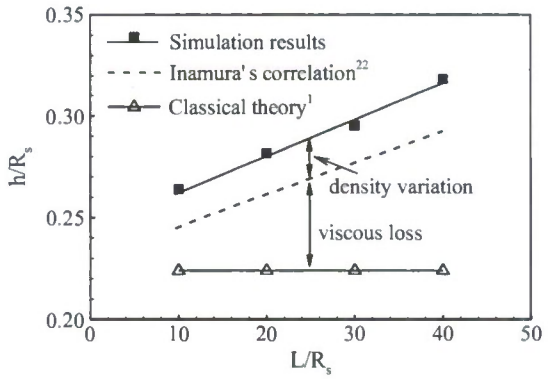

Fig. 21 LOX film thickness as function of injector length.

Two different injector geometrical constants of K=3.2 and 4.2 are examined in Cases 1 and 10, respectively. The mean flow properties are presented in Fig. 13. A greater geometric constant, in general, results in a stronger swirling motion, which eventually gives rise to a thinner liquid film and a wider spreading angle. Since the mixing region downstream of the injector is expanded, a better injector performance is achieved.

The effects of ambient pressure on the swirl injector behavior are investigated for three different pressures of 100, 150, and 200 atm (i.e., Cases 1, 11 and 12). As the ambient pressure increases, the momentum transfer between the LOX film and surrounding gases becomes stronger, and the momentum loss thus increases. Consequently, the film spreading angle decreases from 73.8 degrees for 100 atm to 71.8 degrees for 200 atm. On the other hand, the elevated pressure tends to retard the gasification of oxygen and reduce the low-density region within the LOX film. The net result leads to a decreased film thickness with increasing pressure. The overall trend is consistent with the experimental observations of Kim et al.[14]

1.6 Summary

The flow dynamics of liquid oxygen in a pressure swirl injector with tangential entry has been investigated by means of a comprehensive numerical analysis. The formulation incorporates real-fluid thermodynamics and transport into the conservation laws to render a self-consistent approach valid for any fluid thermodynamic state.

The flow development in the injector broadly involves three different stages. Liquid oxygen is introduced to the injector through the tangential inlet, and occupies a bulk of the injector volume in the developing region near the headend. A thin liquid film then forms, due to centrifugal force, and convects downstream along the wall in accordance with the conservation of mass and momentum. The flow properties and film thickness vary slightly in this stationary region. Finally, the LOX flow accelerates in the axial direction as the swirl-induced pressure converts to axial momentum close to the injector exit.

Several different types of instability waves were identified to provide direct insight into the mechanisms dictating the injector flow dynamics. These include hydrodynamic instabilities in both the axial and azimuthal direction within the LOX film, acoustic waves in the gaseous core, shear-layer instabilities in the LOX sheet downstream of the injector exit, and swirling LOX-sheet induced flow recirculation near the injector exit. The interactions between those flow oscillations and their influences on the injector flow behavior were examined systematically using the spectral and proper-orthogonal-decomposition techniques.

A parametric study was also performed to investigate the effects of flow conditions and injector geometry on the LOX sheet behavior. Results were compared with predictions from classical hydrodynamic theories in terms of the film thickness, spreading angle, and velocity distributions. The rapid property variations of oxygen fluid and viscous dissipation play a decisive role in determining the injector characteristics. The present work provides a quantitative basis for optimizing the injector performance.

References

[1] V.G. Bazarov, V. Yang, and P. Puneesh, "Design and dynamics of jet and swirl injectors," in V. Yang., M. Habiballah, J. Hulka, and M. Popp, (Eds.) *Liquid rocket thrust chambers: aspects of modeling, analysis, and design*, Progress in Astronautics and Aeronautics **200**, 19 (2004).

[2] J. Hulka and J.A. Schneider, "Single element injector cold flow testing for STME swirl coaxial injector element design," AIAA Paper No. 1993-2161, 1993.

[3] J. Hulka and J.A. Schneider, "Performance and stability of a booster class LOX/H2 swirl coaxial element injector," AIAA Paper No. 1991-1877, 1991.

[4] J. Hulka and D. Makel, "Liquid oxygen/hydrogen testing of a single swirl coaxial injector element in a windowed combustion chamber," AIAA Paper No. 1993-1954, 1993.

[5] M. Sasaki, H. Sakamoto, M. Takahashi, T. Tomita, and H. Tamura, "Comparative study of recessed and non-recessed swirl coaxial injectors," AIAA Paper No. 1997-2907, 1997.

[6] V.G. Bazarov and V. Yang, "Liquid-propellant rocket engine injector dynamics," J. Propul. Power **14**, 797 (1998).

[7] P.G. Han, J. Seol, S. Hwang, and Y. Yoon, "The spray characteristics of swirl coaxial injectors," AIAA Paper No. 2003-0490, 2003.

[8] S.H. Kim, Y.M. Han, S. Seo, I.Y. Moon, J.K. Kim, and W.S. Seol, "Effects of LOX post recess on the combustion characteristics for Bi-swirl coaxial injector," AIAA Paper No. 2005-4445, 2005.

[9] A.H. Lefebvre, *Atomization and Sprays* (Hemisphere Pub. Co., New York, 1989).

[10] A.R. Jones, "Design optimization of a large pressure-jet atomizer for power plant," Proceeding of the 2nd international conference on liquid atomization and sprays, Madison, Wisconsin, 1982.

[11] T. Marchione, C. Allouis, A. Amoresano, and F. Beretta, "Experimental investigation of a pressure swirl atomizer spray," J. Propul. Power **23**, 1096 (2007).

[12] P.A. Strakey, D.G. Talley, and J.J. Hutt, "Mixing characteristics of coaxial injectors at high gas/liquid momentum ratios," J. Propul. Power **17**, 402 (2001).

[13] D. Kim, J.H. Im, H. Koh, and Y. Yoon, "The effect of ambient gas density on the spray angle and breakup length of a swirling liquid sheet," J. Propul. Power **23**, 603 (2007).

[14] D. Kim, W. Jeong, J. Im, and Y. Yoon, "The characteristics of swirl coaxial injector under varying geometric and environmental conditions," AIAA Paper No. 2004-3521, 2004.

[15] S.K. Ela, "Subscale LOX/Hydrogen testing with a modular chamber and a swirl coaxial injector," AIAA Paper No. 1991-1874, 1991.

[16] H. Tamura, H. Sakamotot, M. Takahashi, M. Sasaki, T. Tomita, and R. Nagao, "LOX/LH2 subscale swirl coaxial injector testing," AIAA Paper No. 1997-2906, 1997.

[17] M. Sasaki, H. Sakamoto, M. Takahashi, T. Tomita, and H. Tamura, "Comparative study of recessed and non-recessed swirl coaxial injectors," AIAA Paper No. 1997-2907, 1997.

[18] B.D. Kim and S.D. Heister, "Numerical modeling of hydrodynamic instability of swirl coaxial injector in a recessed region," AIAA Paper No. 2006-4720, 2006.

[19] B.D. Kim, S.D. Heister, and S.H. Collicott, "Three-dimensional flow simulation in the recessed region of a coaxial injector," J. Propul. Power **21**, 728 (2005).

[20] H. Park and S. D. Heister, "Nonlinear simulation of free surfaces and atomization in pressure swirl atomizers," Phys. Fluid 18, 052103 (2006).

[21] J.V. Canino, J. Tsohas, V. Sankaran, and S.D. Heister, "Dynamic response of coaxial rocket injectors," AIAA Paper No. 2006-4707, 2006.

[22] T. Inamura, H. Tamura, and H. Sakamoto, "Characteristics of liquid film and spray injected from swirl coaxial injector," J. Propul. Power **19**, 632 (2003)

[23] V. Yang, M. Habiballah, J. Hulka, and M. Popp (Eds.), *Liquid rocket thrust chambers: aspects of modeling, analysis, and design*, Progress in Astronautics and Aeronautics **200**, 2004.

[24] H. Meng, G.C. Hsiao, V. Yang, and J.S. Shuen, "Transport and dynamics of liquid oxygen droplets in supercritical hydrogen streams," J. Fluid Mech. **527**, 115 (2005).

[25] N. Zong, H. Meng, S.Y. Hsieh, and V. Yang, "A numerical study of cryogenic fluid injection and mixing at supercritical conditions," Phys. Fluids **16**, 4248 (2004).

[26] N. Zong and V. Yang, "Near-field flow and flame dynamics of LOX/methane shear coaxial injector under supercritical conditions," Proc. Combust. Inst., **31**, 2007.

[27] J.C. Oefelein and V. Yang, "Modeling high-pressure mixing and combustion processes in liquid rocket engines," J. Propul. Power **114**, 843 (1998).

[28] J.C. Oefelein, "Large eddy simulation of turbulent combustion processes in propulsion and power systems," Prog. Aero. Sci. **42**, 2 (2006).

[29] G. Erlebacher, M.Y. Hussaini, C.G. Speziale, and T.A. Zang, "Toward the large eddy simulation of compressible turbulent flows," J. Fluid Mech. **238**, 155 (1992).

[30] U. Piomelli, P. Moin, and J.H. Ferziger, "Model consistency in the large eddy simulation of turbulent channel flows," Phys. Fluids **31**, 1884 (1988).

[31] M.S. Graboski and T.E. Daubert, "A modified Soave equation of state for phase equilibrium calculation, 1. hydrocarbon systems," Ind. Eng. Chem. Proc. Design Dev. **17**, 443 (1978).

[32] V. Yang, "Modeling of supercritical vaporization, mixing, and combustion processes in liquid-fueled propulsion systems," Proc. Combust. Inst. **28**, 925 (2000).

[33] J.F. Ely and H.J. Hanley, "Prediction of transport properties. 1. viscosity of fluids and mixtures," Ind. Eng. Chem. Fundamentals **20**, 323 (1981).

[34] J.F. Ely and H.J. Hanley, "Prediction of transport properties. 2. thermal conductivity of pure fluids and mixtures," Ind. Eng. Chem. Fundamentals **22**, 90 (1983).

[35] S. Takahashi, "Preparation of a generalized chart for diffusion coefficients of gases at high pressures," J. Chem. Eng (Japan) **7**, 417 (1974).

[36] H. Meng and V. Yang, "A unified thermodynamics treatment of general fluid mixtures and its application to a preconditioning scheme," J. Comput. Phys. **189**, 277 (2003).

[37] N. Zong, "Modeling and simulation of cryogenic fluid injection and mixing dynamics under supercritical conditions," Ph.D. Dissertation, Dept. of Mechanical and Nuclear Engineering, Pennsylvania State Univ., University Park, PA, 2005.

[38] S.Y. Hsieh and V. Yang, "A preconditioned flux-differencing scheme for chemically reacting flows at all Mach numbers," Int. J. Comput. Fluid Dyn. **8**, 31 (1997).

[39] M.M. Rai and S. Chakravarthy, "Conservative high-order-accurate finite-difference methods," AIAA paper No. 1993-3380.

[40] G. Comte-Bellot and S. Corrsin, "Simple Eulerian time correlation of full- and narrow-band velocity signals in grid-generated, isotropic turbulence," J. Fluid Mech. **48**, 273 (1971).

[41] R.C. Swanson and E. Turkel, "On central difference and upwind schemes," J. Comput. Phys. **101**, 292 (1992).

[42] V.R. Rubinsky, "Combustion instability in the RD-0110 engine," in V. Yang and W.E. Anderson (Eds.) *Liquid rocket engine combustion instability*, Progress in Astronautics and Aeronautics **169**, 89 (1996).

[43] N. Zong and V. Yang, "Cryogenic fluid jets and mixing layers in transcritical and supercritical environment," Combust. Sci. Tech. **178**, 193 (2006).

[44] T. Poinsot and S. Lele, "Boundary conditions for direct simulation of compressible viscous Flows," J. Comput. Phys. **101**, 104 (1992).

[45] P.K. Kundu and I.M. Cohen, *Fluid Mechanics*, 2nd ed. (San Diego, California, 2001).

[46] S. Wang and V. Yang, "Unsteady flow evolution in swirl injectors, part II: external excitations," Phys. Fluids **17**, 045107, (2005).

[47] V. Yang and W.E. Anderson (Eds.), *Liquid rocket engine combustion instability*, Progress in Astronautics and Aeronautics **169**, (1996).

[48] Y. Huang, S. Wang, and V. Yang, "A systematic analysis of combustion dynamics in a lean-premixed swirl-stabilized combustor," AIAA J. **44**, 724-740 (2006).

[49] K.C. Schadow and E. Gutmark, "Combustion instability related to vortex shedding in dump combustors and their passive control," Prog. Energy Combust. Sci. **18**, 117 (1992).

[50] C.W. Rowley, T. Colonius, and R.M., Murray, "Model reduction for compressible flows using pod and Galerkin projection," Physics D **189**, 115 (2004).

[51] G. Berkooz, P. Holmes, and J. L. Lumley, "The proper orthogonal decomposition in the analysis of turbulent flows," Annu. Rev. Fluid Mech. **25**, 539 (1993).

[52] J. Panda and D.K. McLanghlin, "Experiments on the instabilities of a swirling jet," Phys. Fluids **6**, 263 (1994).

Task 2

Counterflow Diffusion Flames of General Fluids: Oxygen/Hydrogen Mixtures

Summary

A comprchensive framework has been established to study laminar counterflow diffusion flames for general fluids over the entire regime of thermodynamic states. Thc model incorporates a unified treatment of fundamental thermodynamics and transport theories into an existing model, the DMCF code, for treating dctailed chemical kinctic mechanisms and multi-species transport. The resultant scheme can thus be applied to fluids at any state. Both subcritical and supercritical conditions are considered. As a specific example, diluted and undiluted H_2/O_2 flames are investigated at pressures of 1-25 MPa and oxygen inlet temperatures of 100 and 300 K. The effects of prcssure p and strain rate a on the heat release rate $\dot{q}_s$, extinction limit, and flame structure arc cxaminccl. In addition, the impact of cross-diffusion terms, such as the Soret and Dufour effects, on the flame bchavior is asscssed. Results indicate that the flame thickness δ_f and heat release rate correlate well with the square root of the pressure multiplied by the strain rate as $\delta_f \sim 1/\sqrt{pa}$ and $\dot{q}_s \sim \sqrt{pa}$. The extinction limit strain rate exhibits a quasi-linear dependence with p. Significant real-fluid effects take place in the transcritical regimes, as evidenced by the steep property variations in the local flowfield. However, their net influencc on the flame properties, appears to be limited due to the ideal-gas behavior of fluids in the high-temperature zone.

2.1 Introduction

Laminar counterflow diffusion flames provide much useful information about the basic properties of non-premixed combustion. Scveral numcrical codes incorporating dctailed chemical kinctic mechanisms and multi-species transport, such as the Detailed Modeling of Counterflow Flame (DMCF) code (Darabiha *et al.* 1988 ; Darabiha 1992), have been developed to study flame behavior under various flow conditions. For instance, thc effects of strain rate on burning behavior and flame stability were examined systematically for a variety of fuel/oxidizer combinations (Im *et al.* 1995). Results have been applied as a submodel in the modeling of turbulent diffusion flames in the flamelet regime, in which the flamc is locally assumed to bear a laminar structure. Thus, a thorough understanding of strained laminar flames is a prerequisite to achieving improved knowledge of morc complex systems.

The majority of existing studies on counterflow diffusion flames have been carried out at low and moderate pressures. The effects of supercritical conditions that often occur in high-pressure combustion devices (Yang 2000) have not been carefully explored. Most of the previous studies have dealt with systcms involving either a gaseous or liquid-spray fuel against an air flow. Thc influence of strain rate, inlet temperature, and radiative heat losses on flame structures was numerically investigated and benchmarked against experimental data. Sung *et al.* (1995) have shown both

experimentally and numerically that the flame thickness varies inversely with the square root of the strain rate for a methane/oxygen/nitrogen diffusion flame at one atmosphere. Brown *et al.* (1997) studied the effect of hydrogen dilution by nitrogen for diffusion flames involving (an 80/20 H_2/N_2 mixture) and air. Balakrishnan *et al.* (1995) examined the extinction and ignition limits for diluted and undiluted H_2/O_2 diffusion flames in the pressure range of 0.25-10 bar using both full and reduced chemical kinetic schemes. The critical strain rate at extinction was found to increase rapidly with increasing pressure. Williams (2001) examined the effects of transport on non-premixed flame structures and extinction characteristics, and observed that the strain rate corresponding to the extinction limit is sensitive to molecular transport. A related study was later carried out numerically by Ben Dakhlia *et al.* (2002) on diffusion flames involving n-heptane/O_2/N_2. The Soret effect was found to be dependent on the diluent considered (i.e., nitrogen or helium), and appeared in the flame structure and fuel-vapor diffusion boundary layer. Juniper *et al.* (2003) considered the counterflow diffusion flames formed by gaseous hydrogen impinging on a pool of liquid oxygen and gaseous hydrogen at 1 and 2 bar using a perfect-gas law. The oxygen temperature was set to 90 K, whereas the hydrogen temperature varied from 20 to 310 K. Results indicated that the heat-release rate per unit surface area is proportional to the square root of the pressure multiplied by the strain rate. It was also found that the extinction limit strain rate increases with pressure, a phenomenon consistent with experimental results for n-heptane/air flames (Niioka *et al*, 1991).

The present work deals with the effects of pressure on laminar counterflow diffusion flames. Emphasis is placed on the supercritical conditions typically encountered in high-pressure combustion devices like liquid-propellant rocket, diesel and gas-turbine engines. A notable example is provided by cryogenic thrust chambers like that of the Vulcain 2 engine (Candel *et al.* 2006) in which liquid oxygen (LOX) is injected at a subcritical temperature of 80 K into a high-pressure environment of 11.5 MPa. These conditions are to be compared with the thermodynamic critical temperature and pressure of oxygen which are 154.8 K and 5.04 MPa, respectively. Under these conditions, the injected LOX heats up rapidly and its interface with the surrounding gases prevails over a finite distance from the injection plane. The dense core disappears progressively as mass is transferred from this region to the jet surroundings. Several experimental (Mayer *et al*, 1998; Candel *et al.* 2006) and numerical (Oefelein and Yang, 1998; Oefelein 2006; Zong and Yang 2007) studies have been carried out to characterize the supercritical flame dynamics of shear co-axial injectors for hydrogen and methane fuels. Detailed flow development and flame stabilization and spreading mechanisms were investigated in the near field of the injector exit.

Significant real-gas effects featuring steep property variations take place when the fluid crosses the thermodynamic transcritical regime (Yang 2000; Zong *et al.* 2004). In contrast, the fluid behaves like an ideal gas in the high-temperature reaction and product zones. Palle *et al.* (2005) conducted numerical simulations for unsteady one-dimensional laminar diffusion flames at a pressure of 10 MPa for N_2/O_2, $N_2/C_{12}H_{26}$ and H_2/O_2 mixtures. Three different models of a one-step reaction in the form $A+r_1C\rightarrow$ P were considered and cross-diffusion terms were included. The Soret effect was found to be non-negligible for species with different molecular weights, especially for the

$H_2+(1/2)O_2 \rightarrow H_2O$ reaction. The Dufour effect was insignificant for all cases. Sohn *et al.* (1998) studied numerically the structures and acoustic responses of undiluted H_2/O_2 diffusion flames at pressures up to 10 MPa. Both detailed and reduced chemical kinetic schemes were employed. The calculated strain rate at the extinction limit showed a quasi-linear pressure dependence. This result, obtained with a 4-step reaction mechanism, remains to be checked with a more complete kinetic scheme.

The purpose of the present study is to develop a comprehensive numerical model capable of treating counterflow diffusion flames over the entire range of fluid thermodynamic states. Both subcritical and supercritical conditions are examined. Such a general-fluid approach will not only allow us to explore the flame behavior under various fluid states, but will also serve as a fundamental tool for establishing flame submodels for treating turbulent combustion over a wide range of pressures. To this end, a detailed combustion modeling tool (DMCF) is first extended by implementing general-fluid thermodynamics theories (Meng and Yang, 2003), such that the fluid thermodynamics can be formulated in a unified manner. A general balance of energy is then derived, and thermophysical properties are evaluated with a self-consistent scheme valid for general fluids (Yang 2000). As a specific example, this analysis is employed to investigate H_2/O_2 and H_2/air diffusion flames in both subcritical and supercritical environments. The influences of pressure and strain rate on the flame structure and behavior, as well as the heat release rate, are examined systematically. In addition, the Soret and Dufour effects are studied.

2.2 Theoretical Formulation

The physical model considered herein is an axisymmetric laminar diffusion flame stabilized near the stagnation plane of two opposing streams, as shown schematically in Figure 1. The theoretical basis for treating such a flame configuration is well established for perfect gases (Smooke *et al.* 1986; Darabiha 1992; Ern and Giovangigli 1999).

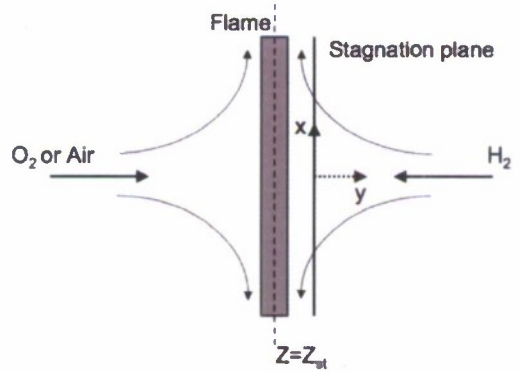

Fig. 1. Schematic diagram of a counterflow diffusion flame.

A constant strain rate, a, defined as the radial gradient of the radial velocity, $\partial u/\partial x$, at the fuel boundary, is assumed. Following the approach of Meng and Yang (2003), the analysis is extended by incorporating general-fluid thermodynamics theories and property

evaluation schemes, so that that the flame behavior over the entire regime of fluid states can be formulated in a unified manner.

2.2.1 Governing Equations

The balance equations of mass, momentum, species mass fractions, and enthalpy for a counterflow flame with a fixed strain rate can be expressed in the following forms.

- Mass

$$\frac{\partial \rho}{\partial t} = -\frac{\partial \rho v}{\partial y} - 2\rho a u^{+} \tag{1}$$

- Radial momentum

$$\rho \frac{\partial u^{+}}{\partial t} = \frac{\partial}{\partial y}\left(\mu \frac{\partial u^{+}}{\partial y}\right) - \rho v \frac{\partial u^{+}}{\partial y} + a\left(\rho_{+\infty} - \rho u^{+2}\right) \tag{2}$$

- Species

$$\rho \frac{\partial Y_k}{\partial t} = -\rho v \frac{\partial Y_k}{\partial y} - \frac{\partial}{\partial y}\left(\rho Y_k V_k\right) + \dot{\omega}_k \qquad k = 1, \ldots, N_s \tag{3}$$

- Enthalpy

$$\rho C_p \frac{DT}{Dt} = \frac{\partial}{\partial y}\left(\lambda \frac{\partial T}{\partial y}\right) - \left(\rho \sum_{k=1}^{N_s} Y_k V_{k,i}\right) \frac{\partial \bar{h}_k}{\partial y} - \sum_{k=1}^{N_s} \bar{h}_k \dot{\omega}_k \tag{4}$$

where ρ is the density, Y_k, W_k, and $\dot{\omega}_k$ the mass fraction, molecular weight, and reaction rate of species k, respectively, $u^{+} = u/ax$ the reduced radial velocity, v the axial velocity, and μ the viscosity. The partial-mass enthalpy of species k, $\bar{h}_k$, is introduced to account for the interactions between molecules of different components in a general-fluid mixture (Meng and Yang 2003). It is defined by the total mass of the mixture, m, and the partial masses of all constituent components, m_k,

$$\bar{h}_k = \left(\frac{\partial mh}{\partial m_k}\right)_{T,p,m_{k \neq l}} \tag{5}$$

The specific enthalpy of the mixture, h, thus becomes

$$h = \sum_{k=1}^{N_s} Y_k \bar{h}_k \tag{6}$$

2.2.2 Thermodynamic Properties and Equation of State (EOS)

Thermodynamic properties, such as internal energy, enthalpy, and constant-pressure specific heat are evaluated based on fundamental thermodynamics theories. Each property can be conveniently expressed as the sum of the ideal-gas counterpart at

the same temperature and a departure function that accounts for the dense-fluid correction. Thus,

$$e(T,\rho) = e_0(T) + \int_{\rho_0}^{\rho} \left[\frac{p}{\rho^2} - \frac{T}{\rho^2}\left(\frac{\partial p}{\partial T}\right)_\rho \right]_T d\rho \tag{7}$$

$$h(T,p) = h_0(T) + \int_{P_0}^{P} \left[\frac{1}{\rho} + \frac{T}{\rho^2}\left(\frac{\partial \rho}{\partial T}\right)_P \right]_T dp \tag{8}$$

$$C_P(T,\rho) = C_{V0}(T) - \int_{\rho_0}^{\rho} \left[\frac{T}{\rho^2}\left(\frac{\partial^2 p}{\partial T^2}\right)_\rho \right]_T d\rho + \frac{T}{\rho^2}\left(\frac{\partial p}{\partial T}\right)_\rho^2 \Bigg/ \left(\frac{\partial p}{\partial \rho}\right)_T \tag{9}$$

where the subscript 0 refers to the ideal state at low pressure. The departure functions on the right-hand sides of equations (7)-(9) are determined using an appropriate equation of state. In the present study, a modified Soave-Redlich-Kwong (SRK) equation of state (Soave 1972; Graboski and Daubert 1978) is chosen due to its wide range of validity in modeling the fluid p–V–T behavior and ease of implementation. It takes the following form,

$$p = \frac{\rho RT}{(W - b\rho)} - \frac{a\alpha}{W}\frac{\rho^2}{(W + b\rho)} \tag{10}$$

where R is the universal gas constant, and W the molecular weight of the fluid mixture. The two parameters, a and b, taking into account the effects of attractive and repulsive forces among molecules, respectively, are calculated with the following mixing rules,

$$a\alpha = \sum_{i=1}^{N_s}\sum_{j=1}^{N_s} X_i X_j \alpha_{ij} a_{ij} \tag{11}$$

$$\alpha_{ij} a_{ij} = \sum_{i=1}^{N_s}\sum_{j=1}^{N_s} \sqrt{\alpha_i \alpha_j a_i a_j}\left(1 - \kappa_{ij}\right) \tag{12}$$

$$b = \sum_{i=1}^{N_s} X_i b_i \tag{13}$$

where X_k is the mole fraction of species k and κ_{ij} the binary interaction coefficient (Graboski and Daubert 1978). The constants a_i and b_i are determined from the following universal relationships,

$$a_i = 0.42747 \frac{R^2 T_{c_k}^2}{p_{c_k}} \tag{14}$$

$$b_i = 0.08664 \frac{RT_{c_k}}{p_{c_k}} \tag{15}$$

where T_{c_k} and p_{c_k} represent the critical temperature and pressure of specics k, respectively. The third parameter, α_i, is given as,

$$\alpha_i = \left[1 + S_i\left(1 - \sqrt{\frac{T}{T_{c_k}}}\right)\right]^2 \tag{16}$$

where S_i is a function of the accentric factor, ω_i,

$$S_i = 0.48508 + 1.5517\omega_i - 0.15613\omega_i^2 \tag{17}$$

2.2.3 Transport Properties

Accurate evaluation of transport properties is crucial for the study of high-pressure flow and flame dynamics. To account for the continuous variation of fluid properties in a supercritical environment one cannot use classical techniques which deal individually with liquids or gases . In the present study, both the mixture viscosity, μ, and thermal conductivity, λ, are determined by the method proposed by Chung *et al.* (1988), established based on the Chapman-Enskog theory with a dense-fluid correction. The calculated properties agree well with the NIST experimental data for both the gas and liquid phases (Congiunti *et al.* 2003).

Estimation of the binary mass diffusivity for a fluid mixture at high pressures is a challenging task, due to the lack of a formal theory or even a theoretically based correlation. Takahashi (1974) suggested a simple scheme for predicting the binary mass diffusivity of a dense fluid by means of a corresponding-state principle. The method, which was established based on curve fits of experimental data of various species over a wide range of pressure and temperature, provides a relatively accurate estimation of the diffusion coefficient of a fluid mixture when the tempcrature is greater than the critical value. Model uncertainties, however, may arise when the reduced temperature of the mixture is smaller than unity because most of the data employed to validate the correlation is located in the ncar- or super-critical temperature regime.

2.2.4 Boundary Conditions and Numerical Method

For a given fuel/oxidizer combination and flow condition, the flame structure is defined by the following boundary conditions:

$$T_{y\to-\infty} = T_{-\infty}, \quad Y_{k,y\to-\infty} = Y_k^{-\infty}, \; u^+_{y\to-\infty} = \left(\frac{\rho_{+\infty}}{\rho_{-\infty}}\right)^{1/2} \tag{18}$$

$$T_{y\to+\infty} = T_{+\infty}, \quad Y_{k,y\to+\infty} = Y_k^{+\infty}, \; u^+_{y\to+\infty} = 1 \tag{19}$$

along with an additional relation $v_{[y=0]} = 0$.

The overall system of equations (1-4) can be conveniently combined into the following form

$$\frac{\partial \psi}{\partial t} + F(\psi) = 0 \tag{20}$$

where ψ is the solution vector and F a differential operator. At a steady state, i.e., $F(\psi) = 0$, equation (20) and the associated boundary conditions can be solved by means of a combination of time marching and Newton iteration techniques (Darabiha 1992). A global adaptive grid is employed to refine the spatial resolution in regions with steep gradients.

2.3 Discussion of Results

The theoretical and numerical framework outlined above has been employed to study the H_2/O_2 counterflow diffusion flames under a variety of flow conditions. The work consists of two parts. First, the flame behavior over a wide range of subcritical pressures is studied using several different detailed chemical kinetics schemes. The impact of the Soret and Dufour effects is also examined. Second, the flame behavior under transcritical and supercritical conditions is explored. Emphasis is placed on the effects of pressure and strain rate on the flame properties and heat release distributions.

2.3.1 Subcritical Pressures

The H_2/O_2 reaction mechanism employed in the present study was developed by Li *et al.* (2004). The scheme is extended from the work of Muller *et al.* (1998) and contains 8 reacting species (i.e., H_2, O_2, H, O, OH, HO_2, H_2O, and H_2O_2) and 19 reversible reactions. Validated for a wide range of experimental conditions ($T \in$ [298-3000 K], $p \in$ [0.25-87 bar]) for laminar premixed flames in shock tubes and flow reactors, the mechanism has been implemented with success in simulating non-premixed H_2/air counterflow flames (Fotache *et al.* 1998 ; Briones and Aggarwal 2005). Figure 2 shows the calculated distributions of the temperature and species mass fractions at the standard condition (i.e., $T_{H_2} = T_{O_2} = 300$ K, $p = 1$ bar). The mixture fraction Z at the flame front is defined (Poinsot and Veynante 2005) as

$$Z = \frac{sY_{H_2} - Y_{O_2} + Y_{O_2}^0}{sY_{H_2}^0 + Y_{O_2}^0} \text{ with } s = 8 \text{ and } Y_{H_2}^0 = Y_{O_2}^0 = 1 \tag{21}$$

Two different software tools are employed herein.

(i) Designated as DMCF both thermodynamic and transport properties are determined from the CHEMKIN and TRANSPORT libraries for ideal gases (Kee *et al.* 1986).

(ii) Designated as DMCF-PRF (Partial Real-Fluid); thermodynamic properties are determined based on the SRK EOS (Meng and Yang 2003), whereas transport properties are estimated using the TRANSPORT library (Kee et al. 1986).

The difference between the flame structures as calculated using the two approaches is negligible, as evidenced in Figure 2. The real fluid thermodynamics implemented in the present study is validated in the limit of ideal gas. The flame thickness δ_f, defined as the

full width at half maximum, is 18 mm for a strain rate of 20 s^{-1}. The temperature reaches its maximum value of 3050 K, which is close to the adiabatic flame temperature of T_{ad}= 3080 K, for the stoichiometric H_2/O_2 mixture.

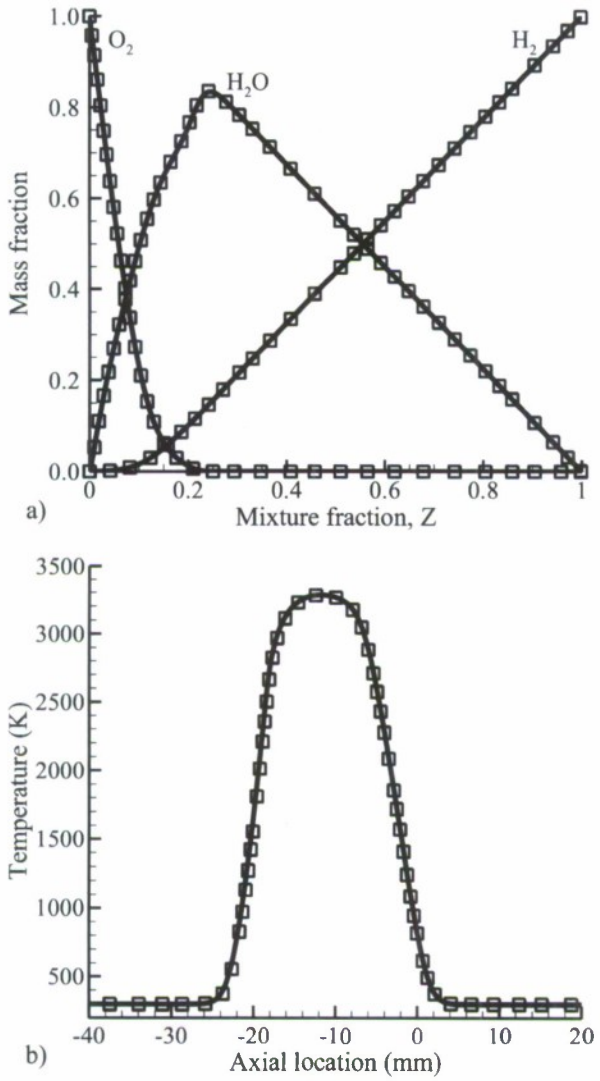

Fig. 2. Mass fractions and temperature at p=1 bar, T_{O2}=T_{H2}=300 K and a=20 s^{-1}: Casc (i) is based on the ideal-gas assumption (Darabiha 1992) (□□□); case (ii) incorporates general-fluid thermodynamics theories and the SRK EOS (—).

Two other different detailed chemical kinetics schcmes werc also tested for simulating the flame structure : the mechanism of Miller *et al.* (1982) and the sub-mechanism of Katta and Roquemore (1998). Almost identical results were obtained, except that thc latter predicts a flame temperature near 4400 K. Accordingly, only the mcchanism of Li *et al.* (2004) is used in what follows.

The Soret and Dufour effeets are examined. With the Hirschfelder-Curtiss approximation for thermal diffusion, (i.e. the Soret effect), the mass diffusion velocity can be expressed in the following general form (Kee *et al.* 1986):

$$V_k = V_k^* + W_k^* + V_c = -D_k^* \frac{1}{X_k}\frac{\mathrm{d}X_k}{\mathrm{d}y} - \frac{D_k^*\theta_k^*}{X_k}\frac{1}{T}\frac{\mathrm{d}T}{\mathrm{d}y} + V_c \tag{22}$$

where θ_k^* is the thermal-diffusion ratio. The correction velocity defined below can be evaluated by the TRANSPORT package (Kee *et al.* 1986).

$$V_c = -\sum_{k=1}^{N_s} Y_k \left(V_k^* + W_k^*\right) \tag{23}$$

This approximation has been validated by Daguse *et al.* (1996) against a complete kinetic theory for a counterflow $H_2/O_2/N_2$ diffusion flame at atmospheric pressure. Results show that the two approaches are in good agreement. The calculated species and temperature profiles differ by 1% in location and the flame front is slightly displaced. The present method does not introduce significant error.

Figures 3(a) and 3(b) show the temperature distributions of the H_2/air and H_2/O_2 flames with strain rates of a = 2000 and 8000 s^{-1}, respectively. The pressure is set to 1 bar, and the incoming flow temperature is 300 K for both fuel and oxidizer. Compared to the H_2/air system, the larger quantity of burnt fuel in the H_2/O_2 system produces a thicker flame. The maximum temperature (T_{max}) is around 3050 K for the H_2/O_2 system and 2250 K for the H_2/air system. The latter exhibits a steeper gradient near the temperature maximum. At a higher strain rate, the flame thickness δ_f is reduced and is found to vary with the inverse square root of the strain rate (i.e. with $1/\sqrt{a}$) (Sung *et al.* 1995) for both cases. The maximum temperature T_{max} decreases slightly to 3030 and 1950 K for the H_2/O_2 and the H_2/air cases, respectively. The impact of the Soret effect is shown by the solid symbols in Figure 3. As a result of thermal diffusion, light molecules are driven towards hot gases and heavy molecules move in the opposite direction, thereby leading to a moderate change in the flame structure. Since hydrogen rapidly reacts with other species, thermal diffusion plays a slightly more important role on the oxidizer side, especially near the flame center where light species are present. The inclusion of thermal diffusion thus results in a slight decrease in the flame thickness and temperature on the oxidizer side. The effect becomes more obvious for H_2/O_2 systems due to the steeper temperature gradient in the flame zone.

Figures 4a and 4b show the temperature profiles for different pressures at a fixed strain rate of 2000 s^{-1} for H_2/air and H_2/O_2 flames, respectively. For both systems, the maximum flame temperature increases with increasing pressure, but the flame thickness exhibits an opposite trend. This can be explained through an asymptotic analysis (Juniper *et al.* 2003). The heat release per unit surface area is proportional to $\sqrt{pa}$, but the thermal conductivity remains basically pressure-independent. As a consequence, the maximum temperature increases with pressure. The reduction in flame thickness with pressure was also found by Law (2006), who suggested the use of the pressure-weighted

strain rate pa in correlating the pressure effects. The flame thickness is thus proportional to $1/\sqrt{pa}$ (instead of $1/\sqrt{a}$), as shown in the Figure 5.

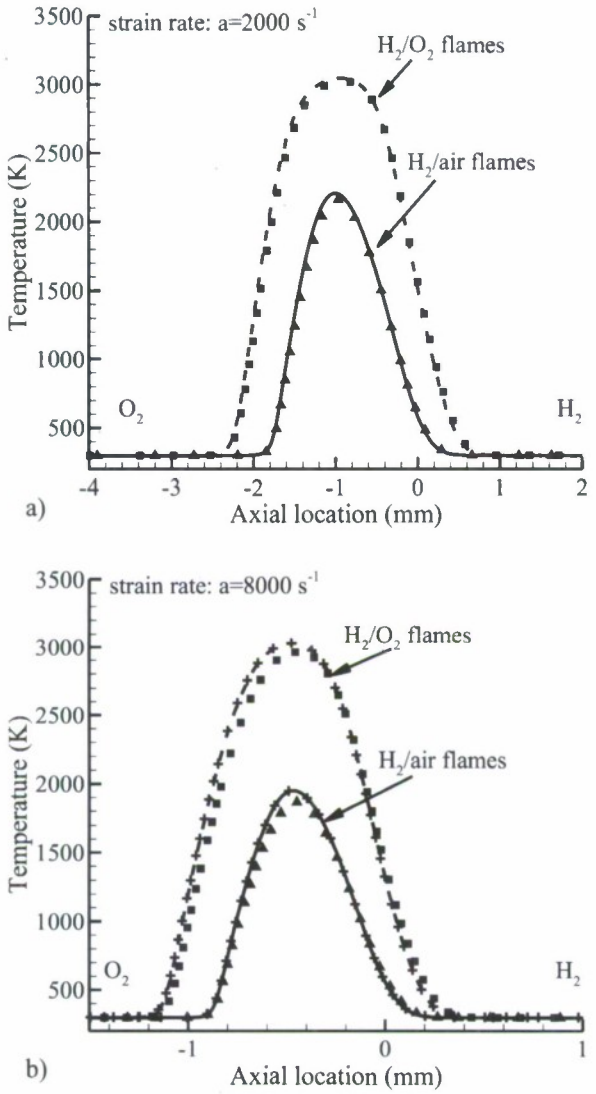

Fig. 3. Impact of the Soret and Dufour effects on H_2/air and H_2/O_2 counterflow diffusion flames at p=1 bar: lines lines (—, —) correspond to diffusion velocity based on mole gradient, (■,▲) include the Soret effect, and (+) represents the Dufour effect.

The impact of the Dufour effect, which accounts for the thermal diffusion induced by a concentration gradient (q_D), is examined by incorporating the following term into the enthalpy equation (4).

$$q_D = -p\sum_{k=1}^{N_s}\left(D_k^{\bullet}\theta_k^{\bullet}\frac{\mathrm{d}X_k}{\mathrm{d}y}\right) \tag{24}$$

The influence on the flame structure appears to be negligible, as evidenced in Figures 3b and 4b. The same conclusion was reached by Ern and Giovangigli (1998) in their study on the H_2/air and CH_4/air flames.

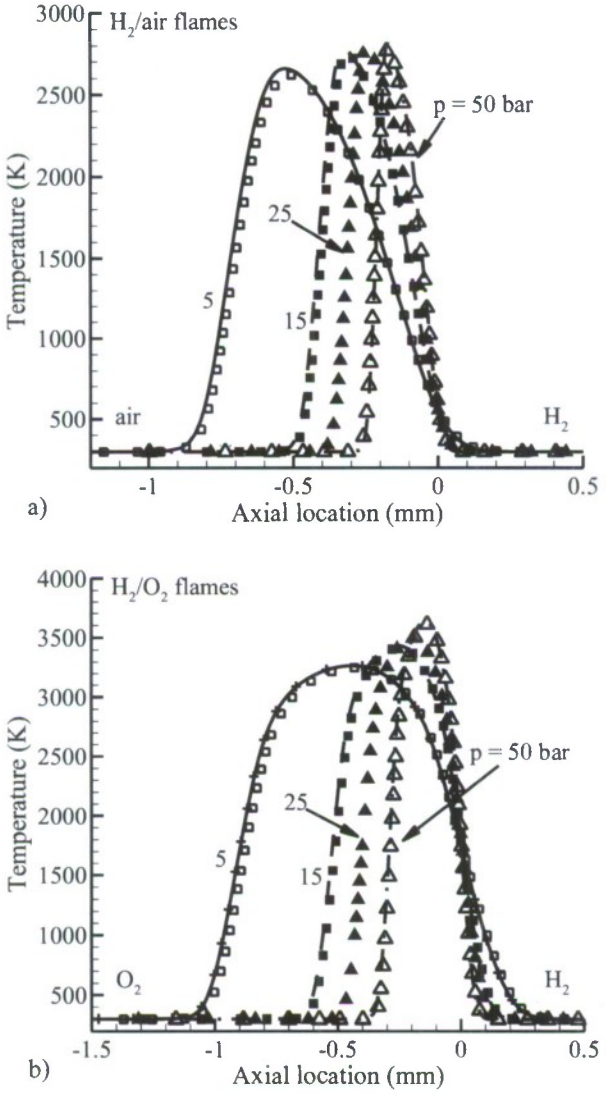

Fig. 4. Impact of the Soret and Dufour effects on H_2/air and H_2/O_2 counterflow diffusion flames for different subcritical pressures at a=2000 s^{-1}: lines (—, −− and · · ·) correspond to diffusion velocity based on mole gradient, (■,▲,□ and △) include the Soret effect, and (+) represents the Dufour effect on H_2/O_2 flame (p=5 bar).

2.3.2 Supercritical Pressures

The flame behavior in the supercritical-pressure regime of oxygen (p > 5.04 MPa) was investigated by means of the general framework described in Section 2. All the thermodynamic and transport properties are calculated using the real-fluid approach along with the SRK equation of state. The overall treatment is designated as DMCF-RF

(full real-fluid). The chemical reaction mechanism is based on the detailed scheme proposed by Li *et al.* (2004). Table 1 gives the critical pressure and temperature of the species included in the reaction scheme. All the species except hydrogen have critical pressure and temperature larger than those of oxygen, and thus may undergo thermodynamic phase transition to the liquid phase in regions situated far from the flame zone, depending on the local flow conditions. This phenomenon, however, is not taken into account in the present analysis, because only small amounts of these species are present in the low temperature regions where fluid condensation may occur.

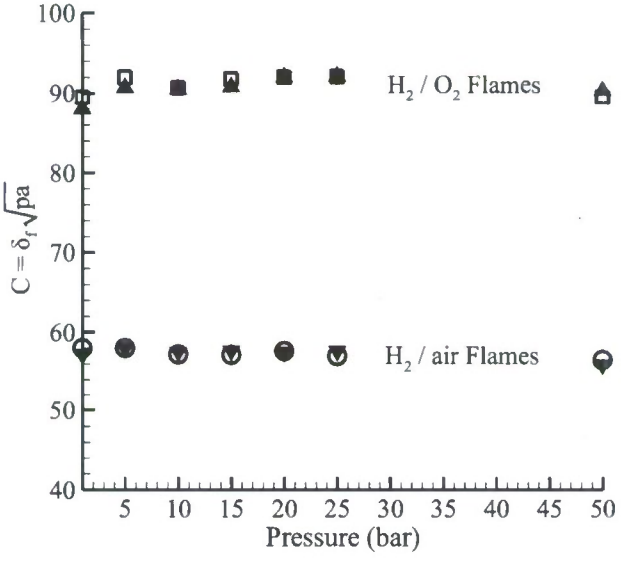

Fig. 5. Flame thickness, δf, as a function for pressure for H_2/air and H_2/O_2 counterflow diffusion flames at two different strain rates: (▲,▼) for a=2000 s^{-1} and (○,□) for a=8000 s^{-1}.

Table 1 Critical pressure Pc and temperature Tc of species involved in the H2/O2 chemical reaction mechanism.

	H_2	O_2	H	O	OH	HO_2	H_2O	H_2O_2
P_c (bar)	13	50.4	88.2	76	85.4	82.8	221.2	93.5
T_c (K)	33.2	154.6	404.3	367.4	443.7	487.3	647.3	544.3

Figures 6a and 6b show the mass fractions of major and minor species at 50 and 100 bar. The inlet temperature is fixed at 300 K for both hydrogen and oxygen, and the strain rate is set to 2000 s^{-1}. As the pressure increases from 50 to 100 bar, the water vapor mass fraction remains the same in the flame zone, whereas the flame thickness varies inversely with $\sqrt{p}$. Since the diffusive transport (ρD) is pressure insensitive, the intensity of chemical reactions becomes the dominant parameter of the combustion

species mass fractions toward the hydrogen side. The situation is, however, quite different for minor species. At a higher pressure, the H mass fraction decreases, and the relatively inactive HO_2 species increases through the $H + O_2 + M \rightarrow HO_2 + M$ reaction pathway. A small amount of H_2O_2 is produced through the HO_2-H_2O_2 chain mechanism. Figure 7 shows the results for the oxygen inlet temperature of 100 K, with all the other conditions identical to those in Figure 6. Only slight changes appear on the oxygen side, where a greater quantity of energy is needed to heat up and then react with oxygen. As a consequence, all species profiles are shifted toward the hydrogen side. The real-fluid effects play a role through species transport, inducing a small increase in the maximum of the intermediate species as compared with those shown in Figure 6.

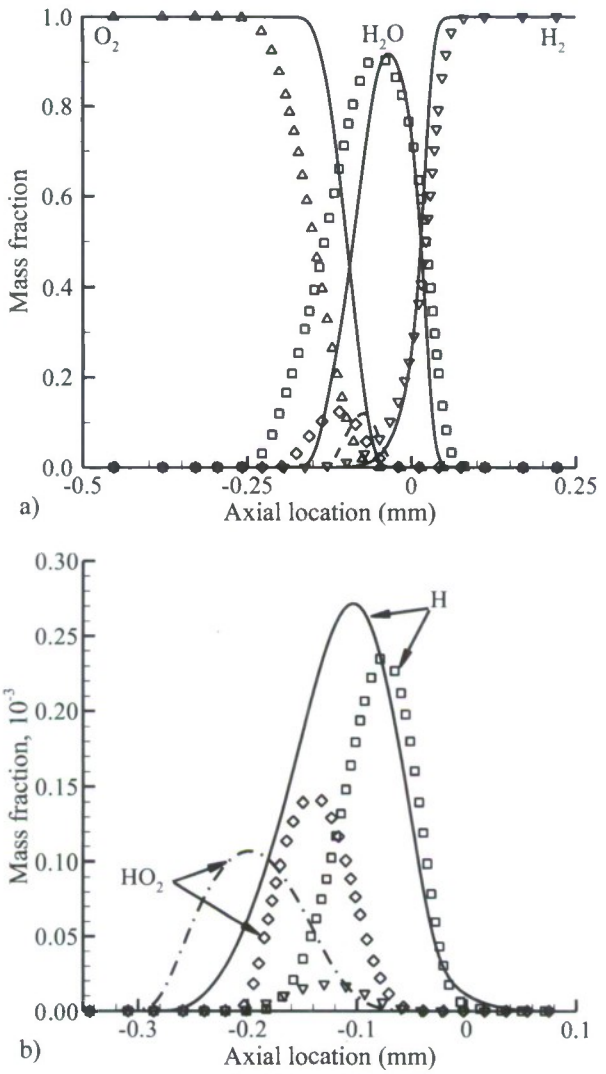

Fig. 6. Distributions of mass fractions of H_2/O_2 flames at 50 bar (lines) and 100 bar (symbols). T_{H2}= T_{O2}=300 K and a=2000 s^{-1} ; (a) Major species profiles: O_2 (—·—,△), H_2 (···,▽), H_2O (—,■) and OH (—,◆); (b) Radicals profiles: H (—,□),HO_2 (—·—,◇) and H_2O_2 (···,▽).

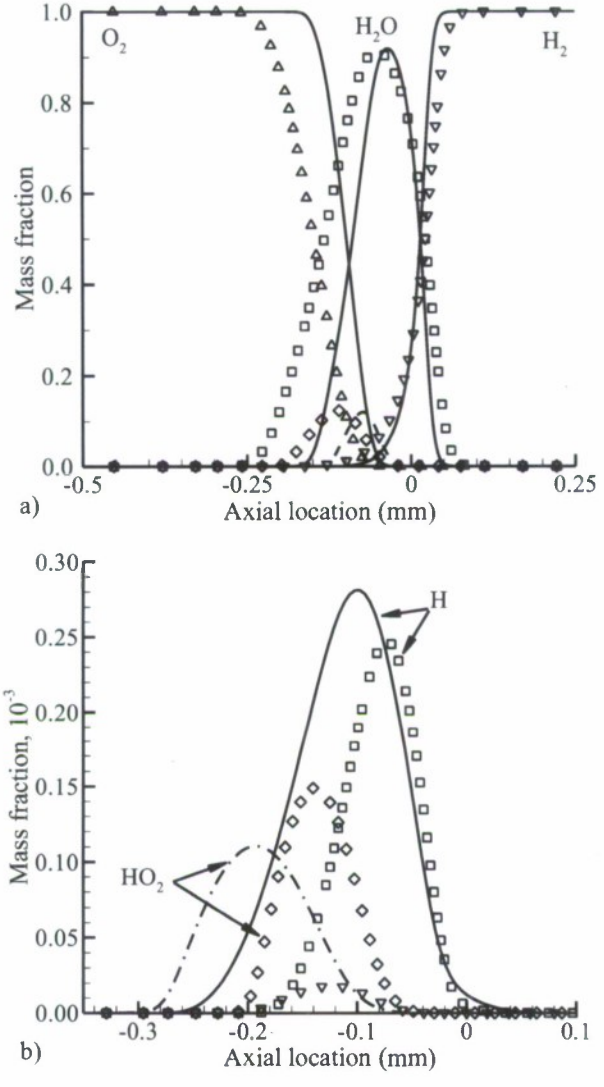

Fig. 7. Distributions of mass fractions of H_2/O_2 flames at 50 bar (lines) and 100 bar (symbols). T_{H2}=300 K, T_{O2}=100 K and a=2000 s^{-1}; (a) Major species profiles: O_2 (—·—,△), H_2 (···,▽), H_2O (—,■) and OH (—,◆); (b) Radicals profiles: H (—,□),HO_2 (—·—,◇) and H_2O_2 (···,▽).

The distributions of the fluid density and thermophysical properties, including the compressibility factor (Z_c), the Schmidt and Prandtl numbers ($Sc(k) = \mu/(\rho D_k^*)$ and $Pr = (\mu C_p)/\lambda$, respectively), and the specific heat, were obtained to explore their effects on the flame structure. Figures 8 and 9 present the results for oxygen inlet temperatures of T_{O_2} = 300 and 100 K, respectively. The hydrogen temperature is fixed at 300 K, and the strain rate at 2000 s^{-1}. The condition of 50 bar is close to the critical pressure of oxygen and was chosen to permit an investigation of the effects on flame behavior of rapid property variations in the transcritical regime. In the case shown in Figure 8, both the oxygen and hydrogen temperatures are supercritical. The compressibility factor is around

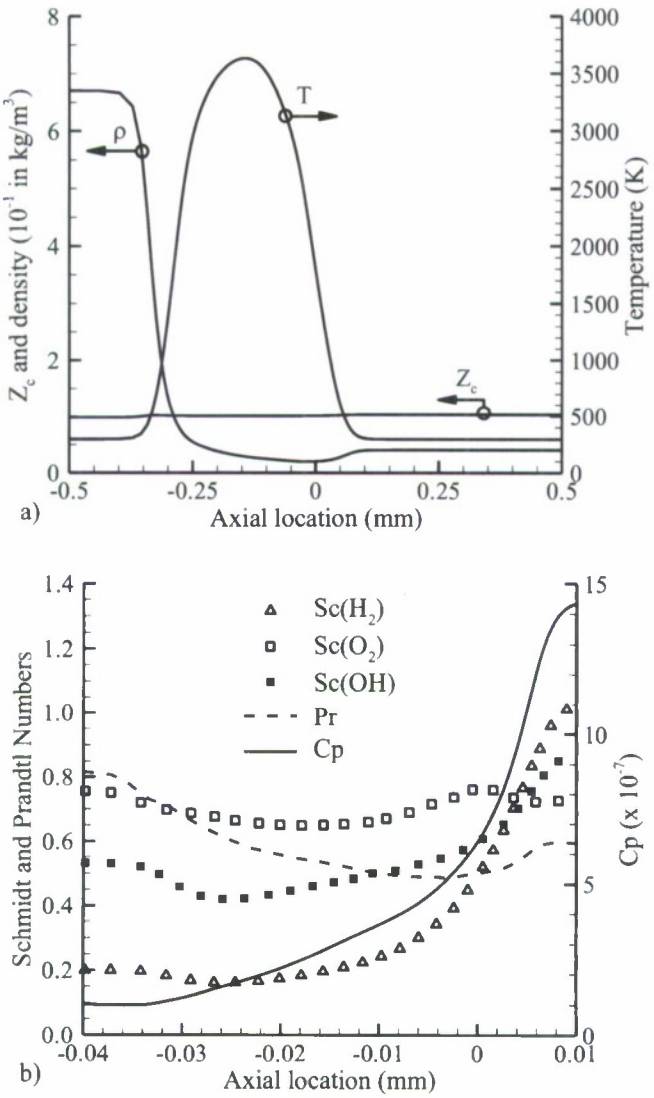

Fig. 8. Distribution of thermodynamic and transport properties for H_2/O_2 flame. T_{O2}=300 K, T_{H2}=300 K, a=2000 s^{-1} and p=50 bar.

unity over the entire domain, whereas the density changes from 67 kg/m^3 on the oxygen side to 4 kg/m^3 on the hydrogen side, with a minimum of 2 kg/m^3 in the flame zone. The transport properties of *Pr* and *Sc(k)* vary moderately around their mean values in the flame zone. In Figure 9, oxygen is injected at a subcritical temperature of 100 K, but hydrogen remains at a supercritical state. The fluid compressibility factor undergoes a rapid variation from $Z_c \approx 0.18$ to 1.0 on the oxygen side when the local temperature increases across the critical point. The same phenomenon is observed for other thermodynamic and transport properties due to the abnormal changes near the critical point of oxygen. In spite of such drastic changes of fluid properties in the low-temperature region on the oxygen side, the oxygen heats up rapidly and behaves like a

perfeet gas before entering the flame zone. The flame thickness as measured by thetemperature profile thus beeomes almost identieal in Figures 8 and 9 for T_{O_2} =100 and 300 K, respeetively. The influencc of the oxygen inlet temperature and assoeiated real-fluid effect appear to be limited in determining the flame behavior. The transport parameters (ρD or λ/C_p) are basieally independent of pressure over most of the flowfield and have values elose to their ideal-gas eounterparts.

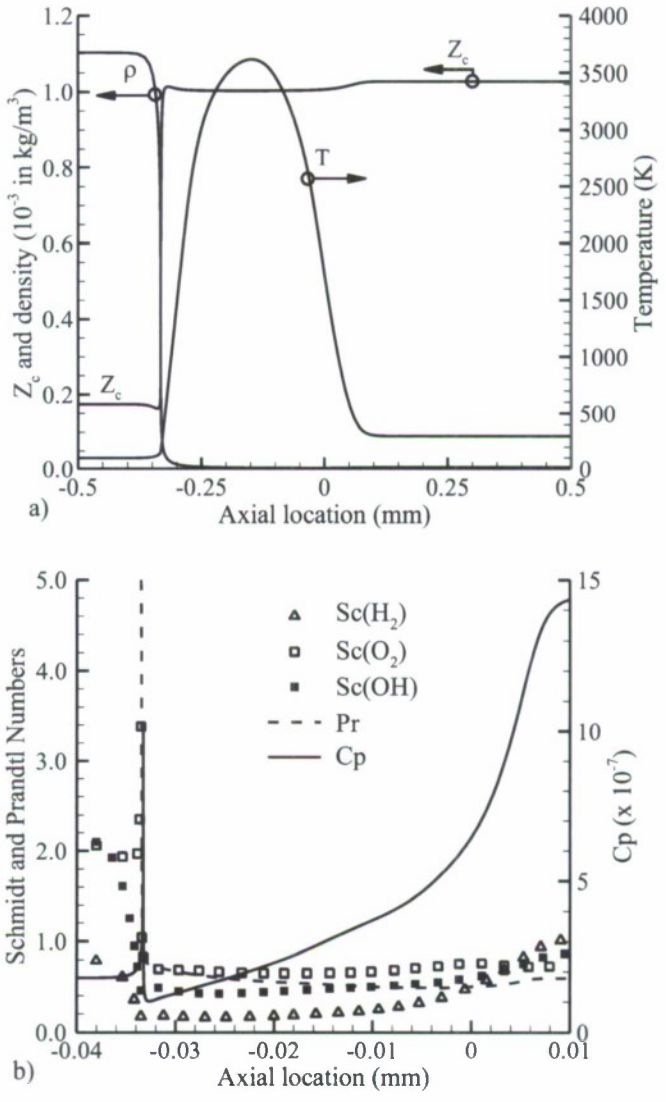

Fig. 9. Distributions of thermodynamie and transport properties for H_2/O_2 flame. T_{O2}=100 K, T_{H2}=300 K, a=2000 s^{-1} and p=50 bar.

Figure 10 shows the temperature distributions for four differcnt pressures in the range of 25-200 bar. The strain rate is fixed at 2000 s^{-1}, and two different oxygen inlet tcmperaturcs of T_{O_2} = 300 and 100 K are considered. At a given strain rate, an inerease in

pressure leads to a thinner flame with a higher flame temperature. A decrease in the oxygen inlet temperature from 300 to 100 K causes only a slight decrease of 20 K in the flame temperature. The ensuing enlargement of the flame is also quite moderate. This behavior can be further explored by considering the heat release rate per unit area, $\dot{q}_s$.

$$\dot{q}_s = \int \sum_{k=1}^{N_s} \bar{h}_k W_k \dot{\omega}_k \tag{25}$$

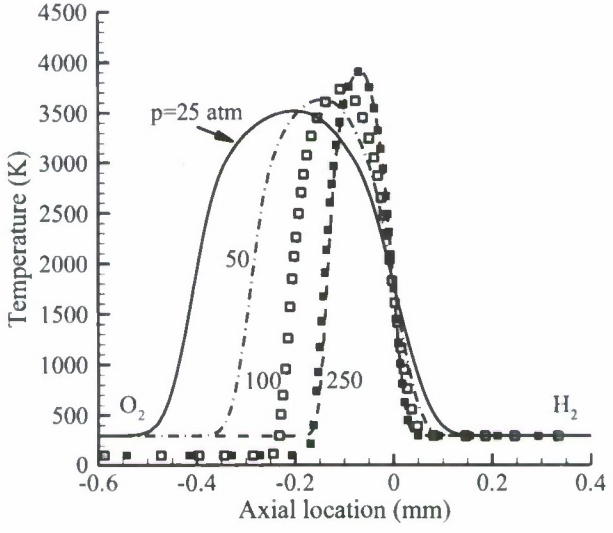

Fig. 10. Temperature profiles for H_2/O_2 counterflow diffusion flames at different pressures. a= 2000 s^{-1}. T_{H2}=300 K and T_{O2}=300 K (lines) or 100 K (symbols).

Figure 11a shows the heat release rate as a function of the strain rate for the pressure range of 10-250 bar. Both the oxygen and hydrogen inlet temperatures are set to 300 K. For a given pressure, the heat release rate $\dot{q}_s$ first increases linearly with the strain rate, reaches its maximum, and decreases slightly before extinction. The linear dependence of $\dot{q}_s$ on the strain rate appears to be insensitive to pressure, although a higher pressure increases the strain rate and temperature at the extinction limit. The overall result can be correlated with the product of pressure and strain rate, *pa*. Figure 11b shows the functional relationship of $\dot{q}_s \sim \sqrt{pa}$.

Figure 12 shows the maximum temperature (T_{max}) as a function of strain rate. At low strain rates, T_{max} remains fixed. At high strain rates, T_{max} decreases exponentially to reach its quenching temperature. The extinction strain rate, a_{ext}, which corresponds to the end point of each temperature profile in Figure 12, is approximately proportional to pressure and evolves with this parameter in a quasi-linear manner. Figure 13 shows the flame thickness (δ_f) in the pressure range of 50-250 bar for three different strain rates. As at the subcritical pressures shown in Figure 5, the result is plotted as a function of the C parameter, defined as $C = \delta_f \sqrt{pa}$. The flame thickness is approximately proportional to $1/\sqrt{pa}$ for the supercritical pressures considered herein.

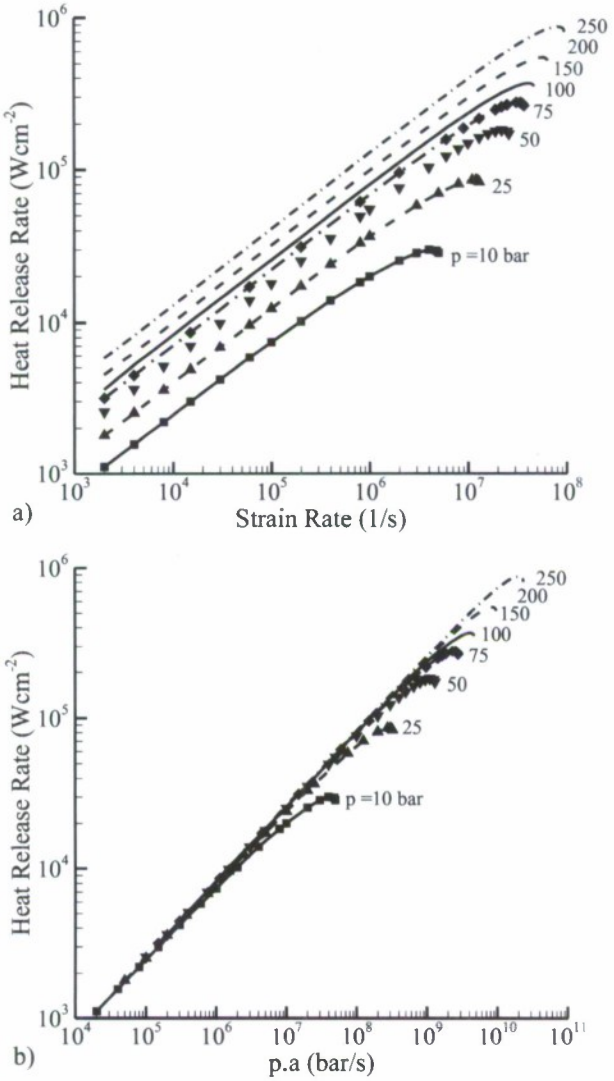

Fig. 11. Effeet of strain rate on hcat release rate for H_2/O_2 counterflow diffusion flames at different pressures. T_{H2}=300 K and T_{O2}=300 K.

2.4 Conclusion

A comprehensive analysis of laminar eounterflow diffusion flames has been developed for general fluids. Thc model incorporates fundamental thermodynamics and transport theories, and ean be applied to the entire regime of fluid thermodynamie states. In addition, eross-diffusion terms sueh as the Soret and Dufour effects are included. As a speeific examplc, diluted and undiluted H_2/O_2 flames have been studied over a broad range of pressures at both suberitical and supercritical eonditions. The effeets of pressure, strain rate, and oxygen inlet temperature on the flame behavior and energy-release rate

were examined systematically. Results not only enhance the fundamental understanding of the flame properties under various flow conditions and fluid states, but can also be used as a submodel in the treatment of non-premixed turbulent combustion.

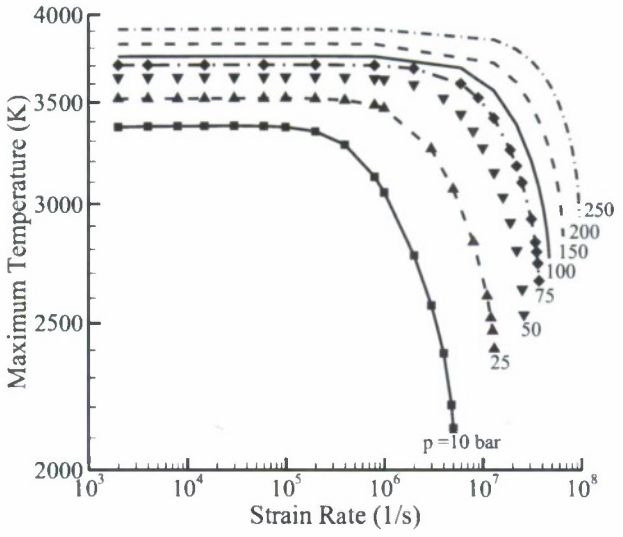

Fig. 12. Effect of strain rate on maximum temperature for counterflow diffusion flames at T_{H2} =300 K and T_{O2} = 300 K.

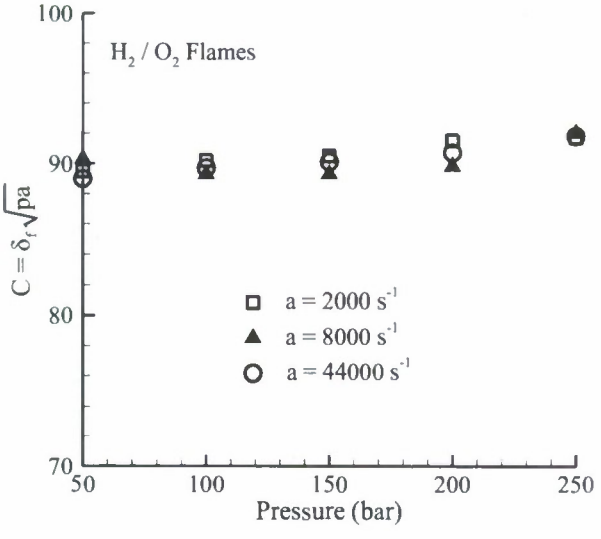

Fig. 13. Counterflow diffusion flame thickness, δf, as a function of pressure, p for three different strain rates.

The calculated flame thickness δ_f and heat-release rate per unit area $\dot{q}_s$ were found to depend on the pressure p and strain rate a through the correlations of $\delta_f \sim 1/\sqrt{pa}$ and $\dot{q}_s \sim \sqrt{pa}$, respectively. The extinction limit of the strain rate evolves with pressure in a quasi-linear manner. For H_2/O_2 and H_2/air mixtures, impacts of the

Soret and Dufour effects appear to be limited with a pressure increase, due to enhanced chemical reaction rates which override changes in diffusion. Nonetheless, the Soret effect may still exert a non-negligible influence on the extinction strain rate. Significant real-fluid effects take place and manifest themselves by rapid property variations in the transcritical regime. The resultant influence on the flame properties, however, is insignificant, since the fluid behaves as a perfect gas when entering the high-temperature flame region.

References

Balakrishnan G., Smooke M. and Williams F. (1995). A numerical investigation of extinction and ignition limits in laminar non-premixed counter-flowing hydrogen-air streams for both elementary and reduced chemistry. *Combust. Flame* **102**, 329–340.

Ben Dakhlia R., Giovangigli V. and Rosner D. (2002). Soret effects in laminar counterflow spray diffusion flames. *Combust. Theory Model.* **6**, 1–17.

Briones A. and Aggarwal S. (2005). A numerical study of H_2-air partially premixed flames. *Int. J. Hydrogen Energy* **30**, 327–339.

Brown T., Tanoff M., Osborne R., Pitz R. and Smooke M. (1997). Experimental and numerical investigation of laminar hydrogen-air counterflow diffusion flames. *Combust. Sci. and Tech.* **129**, 71–88.

Candel S., Juniper M., Singla G., Scouflaire P. and Rolon C. (2006). Structure and dynamics of cryogenic flames at supercritical pressure. *Combust. Sci. and Tech.* **178**, 161–192.

Chung T., Ajlan M., Lee L. and Starling K. (1988). Generalized multiparameter corresponding state correlation for polyatomic, polar fluid transport properties. *Indust. Chem. Engin. Research* **27**, 671–679.

Congiunti A., Bruno C. and Giacomazzi E. (2003). Supercritical combustion properties. AIAA Paper No. 2003-0478.

Dagusc T., Crooncnbroek T., Rolon J., Darabiha N. and Soufiani A. (1996). Study of radiative effects on laminar counterflow H2/O2/N2 diffusion flames. *Combust. Flame* **106**, 271–287.

Darabiha N. (1992). Transient behavior of laminar counterflow hydrogen air diffusion flames with complex chemistry. *Combust. Sci. and Tech.* **86**, 163–181.

Darabiha N., Giovangigli V., Candel S. and Smooke M. (1988). Extinction of strained premixed propane-air flames with complex chemistry. *Combust. Sci. and Tech.* **60**, 267–285.

Ern A. and Giovangigli V. (1998). Thermal diffusion effects in hydrogen-air and methane-air flames. *Combust. Theory Model.* **2**, 349–372.

Ern A. and Giovangigli V. (1999). Impact of detailed multicomponent transport on planar and counterflow hydrogen-air and methane-air flames. *Combust. Sci. and Tech.* **149**, 157–181.

Fotache C., Sung C., Sun C. and Law C. (1998). Mild oxidation regimes and multiple criticality in nonpremixed hydrogen-air counterflow. *Combust. Flame* **112**, 457–471.

Graboski M. and Daubert T. (1978). A modified Soave equation of state for phase equilibrium calculation. *Indust. Eng. Chem. Process Design and Development* **17**, 443–450.

Im H., Law C., Kim J. and Williams F. (1995). Response of counterflow diffusion flames to oscillating strain rates. *Combust. Flame* **100**, 21–30.

Juniper M., Tripathi A., Scouflaire P., Rolon J.C., and Candel S. (2000). Structure of cryogenic flames at elevated pressures. *Proc. Combust. Inst.* **28**, 1103-1109.

Juniper M., Darabiha N. and Candel S. (2003). The extinction limits of a hydrogen counterflow diffusion flame above liquid oxygen. *Combust. Flame* **135**, 87–96.

Katta V. and Roquemore W. (1998). Simulation of dynamic methane jet diffusion flames using finite rate chemistry models. *AIAA J.* **36**, 2044–2054.

Kee R., Dixon-Lewis G.,Warnatz J., Coltrin M. and Miller J. (1986). A Fortran computer code package for the evaluation of gas phase multicomponent transport properties. Technical Report SAND86-8286 UC401, Sandia National Laboratories.

Law C. (2006). Propagation, structure and limit phenomena of laminar flames at elevated pressures. *Combust. Sci. and Tech.* **178**, 335–360.

Li J., Zhao Z., Kazakov A. and Dryer F. (2004). An updated comprehensive kinetic model of hydrogen combustion. *Int. J. Chem. Kinet.* **36**, 1–10.

Mayer W., Schik A., Vielle, B., Chauveau C., Gokalp I., Talley D., and Woodward R. (1998). Atomization and breakup of cryogenic propellants under high-pressure subcritical and supercritical conditions. *J. Propul. Power* **14**, 835-842.

Meng H., Hsiao G., Yang V. and Shuen J. (2005). Transport and dynamics of liquid oxygen droplets in supercritical hydrogen streams. *J. Fluid Mechanics* **527**, 115–139.

Meng H. and Yang V. (2003). A unified treatment of general fluid thermodynamics and its application to a preconditioning scheme. *J. Comput. Phys.* **189**, 277–304.

Miller J., Mitchell R., Smooke M. and Kee R. (1982). Towards a comprehensive chemical kinetic mechanism for the oxidation of acetylene: comparison of model predictions with results from flame and shock tube experiments. *Proc. Combust. Inst.* **19**, 181–196.

Muller M., Kim T., Yetter R. and Dryer F. (1998). Flow reactor studies and kinetic modeling of the H_2/O_2 reaction. *Int. J. Chem. Kinet.* **31**, 113–125.

Niioka T., Hasegawa S., Tsukamoto T., and Sato J., Diffusion-flame extinction of liquid fuel at elevated pressures. *Combust. Flame* **86**, 171-178.

Oefelein J. and Yang V. (1998) Modeling of high-pressure mixing and combustion processes in liquid rocket engines. *J. Propul. Power* **14**, 843-857.

Oefelein J. (2006). Mixing and combustion of cryogenic oxygen-hydrogen shear coaxial jet flames at supercritical pressure. *Combust. Sci. and Tech.* **178**, 229–252.

Palle S., Nolan C. and Miller R.S., (2005). On molecular transport effects in real gas laminar diffusion flames at large pressure. *Phys. Fluids* **17**. 103601.

Poinsot T. and Veynante D. (2005). *Theoretical and Numerical Combustion* (2nd ed.). Edwards, Philadelphia, USA.

Singla G., Scouflaire P., Rolon C., and Candel S. (2005). Transcritical oxygen/transcritical or supercritical methane combustion. *Proc. Comust. Inst.* **30**, 2921-2928.

Singla G., Scouflaire P., Rolon C., and Candel S. (2006). Planar laser induced fluorescence of OH in high pressure cryogenic LOx/GH2 jet flames. *Combust. Flame.* **144**, 151-169.

Smooke M., Puri I. and Seshadri K. (1986). A comparison between numerical calculations and experimental measurements of the structure of a counterflow diffusion flame burning diluted methane in diluted air. *Proc. Combust. Inst.* **21**, 1783–1792.

Soave G. (1972). Equilibrium constants from a modified Redlich-Kwong equation of state. *Chem. Eng. Sci.* **27**, 1197.

Sohn C., Chung S., Lee S. and Kim J. (1998). Structure and acoustic-pressure response of hydrogen-oxygen diffusion flames at high pressure. *Combust. Flame* **115**, 299–312.

Sung C., Liu J. and Law C. (1995). Structural response of counterflow diffusion flames to strain rate variations. *Combust. Flame* **102**, 481–492.

Takahashi S. (1974). Preparation of a generalized chart for the diffusion coefficient of gases at high pressures. *J. Chem. Engineering* (Japan) **7**, 417.

Williams B. (2001). Sensitivity of calculated extinction strain rate to molecular transport formulation in nonpremixed counterflow flames. *Combust. Flame* **124**, 330–333.

Yang V. (2000). Modeling of supercritical vaporization, mixing and combustion processes in liquid-fueled propulsion systems. *Proc. Combust. Inst.* **28**, 925–942.

Zong N., Meng H., Hsieh S. and Yang V. (2004). A numerical study of cryogenic fluid injection and mixing under supercritical conditions. *Phys. Fluids* **16** (12), 4248–4261.

Zong N. and Yang V. (2007). Near-field flow and flame dynamics of LOX/methane shear coaxial injector under supercritical conditions. *Proc. Combust. Inst.* **31** (in press)

Task 3

Flame Stabilization and Spreading of Liquid Oxygen (LOX) and Methane at Supercritical Conditions

Summary

A comprehensive theoretical/numerical framework has been established to treat the turbulent combustion of liquid oxygen (LOX) and methane under supercritical conditions. The turbulence/chemistry interaction is modeled using the steady laminar flamelet model. Detailed LOX/methane reaction mechanism is used for the chemical reaction. Turbulence closure is achieved by a large-eddy simulation technique. The applicability of the turbulent combustion model has been carefully accessed by comparing the chemical and turbulent time scales at condition typical of liquid-propellant rocket engine operation. Results indicate that the flamelet assumption is appropriate. The supercritical mixing and combustion of LOX and methane in the vicinity of a splitter plate has been analyzed and the effect of real-fluid thermodynamics on the cryogenic flame evolution has been quantified.

3.1 Introduction

Although the use of cryogenic oxygen and hydrogen as propellants in liquid-propellant rocket engines has been well established for a variety of launch vehicle applications, the low density of liquid hydrogen gives rise to a large propellant tank volume and booster size. Compared with hydrogen, methane, as a potential propellant candidate, possesses many superior performance and property characteristics. First, liquid methane is six times denser than liquid hydrogen, and thus, requires a much smaller/lighter storage vessel. Second, methane offers the advantage of being a "soft cryogen" because its vaporization temperature is much higher than that of hydrogen. It is easier to store and imposes fewer insulation and handling concerns. Third, the cost of methane production is 5 to 10 times cheaper than that of hydrogen. Furthermore, out of common hydrocarbon fuels, methane has the highest vacuum specific impulse around 370 seconds. Consequently, engines using liquid oxygen (LOX) and methane have recently attracted considerable interest for future development of high-performance reusable launch vehicles (RLV).

A thorough understanding of propellant injection and combustion processes is essential for a useful engine design. Very limited effort, however, was made to investigate LOX/methane combustion in liquid propellant rocket engine environments. Preliminary experimental studies on the ignition of LOX/methane co-axial spray at a low pressure (1.5 atm) were carried out by Cuoco *et al.* on the M3 test bench of DLR, Germany.[1] The effects of momentum flux ratio (0.1-2.0) and Weber number (2000-15000) on the ignition process were evaluated at a chamber pressure of 1.5 bar and a fixed O/F mixture ratio of 3.4. The flame evolution was visualized by both shadowgraph and high-speed OH emission images. Two different ignition scenarios, EBI (Explosion-Blowdown-reignition) and I (ignition), were identified. The EBI process was more likely

to occur at high momentum flux ratios. Compared with LOX/hydrogen systems, LOX/methane flame appeared more easily to be lifted off from the rim of LOX post. A phenomenon could be attributed to the slow chemical kinetics of methane combustion.

Yang *et al.* [2] characterized the stationary atomization and combustion of LOX/methane and LOX/hydrogen sprays at a fixed chamber pressure of 1.5 atm on the M3 test bench. The characteristics of central LOX spray in terms of intact core lengths and droplet numbers were recorded by high resolution shadowgraph images. The intensified high-speed OH radical emission images were taken to analyze the flame anchoring and subsequent spreading. It was reported that the effect of momentum flux ratio (0.22-1.67) and Weber number (1834-15000) on the reactive shear-coaxial spray is similar to those observed under cold-flow conditions. The momentum flux ratio mainly influenced the primary break-up of the LOX jet and thus determined the length of the jet core, whereas the Weber number dictated secondary atomization and subsequent flame spreading. Significant differences exist between LOX/methane and LOX/hydrogen flames at similar injection conditions defined by Weber number and momentum flux ratio. Lifted flames with greater spreading angle were only observed for methane combustion. Yang *et al.*[3] also extended the analysis to identify the factors that dictate the oscillation of LOX jet of a LOX/methane spray. The length of the jet core oscillated at a low-frequency range of 20 to 100 Hz. The jet oscillation was prominently influenced by the variation of momentum flux ratio. An increase of momentum flux ratio gave rise to a decrease of oscillation frequency.

Experimental studies on LOX/methane combustion were also performed at elevated pressures typically encountered in operational liquid-propellant rocket engines. Zurback *et al.*[4,5] conducted a preliminary flow visualization of shear coaxial injection and combustion of LOX and methane at near-critical pressures on the Mascotte test facility at ONERA, France. Shadowgraph images revealed that the flame was attached to the LOX post and spread downstream along the oxygen jet boundary, which is quite similar to that observed for the LOX/hydrogen system. Singla *et al.*[6] performed a more detailed experiment of high-pressure oxygen and methane combustion associated with a shear coaxial injector. The temperature of the oxygen stream remained at 85 K, whereas the methane stream took a value between 120 and 288 K to simulate trans- and super-critical injection conditions. The chamber pressure varied from 4.5 to 6.0 MPa. Emission images of excited OH and CH radicals were time-averaged to determine the mean flame structure. Results indicated that the flame was stabilized in the vicinity of the LOX post tip under all flow conditions. Since vaporization was the slowest process at a subcritical temperature, part of the unburned oxygen droplets penetrated into the inner flame. After vaporization and mixing with gaseous methane at the outer boundary of the methane stream, a second flame with a greater expansion angle was formed. Therefore, the flame featured two different regions of light emission, one surrounding the liquid oxygen jet and the other located close to the outer boundary of the annular methane stream, when both LOX and methane were injected at a transcritical condition. The situation changed if oxygen was injected at a subcritical temperature while methane was gaseous. The enhancement of turbulent mixing between subcritical oxygen and gaseous methane streams led to only one flame surrounding the oxygen jet. Singla *et al.*[7] recently employed Laser-Induced Fluorescence (LIF) of OH radical to identify the flame structure of high-pressure shear coaxial LOX/methane combustion. High-quality measurements

were made in a pressure range of 1.0 to 2.5 MPa. Beyond the pressure limit of 2.5 MPa, additional fluorescence signal originating from PAH species outside the flame zone interferes with the OH fluorescence and scrambles the useful information. Over the accessible pressures, OH fluorescence images indicated that the flame develops as a thin wrinkled layer spreading near the liquid oxygen jet. The flame started from a location away from the injector lip indicating the reactive region is sensitive to the flow perturbation and the flame is less stabilized than liquid oxygen/hydrogen flames.

Non-intrusive optical measurement techniques were employed by Santoro and colleagues[8] to investigate swirl coaxial injection and combustion of LOX/GCH4 at a near critical chamber pressures (4.1 MPa) and a mixture ratio of 3.0. Detail information were obtained on spray and flame structure in the near-field. Experimental studies on high-pressure LOX/methane combustion were performed by Lux *et al.*[9] over a wide range of pressure (4.1-6.8 MPa) with the focus placed on the identification of the operating points where unstable combustion occurs. Preliminary results indicated that the propellant injection velocity ratio and combustion chamber pressure have substantial effects on the near injector flow and flame development.

In parallel to the experimental studies, numerical simulation was also carried out to investigate the high-pressure combustion of co-flowing LOX and methane through a shear-coaxial injector.[10] Several important features were identified. The injector flowfield could be characterized by the evolution of the three mixing layers originating from the trailing edges of the two concentric tubes of the injector. As a consequence of the strong inertia of the oxygen stream and the light density of methane, a diffusion-dominated flame was anchored in the wake of the LOX post and propagated downstream along the boundary of the oxygen stream. In addition, an increase in the velocity of the methane stream significantly enhanced mixing process and shortened the potential cores of both the LOX and methane jets. Although the results are encouraging, many uncertainties associated with the numerical modeling of supercritical combustion still need to be clarified. For instance, turbulence/flame interaction has never been successfully addressed in any numerical modeling of high-pressure combustion. A moment based approximate reconstruction approach was employed by Oefelein[11] to account for sub-grid scale (*sgs*) species fluctuations on the chemical reaction in a simulation of supercritical LOX/hydrogen combustion. Research to-date, however, suggested that the method is not reliable when directly applied to the filtered chemical source terms.[12]

It is well known that the flow Reynolds number increases almost linearly with pressure. An increase in pressure from 1 to 100 atm gives rise to an increase of the Reynolds number by two orders of magnitude.[13] The corresponding Kolmogorov microscale decreases by 1.5 orders of magnitude. One the other hand, a recent numerical study[14] on supercritical O_2/H_2 counterflow diffusion flames indicated that the flame thickness is inversely proportional to the square root of pressure and reduces slower than the size of Kolmogorov eddies as pressure increases. Under supercritical conditions, the Reynolds number may reach such a level that turbulent eddies could penetrate into the flame zone and promote the occurrence of unsteady phenomena (i.e., local extinction). This made the scale separation assumption inherently employed in many subgrid-scale (*sgs*) turbulent combustion models (i.e., flamelet model) becomes questionable. The

hypothesis of scale separation implies that chemistry only occur in a thin layer smaller than the size of Komogorov eddy while propellants mix in the inertial subrange of turbulence.

In this work, numerical studies are performed to investigate supercritical mixing and combustion of LOX and methane separated by a splitter plate. The theoretical and numerical frameworks for the treatment of general-fluid thermodynamics have been extended to accommodate *sgs* turbulence/flame interactions. Steady laminar flamelet model with detail chemistry has been used as the turbulent combustion model. The specific objectives of the study are: 1) to establish a reliable approach to model turbulent combustion under supercritical conditions; 2) to characterize the near-field flow dynamics and combustion processes in the vicinity of the splitter plate; and 3) to explore the effect of thermodynamic non-idealities on the high-pressure fluid mixing and dynamics in terms of turbulent length scales.

3.2 Theoretical Formulation

3.2.1 LES Transport Equations and Sub-grid Scale Models

Turbulent closure in the present work is achieved using a large-eddy-simulation technique, in which large-scale motions are calculated explicitly, whereas eddies with scales smaller than the grid or filter size are modeled to represent the effects of unresolved motions on resolved scales. The formulation treats the Favre-filtered transportation equations of mass, momentum, energy, and mixture fraction in the following conservative form,

$$\frac{\partial \bar{\rho}}{\partial t} + \frac{\partial \overline{\rho u}_j}{\partial x_j} = 0 \tag{1}$$

$$\frac{\partial \bar{\rho}\tilde{u}_i}{\partial t} + \frac{\partial(\bar{\rho}\tilde{u}_i\tilde{u}_j + \bar{p}\delta_{ij})}{\partial x_j} = \frac{\partial\left(\bar{\tau}_{ij} - \tau_{ij}^{sgs} + D_{ij}^{sgs}\right)}{\partial x_j} \tag{2}$$

$$\frac{\partial \bar{\rho}\tilde{E}}{\partial t} + \frac{\partial((\bar{\rho}\tilde{E} + \bar{p})\tilde{u}_i)}{\partial x_i} = \frac{\partial(\tilde{u}_j\bar{\tau}_{ij} + \bar{q}_i - Q_i^{sgs} - H_i^{sgs} + \sigma_{ij}^{sgs})}{\partial x_i} \tag{3}$$

$$\frac{\partial \bar{\rho}\tilde{f}}{\partial t} + \frac{\partial(\bar{\rho}\tilde{u}_i\tilde{f})}{\partial x_i} = \frac{\partial}{\partial x_i}(\bar{\rho}\tilde{D}\frac{\partial \tilde{f}}{\partial x_i} + \Phi_i^{sgs}) \tag{4}$$

where overbars and tildes denote resolved-scale and Favre-averaged resolved-scale variables, respectively. ρ, u_i, p, E, f, τ_{ij}, q_i, and D represent the density, velocity components, pressure, specific total energy, mixture fraction, viscous stress tensor, heat flux, and diffusivity, respectively. The unclosed subgrid-scale (*sgs*) terms in Eqs. (1) - (4), including the *sgs* stresses τ_{ij}^{sgs}, nonlinearity of viscous stress term D_{ij}^{sgs}, heat flux Q_i^{sgs}, energy fluxes H_i^{sgs}, viscous work $\sigma_{i,j}^{sgs}$, and scalar flux Φ^{sgs}, are defined as,

$$\tau_{ij}^{sgs} = \bar{\rho}(u_i u_j - \tilde{u}_i\tilde{u}_j) \tag{5}$$

$$D_{ij}^{sgs} = (\overline{\tau}_{ij} - \tilde{\tau}_{ij}) \tag{6}$$

$$Q_i^{sgs} = (\overline{q}_i - \tilde{q}_i) \tag{7}$$

$$H_i^{sgs} = \overline{\rho}(Eu_i - \tilde{E}\tilde{u}_i) + (\overline{pu_i} - \overline{p}\tilde{u}_i) \tag{8}$$

$$\sigma_i^{sgs} = (\overline{u_j \tau_{ij}} - \tilde{u}_j \tilde{\tau}_{ij}) \tag{9}$$

$$\Phi_i^{sgs} = \overline{\rho}(u_i f - \tilde{u}_i \tilde{f}) \tag{10}$$

A dynamie Smagorinsky model (DSM) proposed by Moin *et al.*[15] is employed to close those *sgs* terms. The anisotropic part of the sgs stresses, Eq. (5), is treated using the Smagorinsky model, while the isotropic part, τ_{kk}^{sgs}, is modeled with a formulation proposed by Yoshizawa,[16]

$$\tau_{ij}^{sgs} - \frac{\delta_{ij}}{3}\tau_{kk}^{sgs} = -2\nu_t \overline{\rho}(\tilde{S}_{ij} - \frac{\delta_{ij}}{3}\tilde{S}_{kk}) \tag{11}$$

$$\tau_{kk}^{sgs} = 2\overline{\rho}k^{sgs} = 2C_I \overline{\rho}(D\Delta)^2 \left|\tilde{S}\right|^2 \tag{12}$$

where

$$\nu_t = C_R(D\Delta)^2 \left|\tilde{S}\right| \tag{13}$$

$$\tilde{S}_{ij} = \frac{1}{2}(\frac{\partial \tilde{u}_j}{\partial x_i} + \frac{\partial \tilde{u}_i}{\partial x_j}) \tag{14}$$

$$k^{sgs} = \frac{1}{2}(u_i u_i - \tilde{u}_i \tilde{u}_i) \tag{15}$$

The dimensionless quantities C_R and C_I are the compressible Smagorinsky model constants and are determined dynamieally during ealeulation. The model utilizes the information about resolved seales at the grid-filter level and at a coarser test-filter level with $\tilde{\Delta} > \Delta$. The least-square method proposed by Lilly[17] is then implemented to obtain the two model parameters,

$$C_R = \frac{\langle L_{ij} M_{ij} \rangle}{\langle M_{kl} M_{kl} \rangle} - \frac{1}{3}\frac{\langle L_{mm} M_{nn} \rangle}{\langle M_{kl} M_{kl} \rangle} \tag{16}$$

$$C_I = \frac{\langle L_{kk} \rangle}{\langle \beta - \hat{\alpha} \rangle} \tag{17}$$

The braekets $\langle \cdot \rangle$ denotes loeal smoothing in the test filter,[18] whieh is used to eireumvent the numerical instability originating from the dynamieally ealculating the eoefficicnts of the eddy-viscosity model.[15,19] A loeal volume-weighted average with around 27 points is employed. The explieit forms of L_{ij}, M_{ij}, β, and α, are,

$$L_{ij} = \bar{\rho}\tilde{u}_i\tilde{u}_j - \hat{\bar{\rho}}\tilde{u}_i\tilde{u}_j = \overline{\rho u_i}\,\overline{\rho u_j}/\bar{\rho} - \overline{\rho u_i}\,\overline{\rho u_j}/\hat{\bar{\rho}} \tag{18}$$

$$M_{ij} = \beta_{ij} - \hat{\alpha}_{ij} \tag{19}$$

$$\alpha = 2\bar{\Delta}^2\bar{\rho}\left|\tilde{S}\right|^2 \tag{20}$$

$$\beta = 2\hat{\Delta}^2\hat{\bar{\rho}}\left|\tilde{\tilde{S}}\right|^2 \tag{21}$$

$$\beta_{ij} = -2\hat{\Delta}^2\hat{\bar{\rho}}\left|\tilde{\tilde{S}}\right|(\tilde{\tilde{S}}_{ij} - \delta_{ij}\tilde{\tilde{S}}_{kk}/3) \tag{22}$$

$$\alpha_{ij} = -2\Delta^2\bar{\rho}\left|\tilde{S}\right|(\tilde{S}_{ij} - \delta_{ij}\tilde{S}_{kk}/3) \tag{23}$$

where the hat represents the test-filtered variable. A Favre-filtered variable at the test-filter level is defined as $\tilde{\tilde{f}} = \overline{\rho f}/\hat{\bar{\rho}}$.

The subgrid energy flux term, H_i^{sgs}, is modeled as

$$H_i^{sgs} = --\bar{\rho}\frac{\nu_t}{Pr_t}\frac{\partial\tilde{H}}{\partial x_i} = -\bar{\rho}\frac{\nu_t}{Pr_t}\left(\frac{\partial\tilde{h}}{\partial x_i} + \tilde{u}_j\frac{\partial\tilde{u}_j}{\partial x_i} + \frac{1}{2}\frac{\partial k^{sgs}}{\partial x_i}\right) \tag{24}$$

where $\tilde{H}$ represents the filtered specific total enthalpy. The turbulent Prandtl number, takes a conventional value of 0.7. Because mixture fraction, f, is a conserved scalar, the subgrid scalar flux, Φ_i^{sgs}, can be easily modeled by eddy viscosity models based on gradient transport assumption as,

$$\Phi_i^{sgs} = \bar{\rho}(u_i f - \tilde{u}_i\tilde{f}) = -\bar{\rho}\frac{\nu_t}{Sc_t}\nabla\tilde{f} \tag{25}$$

A constant turbulent Schmidt number, Sc_t, of 0.4 is employed.[20]

It is noteworthy that accurate modeling of *sgs* dynamics under supercritical conditions remains a challenging task, due to complications arising from rapid property variations and real-fluid thermodynamics and transport. Very limited effort has been applied so far to quantify the effects of real-fluid thermodynamics on small-scale turbulent structures and a well-calibrated *sgs* model for supercritical fluid flows is currently not available. This issue will be addressed in our subsequent work.

3.2.2 Subgrid-scale Turbulent Combustion Model

The modeling of turbulence/chemistry interaction in a physically meaningful manner represents a critical and challenging issue in the present study of supercritical combustion. Figure 1, commonly referred to as regime diagram for non-premixed turbulent combustion, shows the variation of $\log(\sqrt{k}/\hat{u})$ with $\log(l_I/\hat{l})$, where $\hat{l}$ and $\hat{u}$ are the reference length and velocity scales for non-premixed flames, respectively, k and l_I turbulent kinetic energy and integral length, respectively.[21] Four different combustion

regimes exist. Laminar flames occur at low Reynolds numbers. Thin flames, identified as flamelets, take place when the chemical time, τ_c, is smaller than the Komogorov time scale, τ_K. Under such a condition, the flame structure can not be influenced by turbulent eddies and the scale separation assumption is valid. The other extreme, thickened flames, occurs when τ_c is greater than the integral time scale, τ_l. In this regime, turbulent flow motions greatly enhance the mixing of fuel and oxidizer. Thus, the combustion process can be locally modeled as well-stirred and is rate controlling. Flamelet structures interact with turbulence in the intermediate regime, called perturbed flamelet, when $\tau_K \le \tau_c \le \tau_l$. For a turbulent diffusion flame, the local time and length scales of flame depend strongly on such flow conditions as the strain rate, and are affected by various unsteady effects encountered. The flame structures may vary at different spatial locations in the flowfield.

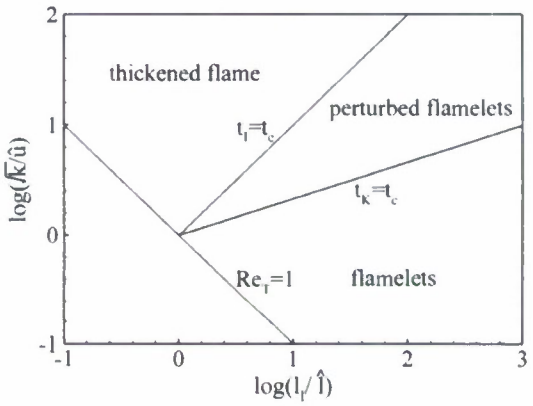

Figure 1 Regimes for turbulent non-premixed combustion (taken from Lentini[21]).

Laminar flamelet model

The basis assumption of the laminar flamelet model is that chemical scales are shorter than the Kolmogorov scale of turbulent flows.[22] Consequently, a turbulent flame can be envisioned as a synthesis of thin reaction zones (i.e., flamelets) embedded in an otherwise inert turbulent flowfield, and the inner structure of the flame can be handled separately from turbulent flow simulations. Instead of directly treating the reactive scalar (i.e., species conservation), the focus of the flamelet model is placed on the identification of the flame surface in the flowfield, which can be obtained by solving the conservation equation of the mixture fraction in a coupled manner with the mass, momentum, and energy equations.

The flame thickness, however, is typically smaller than the grid size employed in LES and is not actually resolved. Therefore, the filtered species mass fraction of the *ith* species, $\tilde{Y}_i(x,t)$, in each computational cell should be evaluated by convoluting the state relationships, $Y_i(f,\chi_{st})$, with the *sgs* filtered probability density function (*FDF*) of mixture fraction, $P(f)$, and the *sgs FDF* of scalar dissipation rate, $P(\chi_{st})$, as follows,

$$\tilde{Y}_i(x,t) = \int_0^1 \int_0^\infty Y_i(f,\chi_{st}) P(\chi_{st}) P(f) d\chi_{st} df \tag{26}$$

It should be noted that a statistieal independenee is intrinsieally assumed in Eq. (26) between the *sgs* variations of mixture fraetion and sealar dissipation. The unresolved *sgs* fluctuation of mixture fraetion is commonly represented by a presumed β-shaped probability density function (PDF) parameterized by the filtered mixture fraction and its *sgs* variance, which takes the following form,

$$P(f;\tilde{f},f''^2) = \frac{f^{\alpha-1}(1-f)^{\beta-1}}{\Gamma(\alpha)\Gamma(\beta)}\Gamma(\alpha+\beta) \tag{27}$$

where Γ is the γ-function. The parameters α and β are defined as,

$$\alpha = \tilde{f}\left(\frac{\tilde{f}(1-\tilde{f})}{f''^2} - 1\right) \tag{28}$$

$$\beta = (1-\tilde{f})\left(\frac{\tilde{f}(1-\tilde{f})}{f''^2} - 1\right) \tag{29}$$

The *sgs* varianee of mixture fraetion, f''^2, is modeled based on the scale similarity assumption as,[23]

$$f''^2 = K_b \overline{\bar{\rho}(\tilde{f} - \tilde{\bar{f}})^2} / \bar{\bar{\rho}} \tag{30}$$

where K_b is a modcl constant chosen as 3. It has been validated by many rcsearchers that the β-funetion *pdf* provides an exeellent estimation for the *sgs* mixture fraction distribution for non-premixed reaeting turbulent flows.[23,24] For simplicity, the *sgs* FDF of scalar dissipation rate, $P(\chi_{st})$, whieh is typieally assumed to be a lognormal, is eonsidered as a Dirac peak at the filtered sealar dissipation rate in the presently work. Further investigation on this issue is required in the subsequent studies. The filtered rate of sealar dissipation, $\tilde{\chi}$, is modeled based on an eddy viseosity approaeh as suggested by Girimaji and Zhou,[25]

$$\tilde{\chi} = 2\left(\frac{\nu}{Sc} + \frac{\nu_t}{Sc_t}\right)\left(\frac{\partial f}{\partial x_j}\frac{\partial f}{\partial x_j}\right) \tag{31}$$

The thermoehemistry state relation is established through a steady-state flamelet approach featuring a detailed oxygen/methane ehemistry with 16 speeies and 16 chemical reaetions.[26] This mechanism has been validated against experimental data over a pressure range of 1 to 20 atmospheres for different flame configurations. Caleulations were performed of counterflow diffusion flames of LOX and methane at five different nominal strain rates of 4000, 5000, 8000, 16000, and 20000 s^{-1}. For all the flame ealeulations, the pressure is fixed at 100 atm and the inlet temperature of oxygen and methane is 120 and 300 K, respectively. It has been noted by Ribert *et al.*[14] that eryogenie flame is extremely resistant to flow strain. A distinction stain rate of 1.76×10^6, which is at least one order greater than the maximum strain rate expeeted in the jet flame

within a typical liquid-propellant rocket engine[27] is obtained under the present flow configuration. Therefore, no flame solution at extinction state is considered for the establishment of flame library. For each strain rate, the scalar dissipation rate is a function of the mixture fraction. To be consistent with the flamelet assumption, the corresponding scalar dissipation rate, χ, of each flame solution is evaluated at the stoichiometric location. The effect of flow strain on the flamelet solution is indictated in Figure 2. The increase of strain rate enhances the heat and species transport close to the flame front, which leads to the deceases of inner layer temperature and flame thickness. The production of OH radial is also retarded. The effect of strain rate on the thickness of a counterflow diffusion flame of gaseous methane and liquid oxygen under supercritical pressure was systematically investigated in Ref. 14. At a constant ambient pressure, the flame thickness is inversely proportional to the square root of strain rate. To facilitate the establishment of the flamelet library, each flamelet solution obtained has been expressed as a function of mixture fraction, as shown in Figure 3. The solutions are then integrated based on Eq. (26) and tabulated as functions of $\tilde{\chi}$, $\tilde{f}$, and f''^2. The present table has five support points in $\tilde{\chi}$ direction and is resolved by 51×51 nodes in $f\times f''^2$ space.

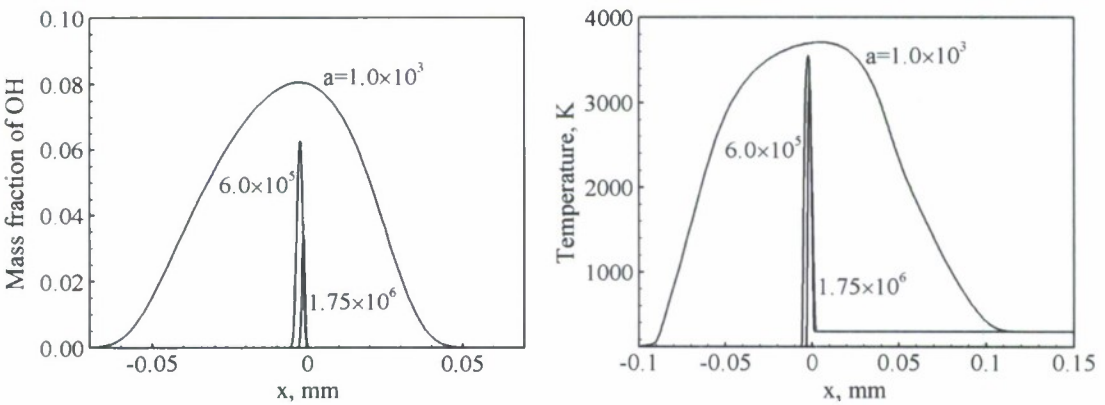

Figure 2 Effect of strain rate on flame thickness of a liquid oxygen/methane laminar diffusion flame.

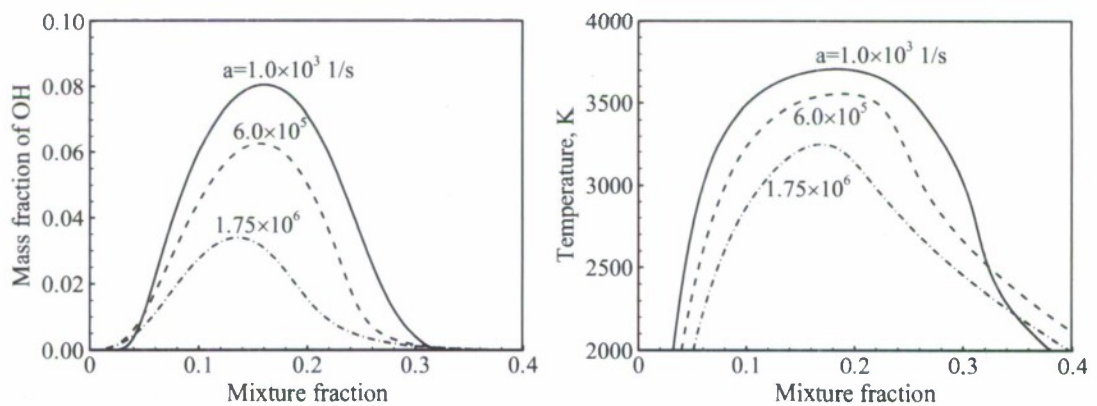

Figure 3 Effect of strain rate on the behavior of laminar diffusion flames.

The calculated filtered mixture fraction, mixture fraction variance, and scalar dissipation rate from LES simulation are employed to determine the appropriate entry of the flamelet table.

3.2.3 Real Fluid Thermodynamics and Transport

An essential prerequisite of any realistic analysis of supercritical fluid dynamics lies in the establishment of a unified property evaluation scheme capable of treating thermodynamic properties of pure substances and mixtures over the entire fluid thermodynamic states of concern from compressed liquid to dilute gas.[28] At elevated pressures, thermodynamic models normally employed to represent ideal-gas behavior may encounter many difficulties. From the microscopic point of view, the intermolecular mean free paths reduce with increase of pressure, and consequently the molecular volume and intermolecular forces are no longer negligible. For convenience, each property can be expressed as the sum of an ideal-gas property at the same temperature and a thermodynamic departure function, which takes into account the dense-fluid correction. For example, the specific internal energy of a general fluid mixture can be expressed as

$$e(T,\rho) = e_0(T) + \int_{\rho_0}^{\rho} \left[\frac{p}{\rho^2} - \frac{T}{\rho^2} \left(\frac{\partial p}{\partial T} \right)_{\rho} \right]_T d\rho \tag{32}$$

The subscript 0 refers to a reference thermodynamic state in the limit of an ideal gas.

Because the intermolecular interactions between molecules of different components in a mixture may differ significantly from those between the same types of molecules in a pure substance, the concepts of partial properties should be implemented to estimate the properties of each component under high pressures. To facilitate numerical implementation, the concepts of partial-mass and partial-density properties were introduced by Meng and Yang.[29] The partial-density internal energy is defined as,

$$\tilde{e}_i = \left(\frac{\partial \rho e}{\partial \rho_i} \right)_{T, \rho_{j \neq i}} \tag{33}$$

where ρ_i is the density of the *ith* species of a fluid mixture. The indices, i and j, range from 1 to N.

An equation of state valid for a broad range of fluid states is required to represent the fluid P-V-T behavior of a supercritical fluid mixture. A modified Soave-Redlick-Kwong (SRK) equation of state is adopted in the present work because of its wide range of validity and ease of implementation. It takes the following form,

$$p = \frac{\rho R_u T}{W - b\rho} - \frac{a\alpha}{W} \frac{\rho^2}{(W + b\rho)} \tag{34}$$

where R_u is the universal gas constant and W the molecular weight. The parameters a and b account for the effects of attractive and repulsive forces between molecules, respectively. The third parameter α includes the critical compressibility factor and acentric (size-shape) interactions between molecules.

Based on the SRK equation of state, the specific internal energy of a general fluid mixture is derived as,

$$e(T,\rho) = e_0(T) + \frac{T^2}{bW}\left(\frac{\partial a\alpha / T}{\partial T}\right)_{\rho,Y_i} \ln\left(\frac{W+b\rho}{W+b\rho_0}\right) \tag{35}$$

where Y_i is the mass fraction of the *ith* constituent species of a mixture. Substitution of Eq. (35) into Eq. (33) yields the partial-density internal energy of species *i*,

$$\begin{aligned}\hat{e}_i = e_{i,0} &+ \frac{2}{bW_i}\left[\sum_j^N x_j\left(T\frac{\partial}{\partial T}(a_{ij}\alpha_{ij}) - a_{ij}\alpha_{ij}\right)\right]\ln\left(\frac{W+b\rho}{W+b\rho_0}\right) \\ &+ \frac{b_i}{bW_i}\left[T\frac{\partial}{\partial T}(a\alpha) - a\alpha\right]\left[\frac{\rho}{M+b\rho} - \frac{1}{b}\ln\left(\frac{W+b\rho}{W+b\rho_0}\right)\right]\end{aligned} \tag{36}$$

where N is the number of species in the mixture and x_i is the mole fraction of species *i*. The partial-density enthalpy, $\tilde{h}_i$, can be easily written as,

$$\hat{h}_i = \hat{e}_i + \left(\frac{\partial p}{\partial \rho_i}\right)_{T,\rho_{j\neq i}} \tag{37}$$

The constant-volume heat capacity can be obtained as,

$$C_v = C_{v,0}(T) + \frac{T}{bW}\frac{\partial^2}{\partial T^2}(a\alpha)\ln\left(\frac{W+b\rho}{W+b\rho_0}\right) \tag{38}$$

Details of the derivation and implementation of real-fluid thermodynamic properties can be found in Ref. 29.

Accurate evaluation of transport properties is also crucial for the modeling of high-pressure flow and flame dynamics. To account for the continuous variation of fluid properties in a supercritical environment, one cannot use classical techniques which deal individually with liquids or gases. In the present study, both the mixture viscosity, μ, and thermal conductivity, λ, are determined by the method proposed by Chung *et al.*,[30] established based on the Chapman-Enskog theory with a dense-fluid correction. The calculated properties agree well with the NIST experimental data for both the gas and liquid phases.[31]

3.3 Numerical Method

The theoretical formulation outlined above requires a robust computational scheme, due to the numerical stiffness arising from rapid flow property variations and wide disparities of the characteristic time and length scales involved. To this end, a unified treatment of general fluid thermodynamics, based on the concepts of partial-mass and partial-density properties is established and incorporated into a preconditioning scheme,[29,32]. All the numerical properties, including the preconditioning matrix, Jacobian matrices, and eigenvalues, are derived directly from fundamental thermodynamics theories, rendering a self-consistent and robust algorithm. The numerical formulation can

accommodate any equation of state, and is valid for fluid flows at all speeds and at all fluid thermodynamic states. Further efficiency is achieved by employing temperature instead of enthalpy as the primary dependent variable in the preconditioned energy equation. The procedure eliminates laborious iterations in solving the equation of state for temperature, and consequently facilitates the load balance among computational blocks in a distributed computing environment. The resultant scheme is highly efficient and suitable for parallel processing.

The numerical framework employs a density-based, finite-volume methodology along with a dual-time-step integration technique. Temporal discretization is obtained using a second-order backward differencing scheme, and the inner-loop pseudo-time term is integrated with a four-step Runge-Kutta scheme. Spatial discretization is achieved with a fourth-order, central-difference scheme in generalized coordinates. A nine-point stencil is employed to evaluate the convective flux in each spatial direction to improve the spectral resolution of small-scale turbulence structures. Fourth-order scalar dissipation with the coefficient $\varepsilon_4 = 0.001$ is applied to ensure numerical stability with minimum contamination of the solution.

The overall accuracy of the present scheme within the context of LES was carefully assessed based on the decay of the kinetic energy of isotropic turbulence. Calculations were performed for an isotropic turbulent flow in a cubic box of a non-dimensional width of 2π. The experimental results of Comet-Bellot and Corrsin (CBC) were selected as the benchmark with an initial Taylor Reynolds number of 80 on a $32 \times 32 \times 32$ grid[33]. Figure 4 shows the temporal evolution of resolved turbulent kinetic energy. The results with a subgrid-scale model agree well with the experimental data, whereas a slower decay of TKE is observed when the *sgs* model turned off. This indicated that the present numerical algorithm offers a reasonable predictive capability in terms of its numerical dissipation.

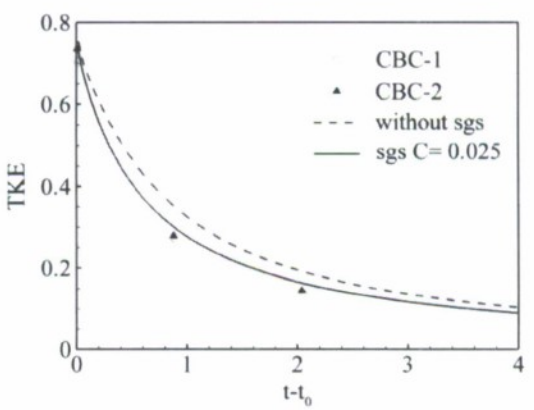

Figure 4 Decay of the resolved turbulent kinetic energy.

In the present study of LOX/methane combustion, exceedingly large property gradients exist in the near field of the injector where the fluid density varies by a factor of 1000 over a fraction of the splitter plate (0.3 mm). A second-order scalar dissipation with a total-variation-diminishing switch developed by Swanson and Turkel[34] was thus applied

to suppress numerical oscillations in regions with steep property variations. A small dissipation coefficient of 0.125 was cautiously selected to minimize the contamination on the numerical solution.

Finally, a multiblock domain decomposition technique, along with static load balance, is employed to facilitate the implementation of parallel computation with message passing interfaces (MPI) at the domain boundaries. The parallelization methodology is robust and the speedup is almost linear.

3.4 Computational Domain and Boundary Conditions

Figure 5 shows the physical model under consideration. Co-flowing methane (upper) and oxygen (lower) are injected at the inlet and separated by a 0.3 mm splitter plate. The thickness of the splitter plate is chosen to be comparable with the LOX post thickness of the shear coaxial injector typically employed in liquid-propellant rocket

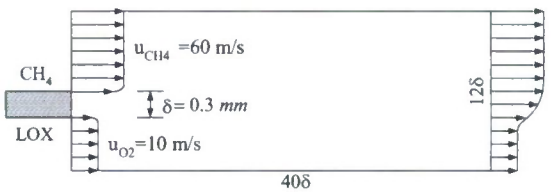

Figure 5 Schematic diagram of the computational domain employed for the analysis.

engines. The computational domain includes the inlet and a downstream region that measures 12δ and 48δ in the axial and vertical directions, respectively. The velocity profile for a fully developed turbulent pipe flow is assumed at the inlet for both streams. Turbulence is provided by superimposing broad-band white noise onto the mean velocity profile. The disturbances are generated by a Gaussian random-number generator with an intensity of 5% of the mean quantity. At the downstream boundary, extrapolation of primitive variables from the interior may cause undesired reflection of waves propagating into the computational domain. Thus, the non-reflecting boundary conditions based on the method of characteristics (MOC) are applied, along with the specification of a reference pressure. At the lower and upper boundaries, the pressure and temperature are specified as the ambient values. The velocity components are extrapolated from the interior. Finally, the no-slip adiabatic condition is enforced along the solid walls.

3.5 Results and Discussion

The laminar flamelet model is employed to study supercritical mixing and combustion of LOX and methane separated by a splitter plate. Liquid oxygen and gaseous methane are injected at temperatures of 122 and 300 K, respectively. The bulk velocities of the two streams are 10 and 60 m/s, respectively. The momentum flux ratio of the two streams is 2.7, which is typical of the shear coaxial injector for liquid-propellant rocket engines. The chamber pressure of 10 MPa is well above the critical pressure of oxygen (5.04 MPa) and methane (4.60 MPa). The critical temperatures of oxygen and methane are 154 and 191 K, respectively. Therefore, the methane stream

remains at a supereritieal state, while the LOX stream is injeeted at a transeritieal temperature. The flow Reynolds number evaluated based on the properties of methane stream and the thiekness of the splitter plate is 7.6×10^4.

The eomputational grid eonsists 360×150 points along the axial and vertical direetions, respeetively. The grids are clustered in the shear layers and near the splitter plate to resolve rapid property variations in those regions. The smallest grid size in the radial direction is 6 μm, whieh well falls in the inertial sub-range of the turbulent kinetie energy spectrum estimated using the Kolmogorov-Obukhow theory. The computational domain is divided into 44 bloeks, with eaeh ealeulated on a single proeessor of a distributed eomputing facility. The physical time step for all caleulations is 100 nano-seconds and the maximum CFL number for the inner-loop pseudo-time integration is fixed at 0.7. For all of the models eonsidered, the simulations are first eonduеted by 0.4 ms to allow the initial transients to pass through the computational domain. The instantaneous flow properties are then time averaged over an additional 1.2 ms, around 5 flow-through times, to gather the mean properties.

To explore the applieability of different turbulent combustion models under the present simulation eonditions, a eomparison between the ehemical time seale and the charaeteristie turbulent time scale is made first. The ehemical time is estimated based on the method suggested by Peters[35] as,

$$t_c = \frac{Z_{st}^2(1-Z_{st}^2)}{\chi_q} \tag{40}$$

Z_{st} is the value of mixture fraetion at the stoiehiometrie eondition and is 0.2 for oxygen/methane combustion. The extinction sealar dissipation rate, χ_q, is ealculated from a eounterflow diffusion flame at a near extinetion state, which takes the valuc 1.56×10^5 s^{-1}. The Kolmogorov time scales are given by,

$$t_I = l_I / k^{1/2} \tag{41}$$

$$t_K = (\nu/\varepsilon)^{1/2} \tag{42}$$

where the integral length seale is approximated by the thiekness of the splitter plate. Thc turbulent kinetic energy, k, viscous dissipation rate, ε, and kinetic viscosity, ν, are evaluated from the simulation results. For instance, viscous dissipation, ε, is calculated based on its definition as, $\varepsilon = \overline{\nu[\nabla u' + \nabla u'^T]:\nabla u'}$. Figurc 6 shows the ratios of ehemieal to the integral and Kolmogorov time scales at different axial locations. The turbulent time seales are estimate based on the simulation of laminar flamelet model.

The weak turbulent kinetic energy in the developing region elose to the splitter plate renders a Kolmogorov time seale that is considcrably greater than the chemical ones. Although the two turbulent seales experienee signifieant reduetions through the transition regime, the ratio of the Kolmogorov to the ehemical time remains greater than unity throughout the entire flowfield. The result eonfirms it is appropriate to use flamelet model under the prcsent simulation conditions. Cautious, however, still need to be

exerted owing the uncertainties associated with numerical model and the intrinsic approximation in models employed to evaluate the chemical and turbulence time scales.

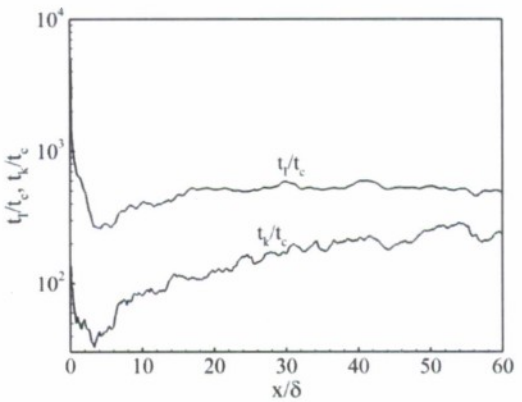

Figure 6 Axial distributions of the ratio of chemical time to the integral and Kolmogorov time scales.

Figure 7 presents the time-averaged fields of temperature and mixture fraction. Two high-temperature regions are observed in the mean temperature field. A small intensive reaction zone appears immediately behind the splitter plate and the main flame starts around 2 mm downstream. The existence of a relative low-temperature region between those two reaction zones may be attributed to the development and evolution of large-scale vortices in the near-field and the associated high flow strain. The phenomenon also indicates that the effect of scalar dissipation on the finite rate chemistry has been well accommodated in the laminar flamelet model.

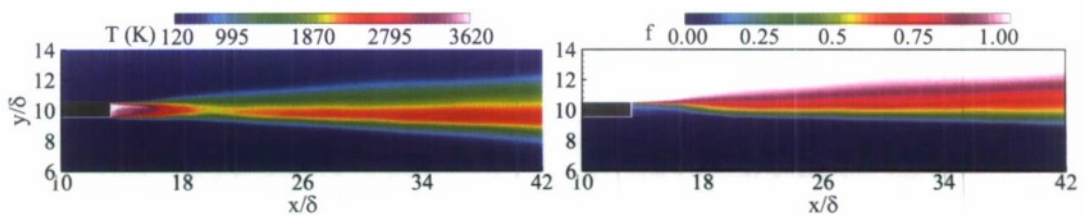

Figure 7 Time averaged temperature and mixture fraction fields

Figure 8 shows the vertical distributions of the time-averaged temperature, density, and axial velocity at different axial locations. Severe density variations occur across the LOX stream boundary, although the distinction between liquid and gas phases diminishes under supercritical pressures. In axial velocity field, negative mean velocities appear in the region immediately behind the splitter plate indicating the existence of recirculation eddies. The strong recirculating backflow in the vicinity of the splitter plate may act as a hot product tank providing the energy to ignite incoming propellants.

Figure 9 shows instantaneous field of velocity vector and mass fraction of OH and CO in the vicinity of the splitter plate. The red contour in the velocity vector fields corresponds to the isocontour line of Z_{st}=0.2, which represents the flame boundary. The large-scale vortices emerging from the upper corner of the splitter plate facilitate the

mixing between incoming methane stream and the hot products. Driven by those strong vortices, a relative weak recirculation flow region forms close to the lower corner of the splitter plate and carries the oxygen rich product toward the methane stream. Unlike

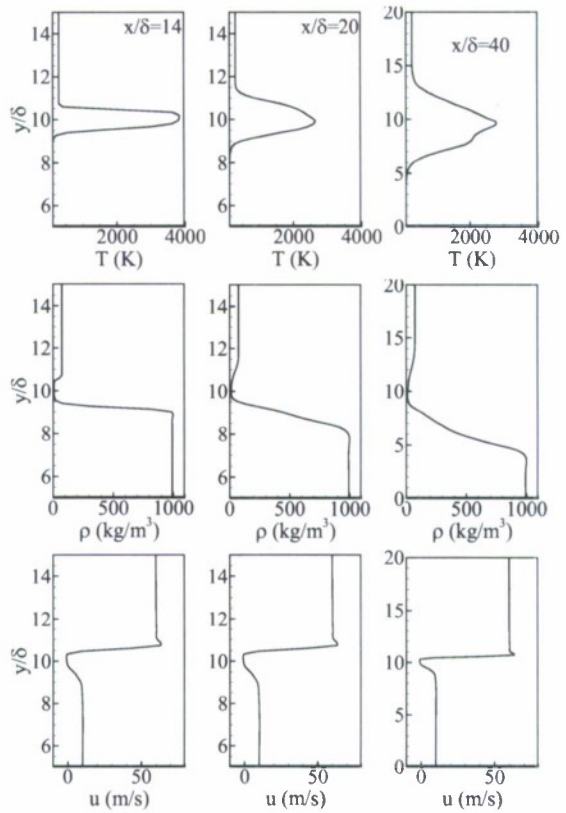

Figure 8 Distributions of mean temperature, density, and axial velocity in vertical direction at various axial locations

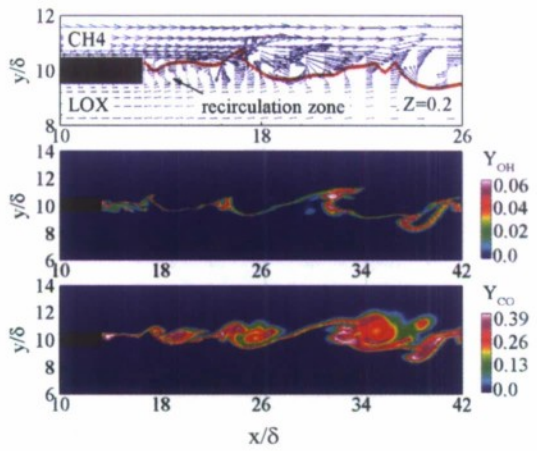

Figure 9 Snapshots of velocity vector, and mass fractions of CO and OH predicted by laminar flamelet model.

LOX/hydrogen combustion, in which the flame is anchored very close to the LOX stream because hydrogen is highly diffusive, the ignition occurs when oxygen and methane rich hot products meet at some locations between two propellant streams. Consequently, the intensive reaction zone starts from a location very close to the upper corner of the splitter plate, as indicated in the OH radical or CO mass fraction field. Since the flame is anchored at a location very close to the high-speed methane stream, the flame may be sensitive to flow perturbations and could easily be lifted off from the splitter plate. The stability of liquid oxygen methane flames is weaker than liquid oxygen/hydrogen flames.

Figure 10 shows the instantaneous fields of temperature, density, mixture fraction, vorticity, and mass fractions of O_2, CH_4, CO_2, and H_2O in the near field. A diffusion-dominated flame emanates immediately from the splitter plate and propagates downstream along the surface of the LOX stream. Large scale vortices emerge from the upper corner of the splitter plate and greatly enhance the mixing of methane and hot products. Intense property variations occur as the fluid state transfer from cryogen oxygen to hot product. For example, the fluid density varies from 10 to 1000 kg/m^3 over a very small interval close to the splitter thickness (0.3 mm). Besides transition of fluid states, the density stratification is further enhanced by anomalies variations of specific heat and thermo conductivity across the LOX stream boundary under such a supercritical condition.[10] Consequently, the exceedingly large density gradients in the region surrounding the LOX stream approach the behavior of a contact discontinuity.[11] Those regions, which behave similarly to a rigid flat plate within the flowfield in horizontal direction, increase the turbulence anisotropy at large scales.[36] The integral vortices emerging from the upper corner of the splitter plate evolve in a manner analogous to that produced by a backward-facing step and mainly reside on the lighter methane stream. The denser oxygen stream is less influenced. The growth of mixing layer between the two propellant streams is retarded. Owing to the substantial damping effects on the turbulent flow in the vertical direction, the development of flame was also restricted.

To further investigate the effect of density stratification on the cryogenic flame dynamics, the spatial correlations of mixture fraction have been calculated at different stoichiometric mixture locations. The spatial correlation coefficient of mixture fraction at spatial location x_i takes the form,

$$R(x_i) = \frac{\overline{f'(x_i - \Delta x) \times f'(x_i + \Delta x)}}{\overline{f'(x_i)^2}} \tag{43}$$

where the over bar denotes a time-averaging procedure and Δx the spatial increment in either axial or vertical direction. In the present study, six pairs of axial and vertical mixture fraction signals with separation distances from 0.3δ to 1.8δ in a 0.3δ increment were obtained at each spatial location of interest. Figure 11 presents the spatial correlation coefficients of mixture fraction in both the axial and vertical directions for $x/\delta = 12,\ 32,\ 50$. The spatial correlation distributions in both directions become wider as the sampling location moves downstream. This implies that the integral length scale grows up with the development of large scale vortices. Compared with the correlation in the axial direction, the correlation in the vertical direction exhibits much narrower distributions at all three locations. The large density gradient region leads to strong

anisotropy of the turbulence within the flowfield. It behaves like a solid wall that amplifies the horizontal turbulent fluctuation but damps the vertical ones. Since eddies of integral length scales are squashed in the vertical direction, the length scale in vertical direction is much shorter than horizontal one.

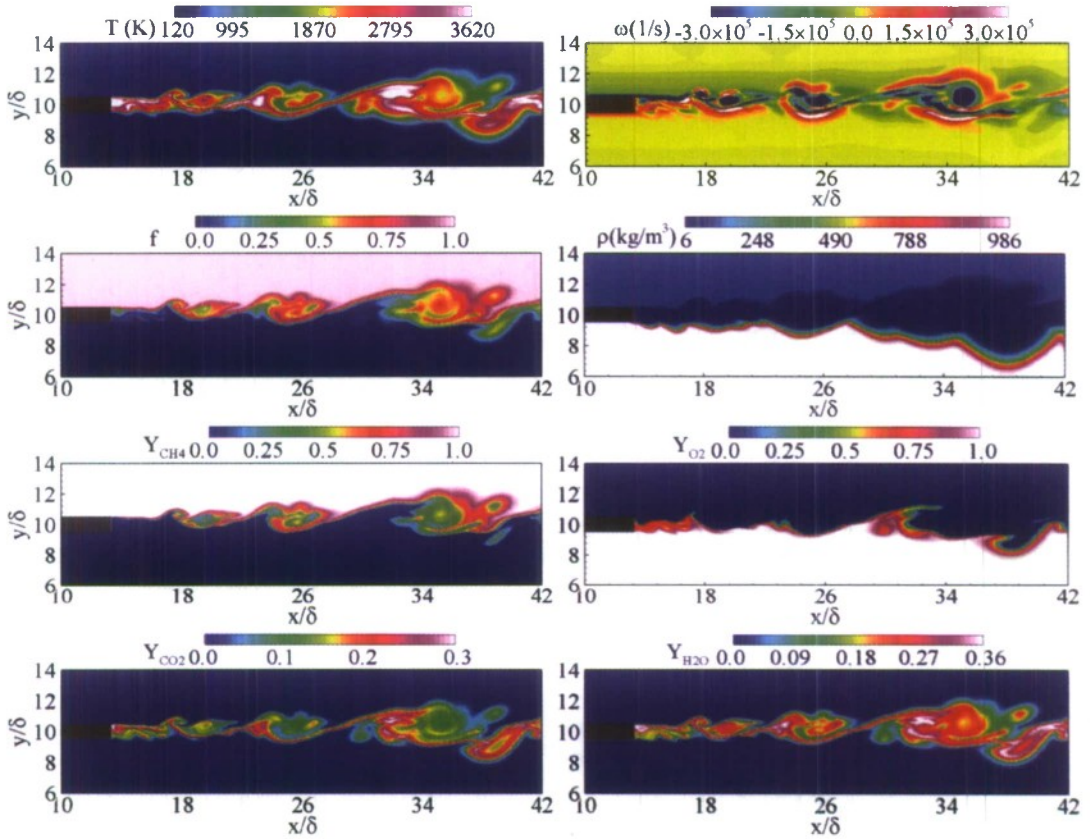

Figure 10 Snapshots of distributions of temperature, density, mixture fraction, vorticity, and mass fractions of O_2, CH_4, CO_2, CO, H_2O, and OH radical.

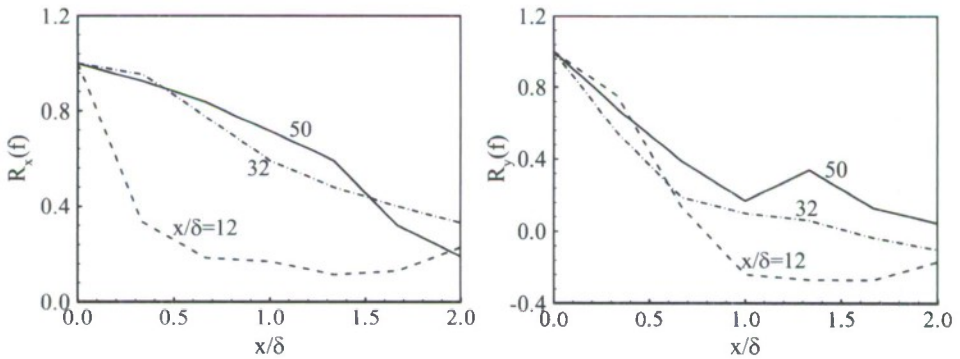

Figure 11 Spatial correlation of mixture fraction in both axial and vertical directions at three different axial locations along the mean stoichiometric mixture fraction contour.

Figure 12 shows the power spectral densities of pressure fluctuations at six different locations. A dominant frequency of 11.2 kHz, corresponding to the vortex shedding frequency downstream of the splitter platter, is obtained. Owing to vortex interactions, higher harmonics exist at upstream locations (i.e., probes 1-4). The influence of high frequency oscillations, however, diminishes rapidly as vortices propagate downstream (i.e., probes 5 and 6). It is noteworthy that the amplitude of the dominant pressure oscillation at the probes surrounding the methane stream is higher than those obtain around LOX jet boundary. This further collaborates that the formation of large density gradient region close to the LOX stream inhibits the evolution of large scale vortices.

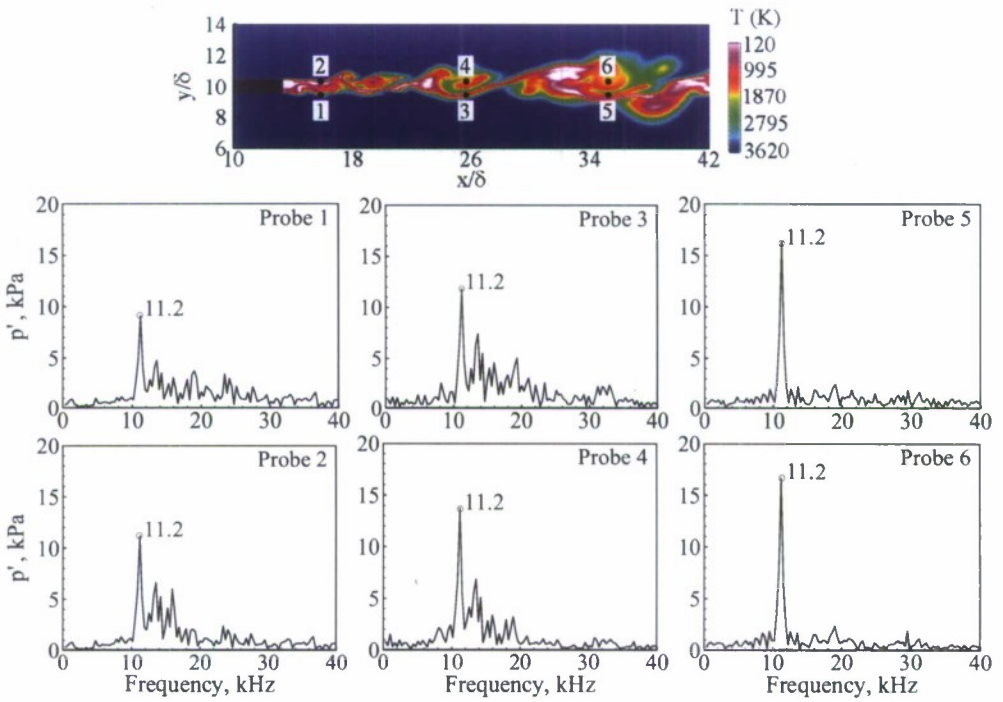

Figure 12 Frequency spectra of pressure oscillations at six different probe locations.

Summary

The unified theoretical/numerical frameworks for the treatment of general fluid thermodynamics have been extended to accommodate turbulence/flame interactions. A laminar flamelet model has been implemented, which could accommodate the detail LOX/methane combustion mechanism and the effect of flow strain on the finite-rate chemistry. The applicability of the turbulent combustion model has been accessed through a careful comparison of chemical to characteristic turbulent time scales under a condition typical of liquid-propellant rocket engine operation. The results indicate that the flamelet assumption is appropriate and supercritical combustion process is mixing dominant. The supercritical mixing and combustion of LOX and methane in the vicinity of the splitter plate has been carefully analyzed. The study confirms that the flame is stabilized by the wake recirculation zone immediately downstream of the splitter plate. The effect of real-fluid thermodynamics on the cryogen flame evolution has been

quantified. The strong density stratification between the LOX stream and hot product exerts a substantial influence on the large-scale flow motions. It amplifies the axial turbulent fluctuation but damps the radial one, and thus, leads to the strong anisotropy of turbulence near the density interface.

References

1 F. Cuoco, B. Yang, C. Bruno, O. J. Haidn, and M. Oschwald, Experimental Investigation on LOX/CH4 Ignition, AIAA Paper No. 2004-4005, 2004.

2 B. Yang, F. Cuoco, and M. Oschwald, Atomization and Flames in LOX/H2 and LOX/CH4 Spray Combusiton, J. Propul. Power 23 (2007) 763-771.

3 B. Yang, F. Cuoco, L. Wang, and M. Oschwald, Experimental Investigation of Reactive Liquid Oxygen/CH4 Coaxial Sprays, AIAA Paper No. 2007-5693, 2007.

4 S. Zurbach, J. L. Thomas, C. Verplancke, L.Vingert, and M. Habiballah, Recent Advances on LOX/Methane Combustion for Liquid Rocket Engine Injector, AIAA Paper No. 2002-4321, 2002.

5 S. Zurbach, J. L. Thomas, C. Verplancke, L. Vingert, and M. Habiballah, LOX/Methane Studies for Fuel Rich Preburner, AIAA Paper No. 2003-5063, 2003.

6 G. Singla, P. Scouflaire, C. Rolon, and S. Candel, Transcritical Oxygen/Transcritical or Supercritical Methane Combustion, Proc. Combust. Inst. 30 (2005) 2921-2928.

7 G. Singla, P. Scouflaire, C. Rolon, and S. Candel, OH Planar Laser-Induced Fluorescence and Emission Imaging in High-Pressure LOX/Methane Flames, J. Propul. Power 23 (2007) 593-602.

8 D. Salgues, A. Mouis, S. Lee, D. Kalitan, S. Pal, and R. Santoro, Shear and Swirl Coaxial Injector Studies of LOX/GCH4 Rocket Combustion Using Non-Intrusive Laser Diagnostics, AIAA Paper No. 2006-757, 2006.

9 J. Lux, D. Suslov, M. Bechle, M. Oschwald, and O. Haidn, Investigation of Sub- and Supercritical LOX/Methane Injection Using Optical Diagnostics, AIAA Paper No. 2006-5077, 2006.

10 N. Zong, and V. Yang, Near-field Flow and Flame Dynamics of LOX/Methane Shear Coaxial Injector under Supercritical Conditions, Proc. Combust. Inst. 31 (2007) 2309-2317.

11 J.C. Oefelein, Thermophysical Characteristics of LOX-H2 Flames at Supercritical Pressure, Proc. Combust. Inst. 30 (2005) 2929-2937.

12 J.C. Oefelein, Large Eddy Simulation of Turbulent Combustion Processes in Propulsion and Power Systems, Prog. Aero. Sci. 42 (2006) 2-37.

13 N. Zong, H. Meng, S.Y. Hsich, and V. Yang, A Numerical Study of Cryogenic Fluid Injection and Mixing under Supercritical Conditions, Phys. Fluids 16 (2004) 4248-4261.

[14] G. Ribert, N. Zong, V. Yang, L. Pons, N. Darabiha, and S. Candel, Counterflow Diffusion Flames of General Fluids Oxygen/Hydrogen Mixtures, Combust. Flame 154 (2007) 319-330.

[15] P. Moin, K. Squires, W. Cabot, and S. Lee, A Dynamic Subgrid-scale Model for Compressible Turbulence and Scalar Transport, Phys. Fluids A 3 (1991) 2746-2757.

[16] A. Yoshizawa, Statistical Theory for Compressible Turbulent Shear Flows, with the Applications to Subgrid Modeling, Phys. Fluids 29 (1986) 2152-2164.

[17] D.K. Lilly, A Proposed Modification of the Germano Subgrid-scale Closure Method, Phys. Fluids A 4 (1992) 633-635.

[18] Fureby, C., "On subgrid Scale Modeling in Large Eddy Simulation of Compressible Fluid Flow," *Phys. Fluids*, Vol. 8, No. 5, 1996, pp. 1301-1311.

[19] M. Germano, U. Piomelli, P. Moin, and W.H. Cabot, A Dynamic Subgrid-scale Eddy Viscosity Model, Phys. Fluids A 3 (1991) 1760-1765.

[20] H. Pitsch, and H. Steiner, Large-Eddy Simulation of a Turbulent Piloted Methane/Air Diffusion Flame (Sandia Flame D), Phys. Fluids 10 (2000) 2541-2554.

[21] D. Lentini, Assessment of the Stretched Laminar Flamelet Approach for Nonpremixed Turbulent Combustion, Combust. Sci. Tech. 100 (1994) 95-122.

[22] N. Peters, *Turbulent Combustion*, Cambridge University Press, Cambridge, UK, 2000.

[23] P.E. DesJardin, and S.H. Frankel, Large Eddy Simulation of a Non-premixed Reacting Jet: Assessment of Subgrid-scale Combustion Models, Phys. Fluids 10 (1998) 2298-2314.

[24] A.W. Cook, and J.J. Riley, Subgrid-scale Modeling for Turbulent Reacting Flows, Combust. Flame 112 (1998) 593-606.

[25] S.S. Girimaji, and Y. Zhou, Analysis and Modeling of Subgrid Scalar Mixing Using Numerical Data, Phys. Fluids A 8 (1996) 1224-1236.

[26] C.J. Sung, C.K. Law, and J.Y. Chen, An Augmented Reduced Mechanism for Methane Oxidation with Comprehensive Global Parametric Validation, Proc. Combust. Inst. 27 (1998) 295-304.

[27] M. Juniper, N. Darabiha, and S. Candel, "The Extinction Limits of a Hydrogen Counterflow Diffusion Flame above Liquid Oxygen," *Combust. Flame*, Vol. 135, No. 1, pp. 87–96.

[28] V. Yang, Modeling of Supercritical Vaporization, Mixing, and Combustion Processes in Liquid-Fueled Propulsion Systems, Proc. Combust.Inst. 28 (2000) 925-942.

[29] H. Meng, and V. Yang, A Unified Treatment of General Fluid Thermodynamics and Its Application to a Preconditioning Scheme, J. Comput. Phys. 189 (2003) 277-304.

[30] T. Chung, M. Ajlan, L. Lee, and K., Starling Generalized Multi-parameter Corresponding State Correlation for Polyatomic, Polar Fluid Transport Properties, Indust. Chem. Engin. Research 27 (1988) 671–679.

[31] A. Congiunti, C. Bruno, and E. Giacomazzi, Supercritical Combustion Properties, AIAA Paper No. 2003-0478, 2003.

[32] N. Zong, and V. Yang, An Efficient Preconditioning Scheme for General Fluid Mixture, Int. J. Comput. Fluid Dyn. 21 (2007) 217-230.

[33] G. Comte-Bellot, and S. Corrsin, Simple Eulerian Time Correlation of Full- and Narrow-Band Velocity Signals in Grid-Generated, Isotropic Turbulence, J. Fluid Mech. 48 (1971) 273-337.

[34] R. C. Swanson, and E. Turkel, On Central Difference and Upwind Schemes, J. Comput. Phys. 101 (1992) 292-306.

[35] N. Peters, Length Scales in Laminar and Turbulent Flames, In Oran, E.S., and Boris, J.P. (Eds.), *Numerical Approaches to Combustion Modeling*, AIAA, Washington D.C., , 1991, Chap. 6, 155-182.

[36] J. Bellan, Theory, Modeling and Analysis of Turbulent Supercritical Mixing, Combust. Sci. and Tech., 178 (2005)